# POLITECNICO DI TORINO

Master's Degree in Mechanical Engineering


Master’s degree thesis

## Methods for optimising the Electron Beam Melting process simulation towards multilayer analysis

***Advisor:***

*Prof. Luca Iuliano*

***Co-advisor:***

*Eng. Manuela Galati*

***Candidate:***

*Oscar Di Mauro*

# Ringraziamenti

Ringrazio con tutto il cuore i miei genitori e mia sorella, senza i quali non avrei potuto portare a termine il mio percorso accademico. Grazie per avermi sostenuto sempre nonostante tutte le difficoltà che abbiamo passato e per esservi sempre presi cura di me indipendentemente dalle scelte che ho fatto.

Ringrazio te per la persona stupenda che sei, per tutto quello che hai fatto per me da quando ti ho conosciuta e per aver creduto in me fino alla fine nella realizzazione di questo lavoro.

Ringrazio il professore Luca Iuliano e l'ingegnere Manuela Galati per avermi seguito fino all'ultimo giorno nella stesura di questo elaborato con serietà e professionalità. Grazie per avermi fatto appassionare al mio lavoro.

Ringrazio i miei amici e colleghi Tullio, Antonio e Simone. Da un progetto è sbocciata una vera amicizia. Grazie per avermi insegnato tanto in questi anni e per avermi aiutato quando ne avevo bisogno.

Ringrazio l'esperienza nel mondo militare per aver accresciuto volontà e determinazione. Sono stati essenziali per portare a termine questo lavoro.

# Abstract

*The electron beam melting (EBM) is one of the most promising metal powder-bed based additive manufacturing technologies. In recent years, a greater awareness of the advantages and limitations of this technology has been acquired, which have allowed its diffusion in the manufacturing world. In this context, process simulation plays a fundamental role in the process parameters optimisation for material development*

*The thesis work begins with an overview on the EBM process simulation. The overview highlights the main advantages and limitations according to the current computational resources. Some guidelines for the implementation of simulation models are outlined and the main degrees of freedom according to the EBM process are presented. The most used models have been grouped in according to the scale of the modelling that mainly concerns the powder modelling. Additionally, an overview of the current state of the art of the process development of 48Ti–48Al–2Cr–2Nb alloys is provided. Most of the models simulated the powder bed as a continuum, and usually the local scale finite elements (FE) models are implemented.*

*In this works a new computational analysis approach for the EBM process based on FE method is presented on the basis of a recent tool widely used in simulation. The new approach attempts to reduce the calculation time by the use of progressive activation of the elements. Criteria for the activation elements are proposed according to the physics of the EBM process. All activation criteria have been verified by analysing the activation front, the activation zone size and the*

*calculation time. Thanks to the time reduction, a multilayer simulation has been implemented.*

*The model is initially validated by simulating the melting of a single layer of 48Ti–48Al–2Cr–2Nb alloy and comparing the model outputs with the output provided by a more detail model already validated in literature. Differences in terms of melt pool size, temperature field, calculation time has been analysed. The multilayer simulation has been then validated against experimental result.*

# Table of contents

# List of figures

# List of tables

# 1 Introduction

## 1.1 Aim of the thesis

This thesis work aims to present some methodologies for optimizing the Electron Beam melting process simulation in the runtime reduction perspective through the element progressive activation (EPA). This powerful tool, widely used in the literature for the simulation of other additive manufacturing processes, not yet applied to the Electron beam melting process simulation, has found space in this thesis work. Based on some criteria for activating the elements proposed, a single-layer uncoupled simulation model was developed for the prediction of the melt pool parameters. From the comparison with a more accurate reference model based on the change of the thermophysical properties of the material, the accuracy of the model was highlighted. The work was therefore developed on a larger scale, extending the implementation of the single-layer model to the multi-layer case. Improved through the use of a material state variable, the model lends itself to the prediction of the surface roughness of the components produced by Electron Beam Melting and also lays the foundations for simulating the residual process porosity.

## 1.2 State of the art

In the section dedicated to the review of the literature, after a brief introduction to numerical simulation, a classification of the main EBM simulation models has been proposed. This classification is based on the modeling scale which mainly concerns the powder modeling. Most of the models simulated the powder bed as a continuum, and usually the local scale finite elements (FE) models are implemented. Although the model developed lends itself only to the prediction of the thermal parameters of the process, the use of the element progressive activation gives added value to the powder modelling approach so far not only from the point of view of the runtime reduction but also to a better comprehension of the process. Finally, the development of a multilayer analysis combined with the thermal activation of the elements for the prediction of lateral roughness confers greater relevance to the topic addressed. In fact, the model lends itself to predicting relevant information in a reasonable time and therefore plays an important role in optimizing process parameters.

## 1.3 The work

Literature review reports also an overview of the current state of the art of the development process of 48Ti-48Al-2Cr-2Nb alloy, highlighting the applicative potential in additive manufacturing world.

A small overview was also made of the application of element activation in literature, highlighting the main limitations of the current use of this tool. This feature as will be discussed later, implemented by means of a specific subroutine, will allow to considerably reduce the runtime. It is possible to progressively activate the elements according to different parameters such as time, spatial coordinates or a minimum temperature using different front geometries. Based on this, three activation criteria have been proposed. This allowed the development of the single-layer implementation of the model, in particular some modalities of motion control are presented in accordance with the scanning strategies most used in the EBM process

A first simulation validation was performed on a more accurate reference model based on the change of the thermophysical properties of the material. A multilayer model was implemented and through the use of a subroutine a material state variable has been implemented that allows to determine an output history of the elements activated at the solidus temperature. Finally, an experimental validation was carried out based on the lateral surface roughness of a test specimen.

# 2 Literature review

## 2.1 Electron beam melting

### 2.1.1 Overview

The electron beam melting (EBM) is one of the most promising metal powder-bed based additive manufacturing technologies, which allows to build up a component layer by layer melting conductive metal powders under vacuum by means of a high energy electron beam. The process is also known in the literature as “selective electron beam melting” (SEBM) and “electron beam additive manufacturing” (EBAM) [1]. In recent years this technology, together with the laser powder-bed fusion (L-PBF) one, has revolutionized the world of metal manufacturing, in fact, as an additive manufacturing process, the EBM makes it possible to produce in a few hours and without using tools, unlike traditional technologies, and at low operating costs, complex geometry near-net-shape components directly from CAD model. In this sense it is appropriate to point out that the manufacturing cost increases considerably as the complexity of the component increases, but this trend is significantly reduced for additive manufacturing technologies because the layer-by-layer build method combined to the complete control on xy plane simplifies considerably the tridimensional realization of a part compared to a traditional

manufacturing technology such as milling, which instead requires movement of the working tool on several axes.

The high energy and the management of the beam entrusted to electromagnetic coils allows a higher melting capability respect the L-PBF systems then an higher productivity [1], this allows to use higher thickness of powder layer (depending on the powder size and the material, it is possible to implement layer thicknesses in the range 50-150 μm [2]) although this leads to worst surface roughness (then is required a thicker machining allowance) which can be mitigated by a correct management of process parameters.

As regard as powder particles are concerned, the EBM granulometry range is higher than L-PBF ones and research carried out in literature [1] point out that decreasing the particle size there are not significant effects on material property.

Being EBM a so called “heat process”, the thermal environment allows a good shape stability then a smaller number of supports are required. Moreover, the preheating of the powder layer leads to lower thermal gradient between molten area and surrounding powder, this has effects both in terms of microstructure obtained and in a lower residual stress. In fact, a lower thermal gradient leads to a higher size of grain which can be considered intermediate between two limit dimensions corresponding to L-PBF process and casting, Fig. 1**Errore. L'origine riferimento non è stata trovata.** [3].

This allows a lower customization capability of the material by heat treatments, also because as the time and the treatment temperature increase the mechanical properties decrease as the crystalline grains increase, however the as-built microstructure obtained depicts a good compromise between mechanical properties as shown in Fig. 1.

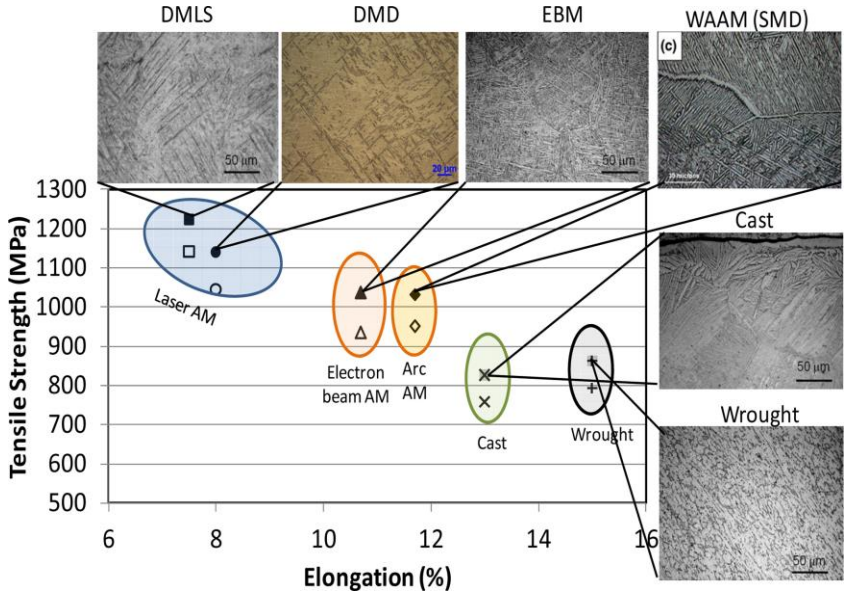


***Fig. 1*** *Mechanical properties for different production technologies*

**History of the process**

The electron beam melting technology is very recent. Researches carried out in literature [4] presumably date the origins of a process according to which a method of making tridimensional bodies layer-by-layer starting from conductor or semiconductor metal powders is presented, to a 1992 patent. The energy necessary to modify the physical characteristics of the powder, was provided by a voltage source (by electrical arc or heat) which constitutes one of the circuit poles, while the metal powder represents the other pole.

Ten years later the first electron beam melting system, the EBM S12, was developed by Arcam [5], a Swedish company which is still the leading company on the worldwide market offering a narrow range of machines with complete solutions for the realization of components by this technology. Today this company has installations throughout the world and its technology is patent protected [5].

In addition to Arcam company, nowadays some universities and research centers all over the world are developing EBM systems for industrial or scientific applications [4].

**A new concept of design for manufacturing**

The additive manufacturing technologies have made it possible to redesign the metal components offering numerous advantages, in fact the emergence of additive manufacturing provides an opportunity to redefine the "design for manufacturing" (DFM) concept of minimizing work difficulties and reducing production costs, to "design for additive manufacturing" (DFAM) one whose objective can be summarized in the following sentence "*maximize product performance through the synthesis of shapes, sizes, hierarchical structures, and material compositions"* [6]. This logic enables several advantages both in terms of product and process which are essentially those of the additive manufacturing. As far as product advantages are concerned this concept leads to a greater design freedom since the components can be optimized for mass reduction, stiffness maximization, dynamical and thermal behaviour, moreover the integration of several parts into a single element is made possible reducing the maintenance costs, and the integration of different functions. Instead among the main advantages of the process, there is the reduction of the buy-to-fly ratio [7], which is the weight ratio between the raw material used for a component and the weight of the component itself, whose reduction lead to a considerable reduction of waste and machining costs.

Other advantages are the reduction of energy consumption therefore lower emissions, and finally shorter lead time.

The weight reduction of the components constitutes the main design requirement in the application fields of EMB technology such as aerospace and automotive since high specific powers are required. In this sense, topological optimization, made it possible from the improvement of computers computing powers, has played an essential role to achieving this target. This numerical technique arises concurrently with finite-element method and represents a powerful tool for designers because it allows to find the optimal geometry of a part in terms of topology to perform a required structural target. Although in literature different categories of optimization problems are distinguished, such as size and shape optimization, topological optimization deserves more attention as it represents one of the phases of DFAM cycle. Fig. 2 shows an example of redesign for AM using topological optimization.

***Fig. 2*** *Topological optimization of a gullwing door bracket: original bracket (on left), redesigned bracket (on right).*

**High performance materials**

The EBM technique allowed the processing of metal materials that are difficult to manage such as titanium alloy which, as it known, is highly reactive with oxygen therefore the possibility of having a vacuum environment, offered by the EBM system, has improved the control of the process compared to traditional manufacturing processes such as casting or forging. Among all the titanium alloy the titanium aluminide deserve more attention, which are attractive materials for structural aerospace applications at high temperature [8], particularly the last stages of aeronautical propulsion turbines where the thermomechanical conditions are not so severe as to necessarily require a Ni-based superalloy which have a high density. In fact, the high specific strength, comparable to common steels one, the excellent corrosion and creep resistance up to T around 750 °C, the high stiffness and the ability to preserve these properties up to the temperatures mentioned above, make these alloys the best choice in the search for a compromise between weight reduction and high performance [8]. Today the development of new generation titanium aluminide alloys has widened the field of application of these materials including also the automotive sector, such as turbocharger wheel prototypes [9] where can be reached low densities and low moments of inertia.

### 2.1.2 Architecture of EBM system

The architecture of a latest generation EBM system will now be presented, highlighting the main components and their functions. It consists of several units, in general it is possible to distinguish a production unit, a control unit, and a powder management unit.

**Production unit**

Fig. 3 shows a typical EBM production unit with the powder bed already prepared and the electron beam in operation. An Arcam system [10], was taken as a reference for the creation of the architecture CAD model related to available models. An external case contains all the other components, which are made of a steel that guarantees the functioning requirements in the temperature and pressure conditions reached in chamber, which, as will be discussed in the following paragraphs, are more severe than the other additive technologies. The main components are listed below:

- an electron beam column
- two powder hoppers
- a turbomolecular pump (not shown)
- a rake to level the powder
- an elevator moved in the z direction

The electron beam column contains a cathode (which consists of a tungsten filament and a grid cup), a drift tube-anode, focus lens, astigmatism lens and deflection lens [11]. The electrons generation occurs by the electric heat of tungsten filament (at a temperature higher than 2500 K) and their acceleration happens by means of an anodic potential. The grid cup controls the electrons amount that finally reach the anode. The cross section of the beam is controlled by the focus coils and the astigmatism lens. The position of the beam on build surface is controlled by a deflection lens [11]. Focus and deflection lens are magnetic lens i.e. their link with proper coils allows the beam control.

The a turbomolecular pump is necessary to realize vacuum both near the electron gun and in the chamber, to avoid beam deflections and pickup of contaminating

elements. The inflow of helium up to $2 \cdot 10^{-3}$ mbar supports the stable process management [2].

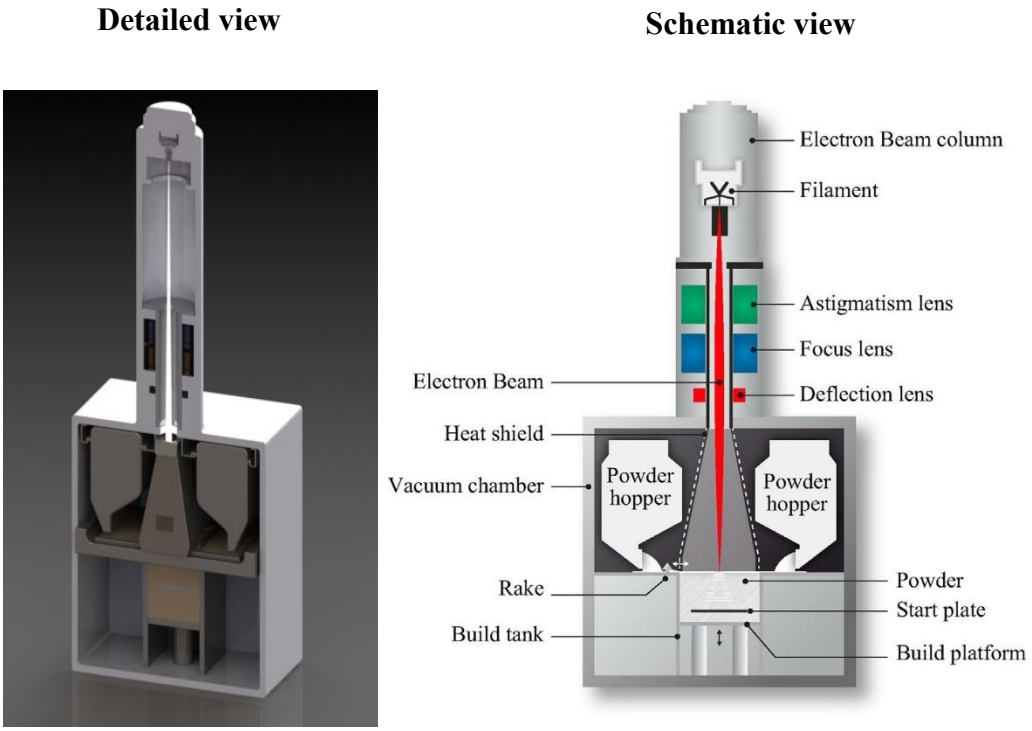


***Fig. 3*** *Production unit of an EBM system. Detailed view (on left), schematic view (on right).*

**Control unit**

The EBM system is equipped with a control unit used to manage the production unit. This unit consists of a computer on which a dedicated software is installed that allows the interface between the machine and the operator. This software is useful both in the preparation of the machine and in the processing and post-processing of the build. The machine preparation phase includes numerous steps whose failure can compromise the final result. Therefore, it is necessary to make sure of the correctness of each procedure performed and possibly repeat it. In this sense, the dedicated software greatly simplifies preparation management.

At present, in general in AM systems, it is not possible to implement a closed control, that is to carry out a monitoring of the process and simultaneously carry out a correction of the detected error, as it requires high computing power to

process the huge amount of data detected. This development would allow a reduction in the control times and therefore of the costs related to the testing of the components. However, it is still possible to monitor the process. Currently Arcam offers two solutions [12]: a defect detection system consisting of high-resolution cameras that in output provides a detailed report for each processed layer and a high-precision electronic beam autocalibration system.

**Powder management unit**

Once the production phase is finished and the build tank is removed, but also during the preparation of the machine, it is necessary to remove the excess powder in the working environment, as this can be recycled and reused after mixing with the virgin powder. To do this, special ATEX-classified standard vacuum cleaners are used for both recyclable powder and those outside the work environment (not recyclable as it is contaminated) [12]. Arcam offers a complete solution for powder management, as once the piece is produced, it is led to an ATEX-classified powder recovery station (PRS), where the excess is evacuated and then recovered [12].

### 2.1.3 EBM process

As already mentioned, electron beam melting is a very complex process because it involves several physical mechanisms that interact with each other, therefore these occur in a very short time interval focusing on the evolution of the single mechanism only on the transient phase. A description of functioning steps and a detailed overview of the various physical phenomena involved will now be presented, focusing on the main mechanisms that occur during the process.

**Phases of the process**

Once the powder bed has been prepared and the initial setup has been performed the machine is ready for the manufacturing process, which can be divided into the phases shown in Fig. 4 [13].

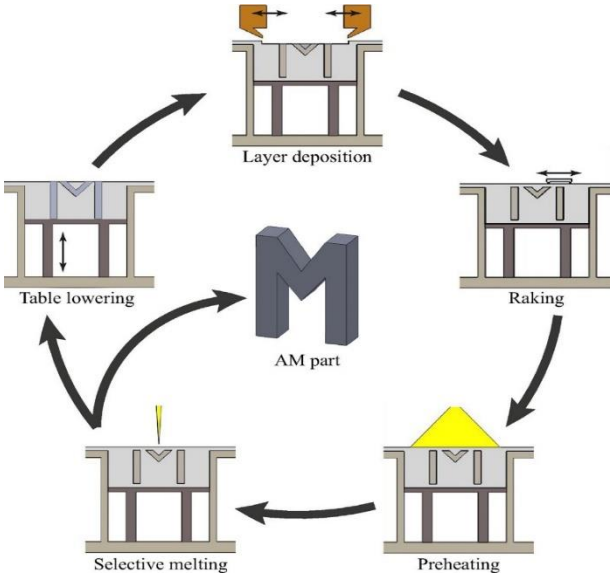


***Fig. 4*** *Phases of the EBM process.*

The first phase is the heating of the start plate by the defocused electron beam. The temperature reached by the start plate, before the first layer is added, depends on the powder material [13] and is monitored by a thermocouple connected to it. The first powder layer melted constitutes the base of the job, here in the interface zone the powder material and the start plate material undergo a metal connection that leads to microstructural transformations, scanning electron microscopy–energy dispersive X-ray spectroscopy (SEM-EDS) analysis conducted on TiAl specimens confirmed that [14], Fig. 5.

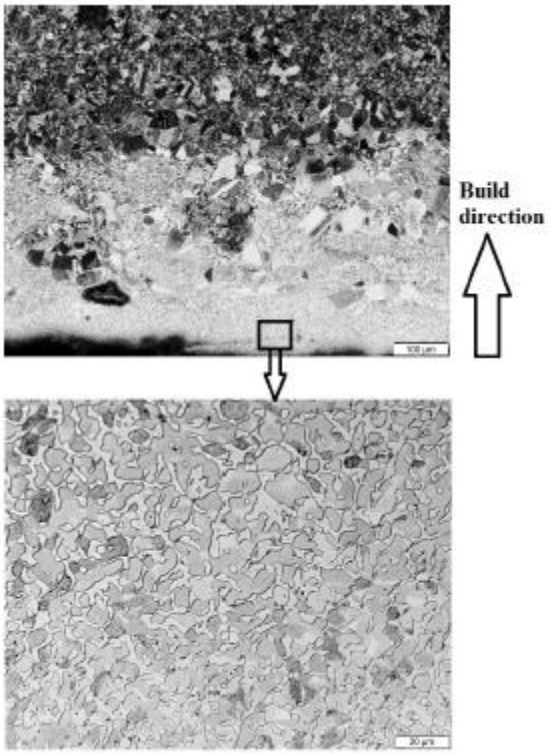


***Fig. 5*** *Microstructural interaction between the first layer melted and the start plate.*

The preheating is carried out after the deposition of the first powder layer. This is done with a series of defocused beam passages in which the power, which is the product between beam current and the acceleration voltage, is generally high (the current range controlled is 1-50 mA, in this phase it is increased linearly around 30 mA), and the scan speed also (around 15000 m/s).

During the melting phase the power and the scan speed are decreased (the beam current in this phase is kept constant), in this phase helium is blown to speed up the cooling process. The process is conducted in sequence by contour melting, and hatch melting in a selective area, driven by the section of the 3D CAD [15].

After the melting, the build tank is lowered by a height equal to the layer thickness used. Afterwards the rake distributes a new powder layer and the process phases are repeated until the building of the part is complete. Once the part is built, the helium pressure is increased to cool it [13]. The sintering of the powder, caused by the thermal environment, leads to a powder agglomeration around the part which

can be removed with a sandblasting process, using the same powder used for the realization of the part. Thanks to the very low oxygen pickup during the process, the unmolten powder can be recycled [13], however it is important to point out that the recyclability depends on the material used: for example in the study [16] it has been verified that the Inconel 718 powder can sustain a large number of cycles without replacement, while the Ti-6Al-4V powders are prone to pick up oxygen with increasing number of build cycles, therefore the recycling is limited, however in both case there is no significant change in the flowability, morphology, and size distributions. The growing oxygen pickup of Ti-6Al-4V powders is confirmed by the study [14] (legitimate from the high affinity of titanium with the oxygen), however for growing reuses a dimensional distortion has occurred, a decrease in the number of satellites and an increase in flowability, the latter is attributable to the excessive exposure to the vacuum that has reduced the moisture content. Other studies on Ti-6Al-4V powders [17] denounce negative effect of the recycling on mechanical and fatigue properties, obviously attributable to the growing oxygen pickup.

**Physical mechanisms**

It is essential to understand the physical mechanisms of the EBM process, which are complex and, as already mentioned, occur in a very short time interval [13], furthermore their interaction directly impacts the process and influences the properties of the processed material, therefore an optimal comprehension of the process helps both in selection of process parameters, and in the realization of the simulation model . The most important physical phenomena during EBM process are listed in Fig. 6 which show a three-dimensional mesoscopic simulation, by Matthias Markl and Carolin Körner, with the powder bed, the molten pool including the molten pool dynamics and the electron beam [2].

It can be said that among all the phenomena, the main one is the interaction between electrons and powder bed [13]. When the electrons hit the powder particles, most of their kinetic energy is converted into thermal energy, the rest is transformed into radiation and back-scattered electrons [13]. Depending on the energy of the electron beam, the powder particles are completely molten in the

range of a certain layer thickness [11]. The interaction between electron beam and powder particles leads many effects, however only a few of these play an important role in the process.

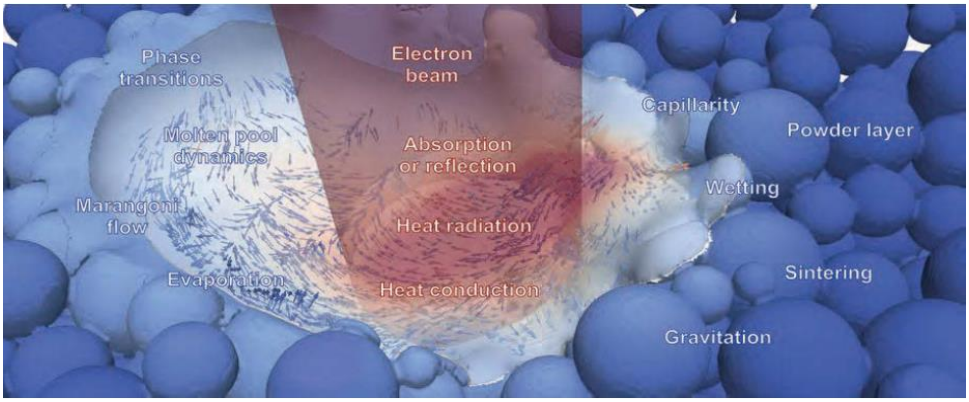


***Fig. 6*** *Most important physical phenomena during EBM process.*

**Spreading of the particles**

At the beginning of the development of electron beam sintering, the researchers, in the first few experiments of the process, noticed that the powder immediately spread, like in an explosion, as soon as it was hit by the electron beam [18]. This is known in literature as “pushing phenomenon” or “smoke” and when it occurs inevitably leads to the termination of the process. [2]. The photographs of a high-speed camera in Fig. 7 shows the development of the phenomenon. Researchers [13] agree that the possible cause for spreading could be limited to the following three: water residues in powder, momentum and electrostatic charge. In fact, electrons, during the accelerating voltage of 60kV, can reach speeds up to 0.5 times that of light and by the deceleration in the powder particles, the momentum of the electrons is transferred to powder particles, this could therefore be a cause of the spreading. This problem could be minimized by increasing the particle size [13].

The spreading could be caused by water residues or humidity in the powder (especially if the powders derive from a water atomization process), which could evaporate explosively when the electron beam hits the powder. This cause could be overcome by resorting to a gas atomization. On the other hand, the spreading of the particles could be attributed to the electrostatic repulsion: in fact this effect arises because when the beam hits the powder, there is an accumulation of electric negative charge in the powder bed, which cannot be dissipated and causes a mutual repulsive force among the particles that is several times greater than the weight of a particle, this could therefore be the cause of this explosion. Due to the slight sintering of the particles, during the preheating, it is possible to provide a certain electrical conductivity [2], this prevents the accumulation of negative charge in localized area of the powder bed and, thanks to helium blowing, the atoms of the gas are positively ionised by the electron beam allowing the dissipation of the negative charge from the powder bed [2].In general, the preheating phase, which leads to the sintering of the powder particles, causes the weight of the particles to be sufficient to hinder the repulsion of the particles [13], thus giving greater stability to the process.

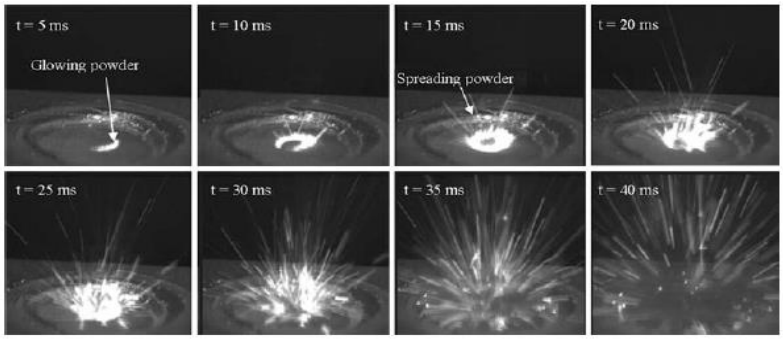


***Fig. 7*** *Photos from a high-speed camera that show the spreading of particles.*

**Preheating of the layer**

This phase is particularly important because involves the formation of physical changes and, as mentioned, gives a certain stability to the powder bed before the melting phase. The process parameters, during the preheating, are set in order to mitigate the amount of heat transferred to the powder layer using a high-power defocused beam at high speed [13]. As will be shown in the following paragraphs the penetration depth of the electron beam is relatively low and the energy of the beam rapidly decreases with depth, therefore following the transfer of the kinetic energy and the consequent transformation into thermal energy, the physical transformation of the powder inside the layer occurs thanks to the conduction mechanism. The preheating partially sinters the powder particles reducing the distance, furthermore due to sintering, interparticle circles are formed [13] as shown in Fig. 8, these represent a mechanical, thermal and electrical connection between the particles therefore allow the diffusion of the heat, of the electric charge and avoid the spreading [13]. In addition, these reduce the number of overhang supports for the realization of the parts.

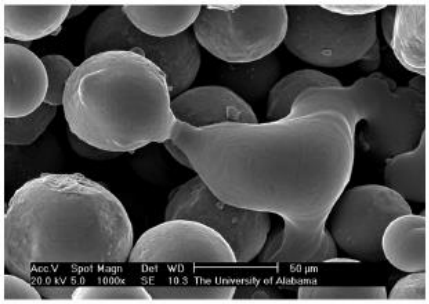


***Fig. 8*** *Interparticle circles due to sintering.*

**Melting of the powder**

As already mentioned, the main mechanism that promotes the thermal exchange, then the amount of heat into the powder bed, is conduction, but during the melting other heat exchange mechanisms take place, such as mass transport (convection), which induces a rapid sintering of the powder surrounding the melt pool. These

mechanisms occur in a very short time interval, since the life of the melt pool is short (only some milliseconds) [19]. The fusion begins when the temperature of the particle reached is higher than the melting one. When the fusion occurs, the volume reduces and the powder surrounding the melt pool, due both to the surface tensions and to the low viscosity of the molten metal, could be dragged into the melt pool [13, 19] . Variation between the liquidus and solidus temperature can influence the viscosity of the melt pool varying the shape of the tracks, then creating stochastic irregularity which leads to process irregularities [19]. An appropriate control of the molten flow, therefore the wetting of the solid phase by the liquid phase, is crucial for a good melting of the powder particles along the path of the beam [13]. The wetting characteristic refer to the intermolecular interaction between solid and liquid phases and to the balance between the cohesive and adhesive forces [13], they must be sufficient for the melt pool to wet the previous consolidated material and the powder particles [19]. The wettability depends on surface tension, material temperature, impurities, contamination and atmosphere [19] in particular, it can be defined by the "contact angle" Fig. 9 which is the angle measured between the solid surface and the tangent to the surface of the liquid at the point of contact [13, 20], if this angle is greater than 90°, wettability is limited, the cohesive forces increase and the surface tension is maximized, instead if it is lower than 90°, the adhesive forces increase and wetting characteristics improve [13].

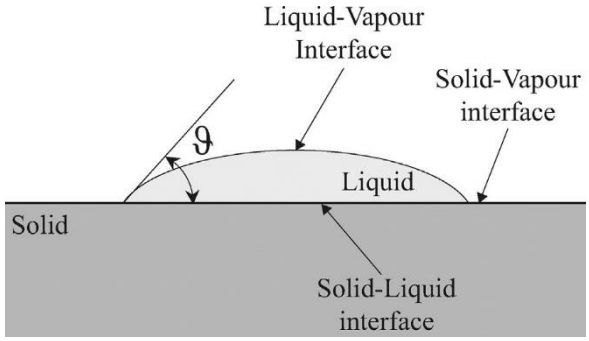


***Fig. 9*** *Contact angle.*

If the liquid phase and the solid phase have the same temperature there is no driving force for wetting, then the process parameters must be chosen to provide an excess energy in order to ensure a sufficient re-melting of the bulk and continuity of solid-liquid interface [13,19], however this energy increase leads to thermal gradients that feed mass transport with unwanted consequences, in particular the temperature distribution inside the melt pool leads to the generation of flotation forces, while the surface temperature distribution causes thermo-capillarity flows known as Marangoni flows [13,19] which affect the quality of the upper surface of melt pool. The flow instabilities can lead to the "balling" phenomenon also known as "Rayleigh instability", which is the breaking of the melt pool into spherical droplets [13,19], this affect the roughness of the solidified track and in extreme cases it can lead to the failure of the process [13].
Densification occurs as the result of the rearrangement of solid particles under the influence of capillary forces exerted on them by the wetting liquid [20].

**Post-heating**

After the melting phase, a post-heating phase may or may not be present. If this is not present there is no beam, therefore the bulk cools for a time equal to the duration of absence of the beam. In the event that post-heating is present, this is performed with a scanning strategy and different process parameters with respect to the previous phases. This phase promotes the growth of crystalline grains, being a heat treatment (annealing) [21]. Furthermore, it involves the reduction of process defects, for example the dislocations induced by thermal loads. Finally, it determines the final microstructure and its mechanical properties.

**Evaporation of alloying lightweight elements**

One of the most important phenomena that requires a careful management of process parameters in EBM is the evaporation of the molten metal caused by an excess amount of energy provided to the powder particles [13]. This phenomenon is governed by the mass transport of atoms from the inside of the molten material to its surface, by the phase change to gas and their consequent mass transport, and finally by condensation [19]. The high vacuum environment of the build chamber

decreases the evaporation temperature promoting the evaporation of alloying lightweight element, therefore the final parts and the recycled powder may have a reduced content of alloying elements.

**Variation of local distribution of the elements**

Another problem, which affects some alloys such as titanium aluminide, is the not uniform distribution of alloying element inside the part after her realization. The layered nature of the process together probably is the main cause of this phenomenon [22], but there is also to consider the interaction between the various layers in fact the short life of the aforesaid processes may not induce an appropriate mixing of the melt pool. However, it is the opinion of some researchers that the root of this problem is the same as the evaporation of lightweight elements, i.e. that is an excessive amount of heat supplied to the powder, which would cause a migration of these elements towards the surface of the melt pool and leads to the formation of bands with several microstructural consequences.

## 2.2 Introduction to numerical simulation

Increasing computing powers together with the software improvements have allowed engineers to deal with increasingly complex problems [23]. Some aspect, mainly economic, have determined a growing interest in computer-aided simulation, which today represent a very powerful software tool as it allows to reproduce in digital scale a specific process by means of a model, avoiding the costs to performing the same operations in laboratory. This tool takes a high added value in a business context, especially in industry 4.0, therefore it must be customized and properly calibrated with the calculator that allows its use, allowing results in a reasonable time and without excessive costs. Today the use of simulation allows the understanding of many scientific realities by providing predictive analyses of complex systems or processes that are difficult to reproduce such as EBM. The approach adopted is to relate different mathematical models that allow, based on some input variables considered important for the phenomenon

which must be reproduced, the calculation of certain useful outputs to achieve a specific purpose.

### 2.2.1 Fundamentals

Some key words used in the text will now be defined. A *simulation* is the replication in digital scale of the behaviour of a real process/system that evolves over time. A *model* is an abstraction of a real/conceptual system which is designed to display significant features and characteristics of the system which one wishes to study, predict, modify or control [24]. It is important to point out that a model includes some, but not all, aspects of the system being modelled [24].
The models will be defined "deterministic" if they do not contain any probabilistic component and "stochastic" if instead they admit some random inputs.

### 2.2.2 Targets

As already mentioned, the simulation constitutes a powerful tool for the optimization of an industrial process, i.e. for the choice of the best set of process parameters to achieve a given objective, however, like all aid tools, it must be implemented correctly and properly calibrated to achieve the desired results. Moreover, this tool must be able to give the desired results, i.e. an exhaustive representation of the EBM process, in a short time, so that it can be inserted in the development cycle of an industrial product, and without additional costs.
As will be seen in the following paragraphs, the level of detail of the simulation model assumes considerable importance, since, based on this, the time to obtain the results will vary, hence it is necessary to find the appropriate compromise between level of detail and time of analysis. Furthermore, since the process in question is very complex, it will involve different phenomena, so the simulation model will consist of several components. None of these components should be a bottleneck for the entire system.
To ensure a given level of reliability, the simulation model must be based on solid analytical models so that it can range across the entire domain of solutions and to ensure an adequate repeatability of results.

Finally, to facilitate the use of the instrument, therefore allowing the setting of the parameters in time, it is advisable to create an adequate graphical user interface (GUI) to provide support for user decisions.

### 2.2.3 Advantages and limits

The development and diffusion of 4.0 technologies combined with the digitalisation of industrial systems, requires increasingly complex calculation tools, so attention is growing towards advanced design techniques [23]. In the specific case, this concerns both the EBM process and in general all the last generation processes. In this context, process simulation is acquiring an increasingly significant role as it allows predictive analysis of the process. One of the main motivations for developing a simulation model is that it is an inexpensive way to gain important insights when the costs, risks or logistics of manipulating the real system of interest are prohibitive [24]. Simulating the process is a way to investigate it in detail and also to increase its efficiency and potential, in fact the main reason why simulation of EBM is used, is to reduce the optimization time of the process itself respect to the traditional try and error approach. The simulation allows to test the multiple operating conditions of the production system which are often too expensive, furthermore, this leads to a reduction in development costs, the ability to evaluate a greater number of alternatives effectively and quickly, the capacity to explore new possibilities [23]. Moreover, the preventive study of the process offered by the simulation, allows the identification of any process problems or in any case the cause-effect relationship of events. With reference to the EBM process, which, as discussed in the previous paragraphs, takes place in an environment not accessible by measurement tools other than those of the system itself, the simulation of the process offers the capacity to make estimates that cannot be measured on the real system and repeatability of the results at low cost. Finally, through appropriate sensitivity analyses it is possible to modify the hypotheses, algorithms, or structure of the simulation model to study its effects.

However, even the simulation has its limits, which can be referred both to a general context and to the company context. As far as the general limits are concerned, it is important to emphasize that it is not possible to exactly replicate a given process since the computational cost would be too high and the amount of data to be managed by the calculator would be too high. Another limitation, intrinsic to the model itself, can be, for example, the difficulty of sensitivity analysis or the interpretability of the results obtained, or the fact that displaying results is not easy. In a business context, however, the main limits of simulation often converge to the time factor. One of the main problems is that the run times of the analysis are too high, even if the model is optimized, and to reduce them it is necessary to lower the level of detail, at this time the times of validation and experimentation are being added.

### 2.2.4 Degrees of freedom in EBM process

The effort of researchers to model the EBM process is due to its complexity, but also because it involves a several number of process parameters, whose incomplete control may compromise the success of the operation. In fact, the parts are only near-net-shaped since they do not satisfy the surface roughness and dimensional accuracy requirements. The incomplete control of the process can also lead to the formation of defects which in some cases can be of minor importance, such as porosities, inclusion or geometrical deviances, which can be minimized by hip treatments and machining even if they increase the waste rate, while in other more serious cases, such as delamination or balling, they can lead to the failure of the process [13].

The first years of development of EBM technology saw the application of the try and error approach for the optimisation of process parameters, i.e. reducing the process deficiency by the process calibration on the case study. However, this approach is radically wrong considering that the process is optimized on the material and geometry in question, therefore in addition to the incomplete control of all the process parameters the range of validity of the results is restricted to a narrow window of values investigated in the study. Instead in the last few years

different simulation models have been developed, trying more and more to understand the physical phenomena behind it, and spacing the whole domain of process parameters, thus making the EBM process more reliable [13].

According to literature [13] the main process parameters are the following:

- **acceleration voltage**: which is typically kept constant at 60kV.
- **intensity of the beam current:** it is usually controlled in the range 1-50 mA, together with the focus offset jointly control the beam diameter which, according to literature, can be focused down to 0.100 mm [25].
- **focus offset (FO):** is the additional current running through the respective coil and can be translated into an offset of the focal plane from its zero position [13]. With a blurred beam the energy is dissipated over a wider area, reducing the fusion capacity, thus leading to possible unmelted regions [26].
- **layer thickness**: it is variable in the range 0.05 to 0.02 mm.
- **scan speed:** it can be set directly or by the speed function index [13]: the speed function index (SF), which can range between discrete values of -10 to 200 [11], is used to control the translational speed of the electron beam during the fabrication of the part. No information about the speed function algorithm is available in literature or has been disclosed by the Arcam company, but this parameter seems to affect the instantaneous scan speed value of the electron beam [11, 13].
- **scanning strategy:** it indicates the scanning process and the scanning mode: the first one consists of pre-heating, melting and post-heating (where the current and the scanning speed are kept high to allow a better dimensional accuracy, thus uniforming the temperature field and therefore a lower solidification shrinkage), the second one defines the path of the electron beam, in particular, after the preheating phase, the 2D section slice of the part is realized in two steps: contouring and internal filling [27, 28]. The contouring is used to improve the surface finish of the part [27], the melt strategy used exploits a technology known as MultiBeam, which rapidly moves the beam so as to keep several separate melt pools active at one time, generally three contour passes are made as shown in Fig. 10,

moreover in the outer contour pass each melt pool is translated more slowly and with a lower power than for the inner two [28]. The internal filling is usually made by a back and forth raster pattern, with a continuous path, according to a "snaking" melt strategy known as "hatching" [27, 28] which is adjusted by means of the "line offset" parameter or "hatch distance" i.e. the distance between two parallel lines. A high line offset can lead to insufficient fusion of the powder between the scan lines [26]. This scanning mode has some advantages, such as no vacancy path, a simple algorithm, an isotropy microstructure moreover the change in direction of the electron beam will be relatively smooth and will not push the powder away from the original positions [29].The beam current during hatching is calculated by the EBM control software and varied linearly with the length of the hatch line while the speed function tries to keep a constant melt pool depth by maintaining an approximate constant ratio of power and scan speed, moreover when the beam reverses direction, a "turning function" automatically increases the beam speed, to avoid overheating the already hot recently melted area and the focus diameter is also adjusted by the focus offset [28].

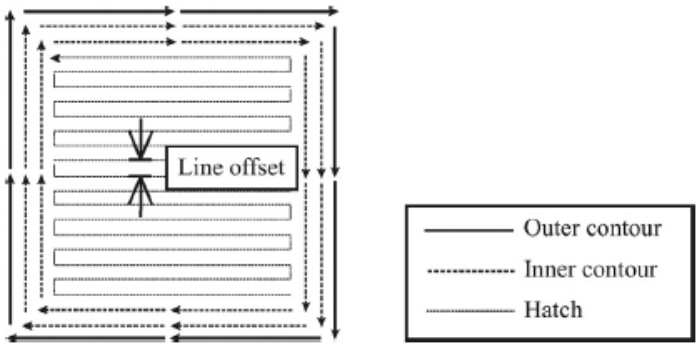


.

***Fig. 10*** *Contouring and hatching.*

Finally, in literature it is possible to find some parameters obtained by normalizing process parameters, used by the machine control software, respect to known quantities such as “line energy” [30] which is the ratio between the beam power and the scan speed, “area energy” [31] which is the line energy normalized respect to the line offset, “energy density” [32]which is the ratio between the power and the section of the beam. However, it is important to point out that among the three derived parameters the last is the most representative as it normalizes respect to the beam diameter, while for example the energy area, normalizing the amount of heat supplied respect to the line offset, does not take into account the possible overlap of two adjacent passes as shown in Fig. 11.

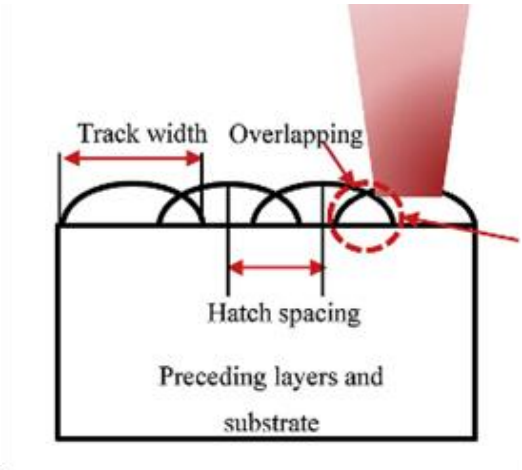


***Fig. 11*** *Schematic representation of overlapping of two adjacent scan lines.*

## 2.3 State of the art on numerical simulation of EBM process

In this section the main numerical simulation models present in the literature will be presented, highlighting the main aspects and critical issues, evaluating at last their applicability in a typical business context. The classification of the simulation models of the EBM process is rather complex and mainly refers to the work conducted by M. Galati et al. [13] reporting an update on the most recent models present in the literature. The models belonging to the same category will be

presented in chronological order, so that a comparison can be made between them regarding the improvements made. Finally, the results of the simulation of each model will be discussed, thus highlighting the main aspects

### 2.3.1 Single-track, single-layer and multi-layer models

In general, the EBM process simulation models can be divided into three macro-categories: single-track models, single-layer models/multi-track models and multi-layer models. As the name itself suggests, the models belonging to the first category allow simulating only a single scan line, the latter allow simulating several o all the scan lines belonging to the same layer, while the third allow simulation of the EBM process for some or all the layers needed to make a part.

Obviously, the level of complexity and the level of detail of the model increase by passing from the first to the third category as well as the necessary computational power increases, therefore the runtime increases since a greater quantity of data must be processed. However, it is possible to use software expedients that allow a considerable reduction in run time.

As was discussed in the section dedicated to the EBM process, it is reasonable to say that the use of a single layer model is not enough to represent the process with a sufficient level of detail since there is a mutual interaction between the layers. However, in order to optimize the parameters of the EBM process, during the creation of the model, it is advisable define an adequate level of detail in accordance with the set objectives of the simulation to achieve.

### 2.3.2 Black box, grey box and white box models

The model present in literature can be grouped in three main categories depending on the level of detail in representing the physical phenomena that occur during the EBM process: black box models, grey box models and white box models. As shown in Fig. 12, the level of detail of a simulation model increases moving from the black box models to the white box models. The greater the level of detail with which the model is created, the greater the physical meaning explained and the

complexity of the model, however there will be a greater amount of data to be processed therefore the computational cost will increase and consequently also the run time required for the simulation, moreover the possible sources of error will be greater and more effort will be needed for calibration. Obviously, there will be no purely black box or white box models, but models whose structure and characteristics tend to these limit conditions.

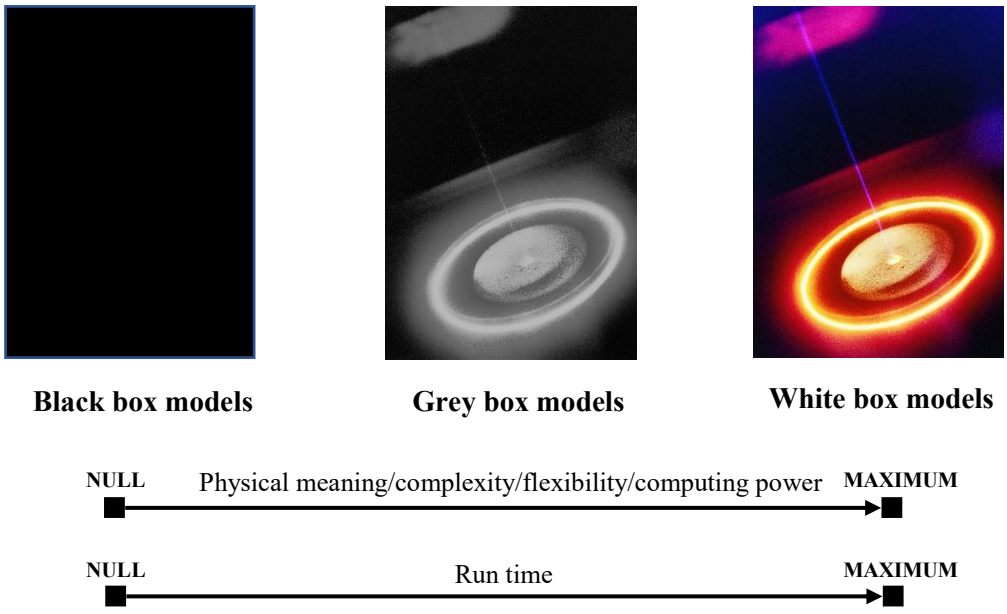


***Fig. 12*** *Characteristics of black box, grey box and white box models.*

**Quasi-black box models**

The models tending to the limit black box, as already mentioned, have a low level of detail, since they solve a numerical problem without referring to any underlying physics [13], so the main advantage they have is a very low run time. These models take the form of a set of transfer parameters or empirical rules that correlate the outputs to the inputs of the model. Few models are present in the literature, as an example we report the work conducted by M.F. Zah and S. Lutzmann [33], in which is reported a mathematical model in terms of the temperature distribution during scanning, based on the heat conduction equation opportunely modified according to the load and the boundary conditions. The equations have been implemented into a FE-solver under consideration of an idealised geometry.

Another quasi-black box model present in literature was developed by G. M. Mladenov et al. [34], in which is presented a simple analytical model of a moving energy beam on a powder layer and the use of dimensionless parameters for the reduction of the total number of considered variables. Although the model has been adapted from models of the electron beam welding process (EBW) present in the literature, thus considering different physical phenomena with respect to EBM, it can be considered a black box model because the level of detail and the physical meaning adopted is very low.

**Quasi-white box models**

The quasi-white box models have a high level of detail, this allows them to replicate the phenomenon in question with a very low level of approximation, therefore they are very complex with a high level of flexibility. The drawbacks of these models are the high run time due to the large amount of data to be managed, and, since the components of the model will be more integrated, the increase of sources error. In the literature there are no quasi-white box models. This is permissible as often the results of the simulation are desired in a short time therefore the researchers prefer to implement models belonging to the first two categories. However, as will be discussed, some grey box models have some features that make them prone to white box, achieving a greater level of detail at the expense of run time.

## 2.4 Grey box models

In this section the main grey box models present in the literature, which represent most of the simulation models of the EBM process, will be presented. These models, as already mentioned, have intermediate characteristics compared to black box and white box models, however they can have one or more elements that allow them to tend to one of the two extremes.

The grey box models can be divided into three main categories depending on how the powder is modelled: micro-scale models, meso-scale and macro-scale models, as shown in Fig.13. A fourth category is represented by multi-scale models that integrate one or more of the previous categories.

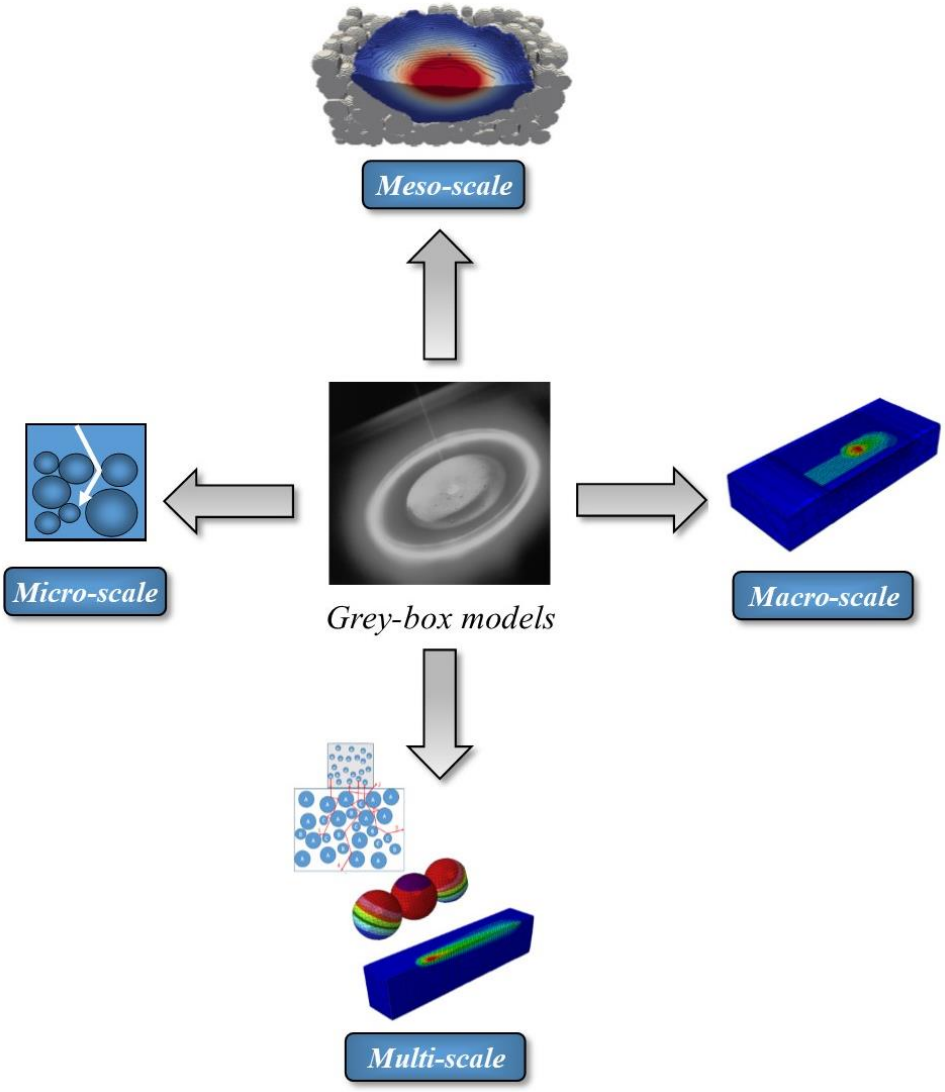


***Fig.13*** *Classification of grey-box models.*

### 2.4.1 Micro-scale models

To this category belong the models that allow to simulate the micro-scale aspects of the EBM process. One of these is represented by the interaction between the electron beam and the powder bed, which makes it possible to make opportune considerations useful for modelling the thermal source. The heating of a powder bed or a substrate is the result of interaction between electrons and material atoms. The electrons impinge the material and then collide elastically or inelastically with

the material atoms, resulting in energy transfer from the electrons to the material. [35].

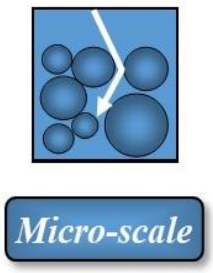


- ***M. Galati, W. Yan***
  *Interaction between electron beam and powder layer*
- ***A. T. Olanipekun***
  *Evolution of the dendritic growth during solidification*

*(Micro-scale aspects of EBM process)*

***Fig. 14*** *Micro-scale models, classification.*

As an example, the first attempt to reproduce the interaction electron-material using a Monte Carlo simulation has been carried out in the model developed by M. Galati et al. [29] about the modelling of the heat source. Another work was developed by W. Yan [35, 36] (section multi-scale models) which also used a Monte Carlo simulation as shown in **Errore. L'origine riferimento non è stata trovata.**. The Monte Carlo was also used by et al. [30] which they developed a MATLAB code to solve the set of Time-Dependent Ginzburg–Landau equation phase field equations and simulate the evolution of the dendritic growth during solidification in EBM of Ti-6Al-4V.

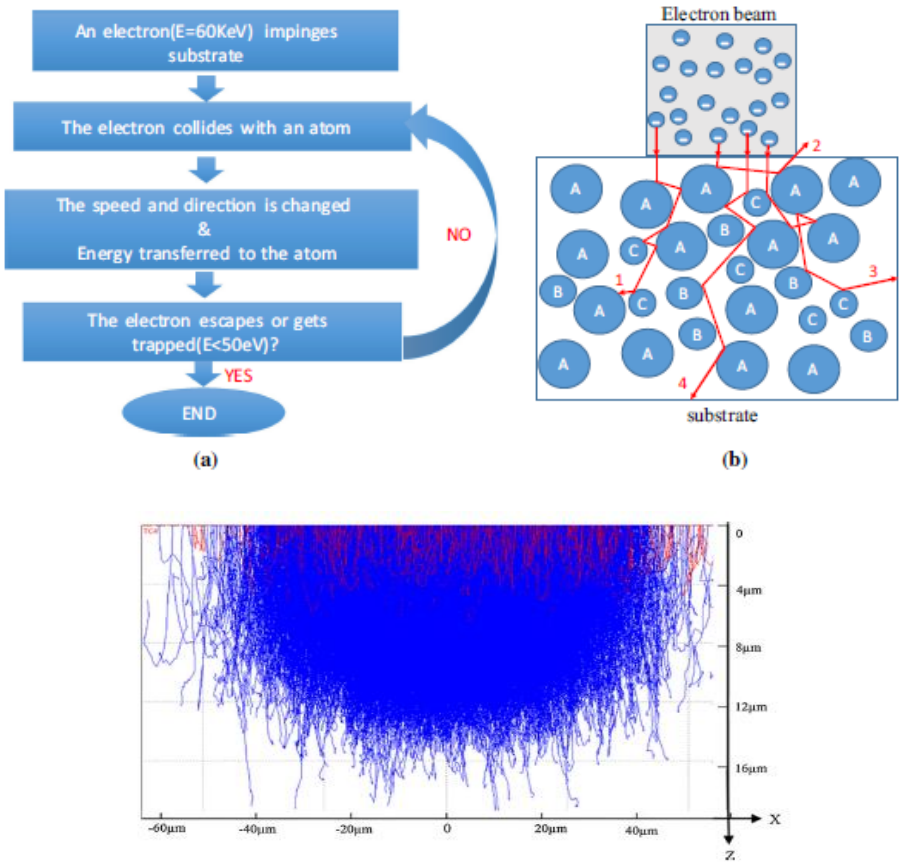


***Fig. 15*** *Monte Carlo simulation of electrons trajectory inside the powder particles.*

### 2.4.2 Meso-scale models

Mesoscale or mesoscopic modelling covers a wide range of models which objective is to study length-scales and timescales that are not easily accessible to either micro-scale or macro-scale methods [37]. The most common approach to modelling a process is through a continuous model (macro-scale), however often the small-scale features of the problem cannot be ignored, moreover the possibility of considering them making the mesh sufficiently fine is computationally prohibitive [37]. Furthermore, often the small-scale elements dominate the process to be simulated and their level of detail and their temporal evolution determine the actual properties required by the simulation [37].

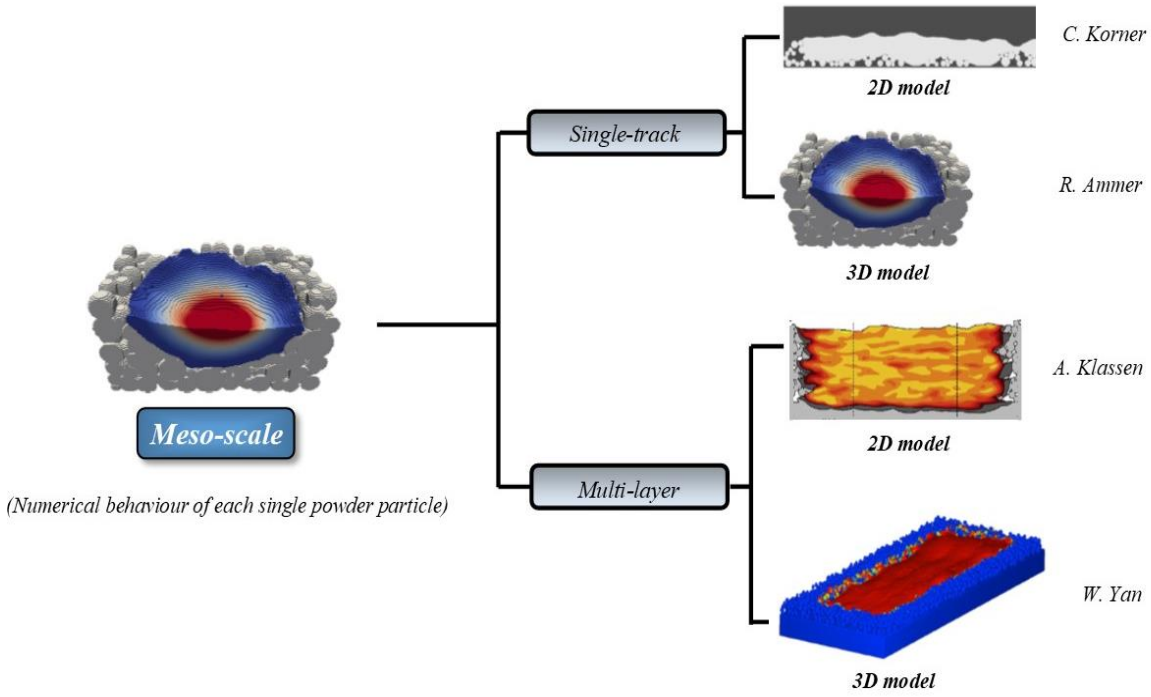


***Fig.16*** *Meso-scale models, classification.*

In the case of the EBM process the small-scale element of the model is powder. In this sense, some researchers believe that a mesoscopic powder modelling approach is necessary to give an adequate level of detail to the model.

- ***Single-track models***

  The first attempt of modelling the EBM process according to a mesoscopic approach was conducted by Professor Korner's research group [19, 30]. The author justifies the application of a mesoscopic approach based on the work carried out by the researchers up to that time, who, using mainly continuous approaches, assumed powder particles as a homogeneous material whose properties depended on the relative density, moreover, the modelling of the shrinkage of the powder during the fusion (around 50%), which greatly influences the geometry of the melt pool and the local thermal properties, in the continuous powder models present at that time was only dependent on the packing density of the powder and not on a real random powder bed.

Thus, the resulting melt pool geometries were defined without the stochastic behaviour observed experimentally. Therefore the research group, to meet these needs, develops a 2D mesoscopic model based on the lattice Boltzmann method (LBM) [38, 39, 40, 41], which is an alternative to the normal models of computational fluid dynamics, particularly useful for problems with complex interfaces such as flows in porous media. Moreover, by means of an algorithm, randomly packaged 2D layers of spherical powder are generated, that during the absorption of the electronic beam lead to complex and highly changeable geometries of the melt pool. The model allows to predict local powder melting and re-solidification processes on the powder level in 2D focusing mainly on physical mechanisms like wetting, capillary forces and materials parameters like the stochasticity of the powder bed. The simulations show that the packing density of the powder bed significantly influence the melt pool characteristics as shown in Fig. 18. Moreover, the line energy dominates the processing results at constant powder packing density Fig. 18.

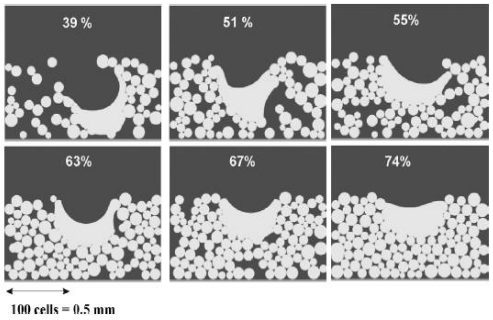


***Fig. 18*** *Influence of packing density of powder bed on melt pool characteristics*.

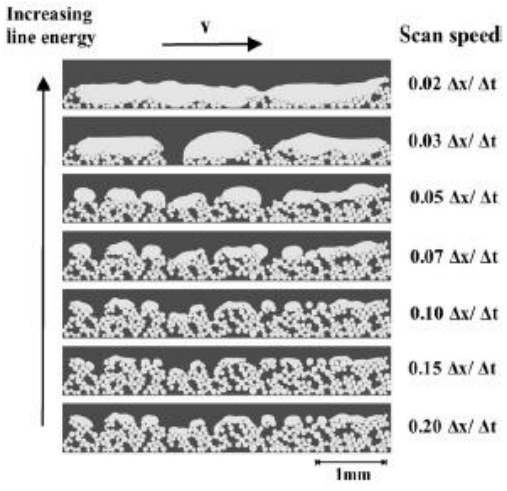


***Fig. 18*** *Influence of line energy on melt pool characteristics.*

Due to the low level of approximation and the high accuracy of the simulation the model is very complex and expensive in terms of run time and computational power, therefore not suitable for large-scale simulations [13].

An improvement on the previous model is due to R. Ammer et al. [42, 43] which develop a thermal 3D free surface lattice Boltzmann (LB) model. The implementation was integrated in the waLBERLA framework, a widely applicable lattice Boltzmann solver. The model includes hydrodynamic physical effects (the flow of the melt pool) and thermal effects (beam absorption, melting and solidification), however 3d simulations (Fig. 19) require a high computational power, thus an optimization of the program is required [42].

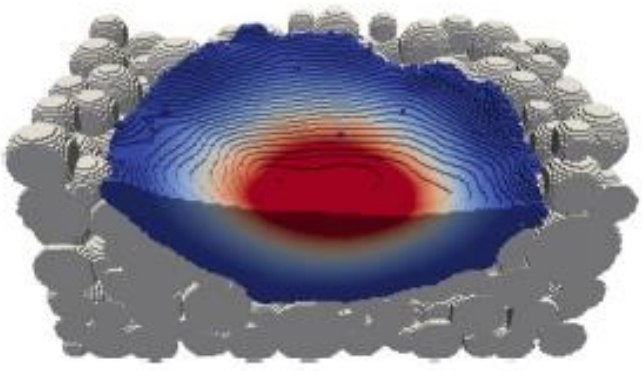

***Fig. 19*** *Thermal 3D free surface LB model by R. Ammer* [42].

- ***Multi-layer models***

  A third evolution of prof. Korner's model was presented in 2017 by A. Klassen et al. [44, 45, 46], in particular was developed an evaporation model, based on the lattice Boltzmann method, for multi-component systems that is capable of predicting heat release at the melt surface, selective loss of mass and recoil forces onto the molten surface generated by the expanding vapour. Like the predecessor models the model includes electron beam absorption, stochastic powder particle distribution and melt

pool movement. The simulations were carried out in 2D. This model is particularly useful when processing metals with light alloy elements such as titanium aluminides, so when the evaporation of a component is significant with consequences for the distribution of these elements along the build direction.

The model was used to understand the impact of powder consolidation and evaporation on alloy composition during selective electron beam melting of Ti-48Al-2Cr-2Nb. The simulations demonstrated that the irregular powder packing, which generates stochastic variation in the deposited powder distribution and in the layer thickness, influences, respect to an idealized compact powder bed, the aluminium distribution and content in the final part as shown in Fig. 20.

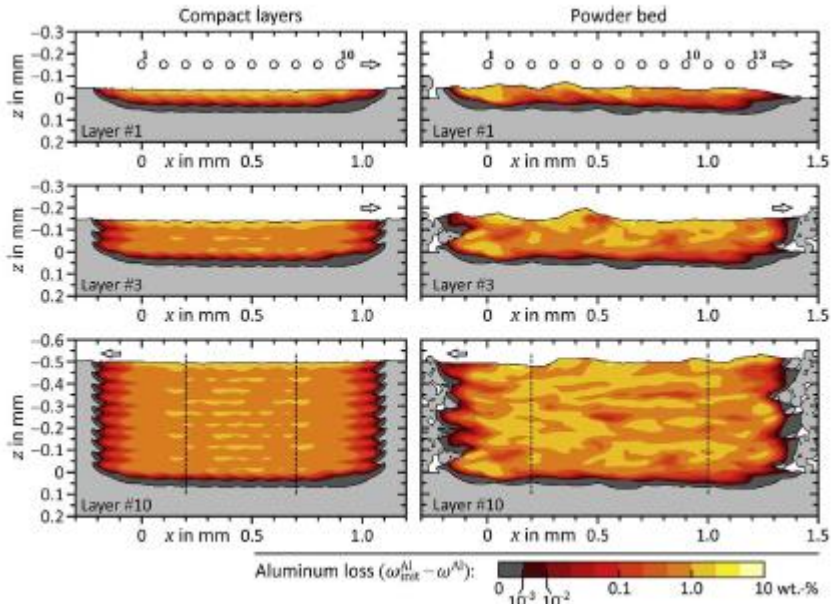


***Fig. 20*** *Comparison of stochastic irregularities generated by a compact powder bed on the left and by a powder bed with irregular packing on the right.*

Furthermore, it has been shown that line energy is the parameter that most influences evaporation, in particular for high scanning speeds in conjunction with a small line offset lead to a significant reduction in evaporation of alloying elements.

Recently a meso-scale model was developed by W. Yan et al. [47] starting from the presupposition that, in accordance with the work of the predecessors, a model that simulated the interaction of the rack with the powder bed, therefore the complete laying of the powder bed, had not yet been developed. In fact, the rain drop model which generates each powder layer, developed by prof. Korner's research group [30], does not fully consider the mechanical interaction between particles and rake, therefore the relative density of the powder bed is higher than in reality [47]. Moreover, since some predecessors developed only single-track model, neglecting the interaction between track and between layers, the integrated modelling framework proposed by W. Yan et al. [47] allows simulation of two successive steps: laying and selective melting of the powder bed, as shown in Fig. 21.

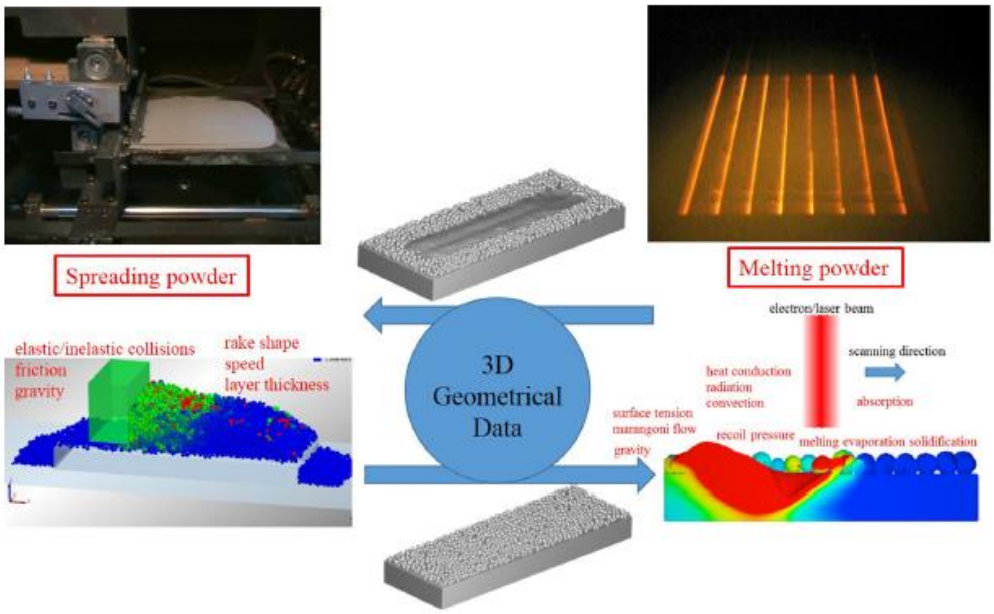


***Fig. 21*** *Logical scheme of the model developed by W. Yan* [47].

For the laying of the powder bed is used a model based on Discrete Element Method (DEM) which simulates the frictional contact and collision both

between particles and with the rake and substrate [47]; for the selective melting of the powder bed is used a thermal-fluid flow model, which captures the material evolution process, heat transfer, phase change, and molten pool flow [47]; the simulations are repeated according to a multi-layer and multi-track implementation which allows to predict the formation of inter-track and inter-layer voids to optimize the scan path, as shown in Fig. 22. The study, according to the results of the simulation, showed that the voids are generated edge regions of the part, this can be avoided by acting on contour scan strategy, moreover, it is possible predicting the position of voids according to scan strategy used [47]. This too, like all the powder mesoscopic models, deserves improvements in terms of computational efficiency.

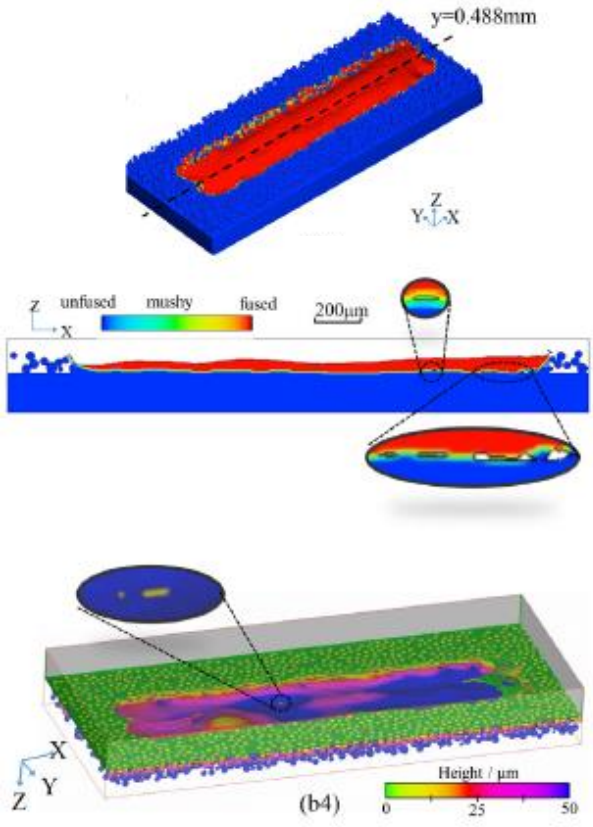


***Fig. 22*** *Inter-track and inter-layer voids generated from simulation.*

### 2.4.3 Macro-scale models

The main reasons why mesoscopic models are not suitable for large-scale simulation have been listed in the previous sections. These reasons have led researchers to model the powder as a continuum media, in order to use the finite difference method (FDM), finite element method (FEM) or finite volume method (FVM) and thus reduce the calculation time [13]. Although the use of aforementioned approaches was criticized by some researchers, about the low level of detail with which to represent the phenomenon (i.e. the stochasticity of the powder bed that influences the geometry of the melt pool), recently the use of integrated numerical expedients in the solvers it attenuated the gap between the two types of approaches.

The main difficulty of using a macro-scale approach was to implement a suitable model of the powder and the change of its properties by melting and subsequent solidification. The macro-scale models can be classified according to whether the solvers are used individually or coupled with other different solvers. It is possible to distinguish: uncoupled models, weakly coupled models, coupled models.

The heat exchange that takes place during the EBM process involves only the conduction mechanism (through the powder and between powder and bulk substrate) and the radiation one (from the powder bed to the build chamber), moreover, due to the high scan speed of the electron beam, the phase change occurs in a very short time [13]. In addition to the principal mechanisms that generate heat exchange, as has been discussed in the previous sections, there are dissipative phenomena such as the Marangoni convection or the dissipations induced by the viscous forces that generate flows out of the melt pool towards the build chamber and therefore should be included in the thermal balance equations. The approach followed by the uncoupled models is based on the use of an uncoupled heat transfer analysis in order to calculate the temperature distribution (using of FE or FD solvers), where a perfect wettability is generally assumed so as to neglect thermo-fluid dynamic dissipations [13]. A second approach used in coupled models is based on coupled thermo-fluid analysis (then using thermal-fluid flow models) which considers thermo-fluid dynamic dissipations in the global thermal balance to calculate the temperature field.

The key concept of macro-scale models is that, during the numerical simulation, the material properties specified in the heat transfer equations should be changed during the heat transfer analysis, according to the temperature reached [13]: at the beginning of the process the thermophysical properties must be those of the powder; when the temperature is higher than the melting point, and the powder is thus melted, the powder thermo-physical properties should be the same as those of the liquid metal properties; after the melting, and during the cooling phase, the thermophysical properties should be those of the bulk [13]. Definitely, the thermal behaviour of the material is a function of the temperature and of the state of the material [13].

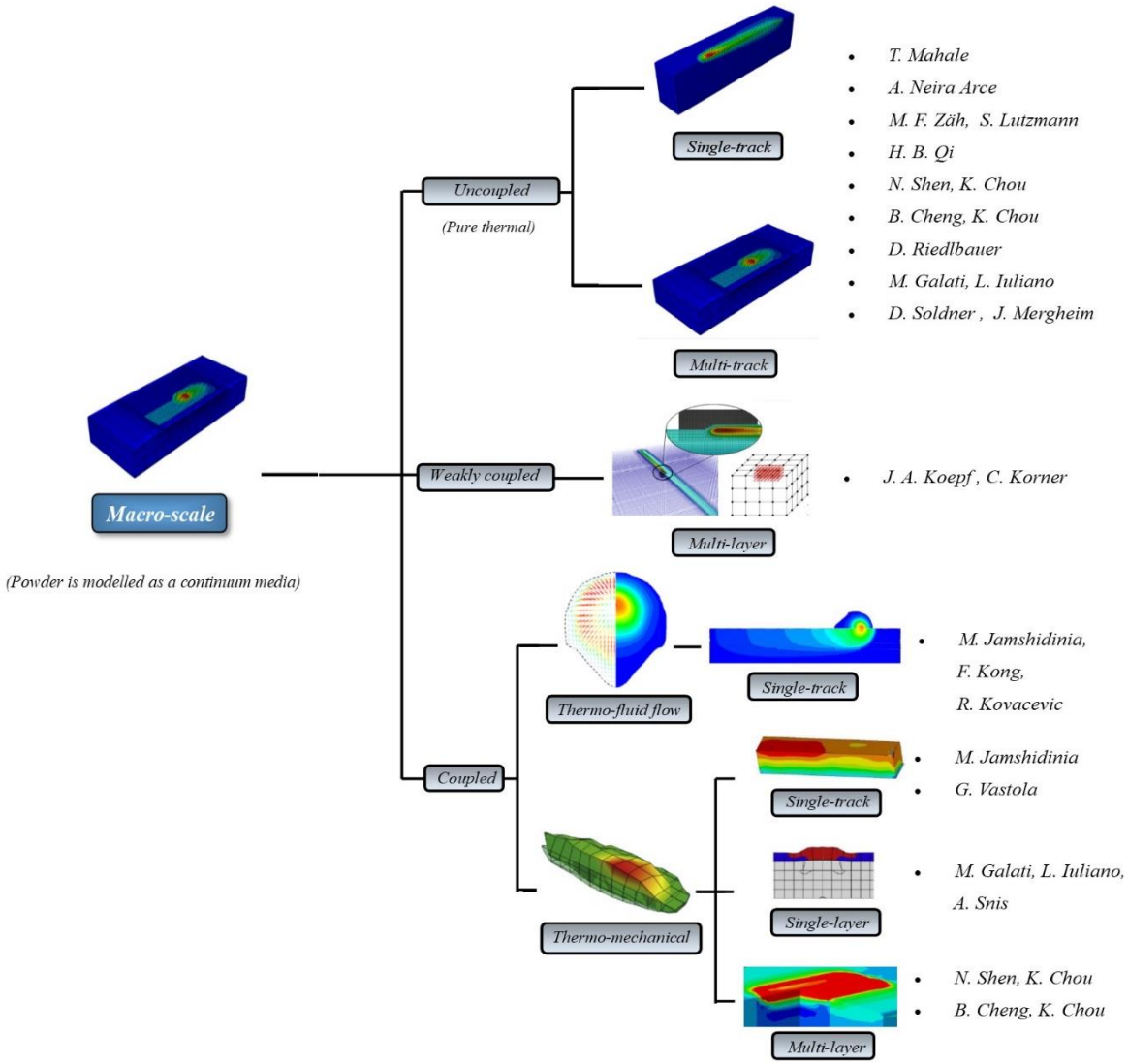


***Fig.23*** *Macro-scale models, classification.*

**Uncoupled models**

In the uncoupled models, also called "pure thermal models", a single thermal solver (FD or FE) is used to simulate the temperature field in the domain of interest. In general, the development of an uncoupled thermal model is carried out starting from a general analytical model of heat transfer, on which appropriate hypotheses will be carried out for the properties of the material, for the material state change and for modelling the heat source.

One of the first attempt of modelling the EBM process with a macro-scale approach was conducted by T. Mahale [11] and Neira Arce A. [48] using FD and FE-solvers to analyse the thermal problem in small subdomains called “voxels”. In summary, planar energy source acts over a voxel, which represents the melt pool location at a specific place in time with time-dependent boundary conditions [13], therefore is subjected to a prescribed heat flux until the domain reaches the material melting point at an arbitrary temperature above the melting point [13]. The voxels that are not melted are assigned a thermal conductivity equal to zero in order to allow the voxel domains on the desired area to be solved [13]. In this model the change of properties has not been implemented therefore it will not be discussed in detail.

The main uncoupled models will now be presented, analysing their characteristics in terms of modelling assumptions for material properties and heat source according to M. Galati work [13].

*Material properties assumptions (**single layer/single track models**)*

Qi et al. [29] assumed that the powder density was equal to 64% of the bulk one, the solid thermal conductivity was considered as a linear function of porosity, the heat losses due to radiation were neglected and the material state change was not considered.

Zäh and Lutzmann [49] modelled the density, specific heat and conductivity of powder according to the method proposed by Zenher et al., the emissivity was considered constant and the material state change was not considered.

Shen e Chou [50] and Galati et al. [51] implemented a more accurate modelling. The density, specific heat and thermal conductivity as temperature dependent. The powder properties were calculated from those of the bulk: the specific heat and the latent heat of fusion were considered the same as those of the bulk, the porosity was used to reduce the density of the bulk and to simulate the apparent density of the powder layer. Conductivity was modelled according to the model by Tolochko et al. [52], assuming the body cubic center (BCC) packing of powders. In the model [50] the powder was considered packed randomly and emissivity was considered independent from temperature, and the Sih and Barlow's model [53] was used to approximate powder emissivity. Galati et al. [51] considered emissivity as temperature dependent calculable according to the BCC packing of the powder bed. Both models considered the material state change using user subroutines integrated to the solver, which work by means of material index (0 for powder and 1 for bulk), however different material change criteria were used.

Cheng et al. [54] in their model used the same material change criterion used by Shen e Chou [50],but no analytical formulation to calculate the material properties was used since the model was developed specifically for Ti-6Al-4V, in particular the conductivity was obtained applying the "series of heat conductance" concept and the radiation losses were neglected since the interested area by the heat flux is small.

In the model developed by Riedlbauer et al. [55] the consolidation of the powder was not modelled, then an effective powder layer thickness was assumed in the simulations starting from the relative density of the powder which was determined experimentally, equal to 58.3% of the bulk one. The density was assumed to be different for each material phase and temperature-independent, the emissivity and the material state change was not described clearly.

*Heat source modelling*

The researchers followed different approaches for modelling heat source, however all agree that the energy intensity depends on the power of the source and on the absorptivity of the material.

According to Qi et al. [29] the source was modelled by a uniform volumetric distribution of the heat that affects a single prismatic element.

Zah, Shen and Cheng [49, 50, 54] assumed the heat source intensity according to a Gaussian volumetric distribution, in particular as a conical heat source whose intensity decreases as the penetration depth increases.

Even Riedlbauer et al. [55] considered a volumetric heat source but they used a set of semiempirical equations taken from the A. Klassen's et al. [56] study in which the model model source was applied in an LBM simulation, taking into account absorption, transmission and backscattering.

In the study developed by M. Galati et al. [51] the heat source was modelled analysing the impact of the electron beam on the preheated powder bed by means of a Monte Carlo simulation of the electron trajectory. Based on numerical results the real heat flux was modelled as a uniform circular distribution on top of the surface, neglecting the penetration depth, and a correction coefficient of the global flux was introduced to take into account the real distribution of the electrons, which had a larger effective diameter than the nominal focus beam diameter.

*Improvement to existing models*

Based on the Riedlbauer's work [55], D. Soldner and J. Mergheim [57] developed an improvement of the existing model in term of computational efficiency. A first improvement was the use of adaptive mesh refinement in the regions currently exposed to the electron beam and a coarsening of other regions. A second improvement was the development of a multi-time stepping approach to solve the thermal problem accounting for the distinct scales in time, since the time step size of the model is constrained by the resolution of the beam path, which limits the size of the thermal problem. A third improvement was the use of a line input model.

**Weakly coupled models (*multi-layer models)***

The weakly coupled models are characterized by the coupling of a thermal solver (generally FEM) with another type of solver, in particular on the basis of the temperature field obtained from the first analysis it is possible to obtain a greater level of detail regarding the process simulated by performing further types of analysis. With regard to what has been found in the literature, these types of analyses aim to provide predictions in terms of the microstructure obtained. As an example, the work conducted by J. A. Koepf et al. [58] is reported, which based on the uncoupled model for SEBM developed in the work by D. Soldner and J. Mergheim [57]. The model consists of a coupling of a finite-element thermal solver with a cellular automata (CA), in particular the analysis is based on the iterative reuse of the thermal field for the simulation of the grain size, as shown in Fig. 24.

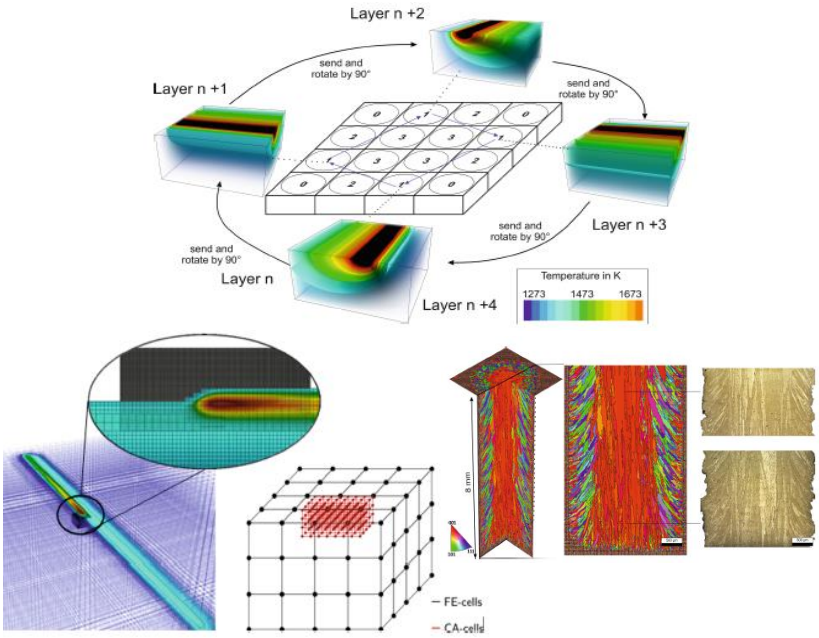


***Fig. 24** Iterative reuse of the thermal field for the simulation of the grain size by a weakly coupled FE-CA model by J.A. Koepf et al* [58].

However, the excessive computational cost requires the use of a high-performance cluster computer to decrease the run time.

The CA has been widely used in previous microstructural simulation work. For the microstructural simulation T. M. Rodgers et al. [59] presented a comparison of AM microstructure simulation methods reported in Tab. 1.

The table shows that the best compromise between computational cost and an adequate level of detail for the simulation of the microstructure is given by the Monte Carlo simulation.

***Tab. 1*** *Comparison of AM microstructure simulation methods*

| Method and Approx. Computational Cost | Benefits | Challenges |
|---|---|---|
| Cellular Automata-Finite Element (CAFE) (High) | • Provides coupled predictions of thermal behavior and microstructure.<br>• Incorporates crystallographic texture. | • Does not simulate solid-state grain evolution after solidification.<br>• Limited to few passes of a heat source.<br>• Free open-source code currently unavailable. |
| Cellular Automata-Lattice Boltzmann (High) | • Allows for coupled thermo-fluid and microstructure evolution on same lattice.<br>• Incorporates crystallographic texture. | • LB provides unstable solutions for many regimes.<br>• Does not simulate solid state grain evolution after solidification.<br>• Limited to few passes of a heat source.<br>• Free open-source code currently unavailable. |
| Monte Carlo (Medium) | • Predicts full 3D microstructures with hundreds of heat source passes.<br>• Approximates microstructure during solidification and solid-state grain evolution.<br>• Utilizes idealized molten zones, without the need to parameterize for specific material systems.<br>• Included in the open-source SPPARKS Monte Carlo suite. | • Does not allow for direct coupling of thermal and microstructural models.<br>• Quantitative ties to experimental conditions are less developed.<br>• Currently does not incorporate material texture or anisotropy. |
| Empirical Microstructure models (Low if thermal prediction exists, otherwise medium) | • Estimates microstructural features over large builds.<br>• Allows extension of pre-existing thermal simulation models. | • Does not provide microstructure for further analysis.<br>• Requires estimation of thermal environment.<br>• Not well explored for many material system in AM. |

**Coupled models**

To this category belong the models characterized by the coupling of a fluid or mechanical analysis with the thermal one. Coupled models are distinguished in coupled thermo-fluid flow and coupled thermomechanical models.

*Termo-fluid flow models (**single-track models**)*

Generally, in these models a FEM solver is coupled to carry out the thermal analysis, and a CFD solver, generally based on the use of finite volumes (VF) or in other cases FD or FE. As already mentioned, in coupled thermo-fluid flow models the level of detail of the simulation of the EBM process is expanded, taking into account the thermo-fluid-dynamic dissipations, therefore the influence of molten material convection inside the molten pool.

In literature the development of thermo-fluid flow models is mainly due to the work conducted by M. Jamshidinia, F. Kong and R. Kovacevic. The first model [60, 61] was developed and subsequently validated considering Ti-6Al-4V. Some simplifying hypotheses have been carried out, in particular it has been assumed that the maximum temperature reached in the melt pool is lower than that of evaporation of the material, therefore the material loss by evaporation is negligible, moreover powder bed shrinkage caused by sintering is neglected. Together with the equations that govern heat exchange, the viscosity forces and thus Marangoni convection flows inside the melt pool are taken into account by introducing additional boundary equations in order to ensure the balance between the shear force and the surface tension on the top surface of the molten pool [13]. A CFD solver was used for the thermal fluid flow analysis. As regards as material assumptions are concerned, the thermal conductivity, specific heat and density were calculated as a function of solid material properties and powder bed porosity, in particular the powder bed conductivity was considered affected by its porosity and packing according to N. K. Tolochko's study [52] and was obtained from a nonlinear regression. The heat source was modelled according to the model proposed by M. F. Zäh and S. Lutzmann [49]. Finally, a comparison was made between the model in question and a thermal purification model to investigate the effects of flow convection on the temperature field and on the melt pool geometry:

the results, showed in Fig. 25, underline a narrower width, a shorter length, a deeper penetration and a higher maximum temperature compared to the pure thermal model due to the convection inside the molten pool .

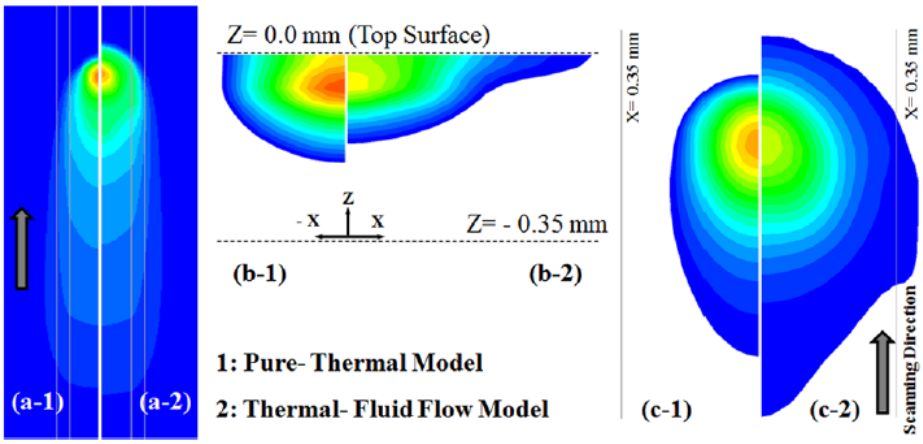


***Fig. 25*** *Effect of flow convection on temperature field an on the melt pool geometry.*

*Thermomechanical models*

The most common approaches for the realization of thermomechanical models are based on the use of two FE solvers or a FE solver and a CFD solver to perform the thermomechanical analysis to simulate the residual stresses in the EBM process.

- ***Single-track models***

  M. Jamshidinia et al. [62] have modified the previous model [60] by inserting a thermomechanical analysis to investigate on the effects of the thermal stresses caused by non-uniform heat distribution, thus a coupled CFD-FEM model was developed.

  Vastola et al. [63] developed a thermomechanical model starting from their previous model and have validated it for Ti64AlV. The model was used to investigate the effect of beam size, beam power density, scan speed and bed preheating temperature in the the stress field. The control of so called “heat affected zone” (HAZ) i.e. the region in depth and width of high stress surrounding the scan track can be achieved by choosing the appropriate

beam size and beam power density, moreover a deeper HAZ resulted from lower scan speed, and the preheating temperature influences significantly the residual stresses, with lower stresses recorded at higher bed temperatures.

- ***Single-layer models***

  Recently, a thermomechanical model has been developed by Galati et al. [64], which considers non-linearities caused by the change in material properties during melting phase. This represents an analysis of the EBM process different from that developed by the predecessors, who considered only the thermal stresses and distortions caused during the cooling phase [64]. The model takes into account the thermal expansion of the powder bed and the reduction of porosity up to the melting point and shrinkage during the cooling phase. The model has produced remarkable results in the prediction of distortion, melt pool size, residual stress, and thermal field with minimal variations compared to experimental specimens.

  The model has been experimentally validated for Ti6Al4V considering continuous scanning strategies and MultiBeam™. Furthermore, a comparison was made with respect to the purely thermal model both from the point of view of the results of the analysis and from the computational point of view. The calculation time in the case of a thermo-mechanical model has increased by about one order of magnitude.

  The model is presented as a single-track but can be extended to the single-layer case.

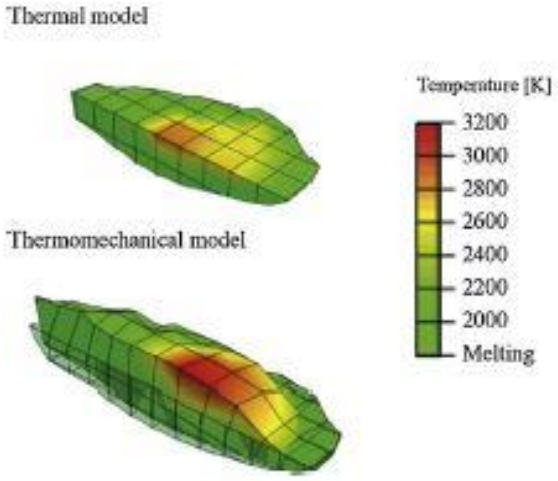


***Fig.26*** *Thermo-mechanical model developed by M. Galati et al.* [64]*, comparison with pure thermal model.*

- ***Multi-layer models***

  Based on the work [50], a coupled thermomechanical finite element model was developed N. Shen e K. Chou [65] to simulate the thermal process, thermal stress evolution, residual stress distribution and deformations in a single straight scan path and multi-layer crossed raster scan during the EBM process of Ti-6Al-4V. As regard as mechanical properties of the powder (that are considered the same as those of the bulk) are concerned the Young's modulus, thermal coefficient and yield stress were considered temperature dependent. The model allows the simulation of two successive layers using an activation technique (the second layer is activated only after the first one has been scanned). Only the top section of the substrate has been modelled. Two conditions have been developed for the simulations. In the first case a single-track simulation was conducted to investigate the thermo-mechanical phenomena for a simple condition. The mechanical results are reported in Fig. 27 which shows the trends of the longitudinal and transverse stress after the single scan.

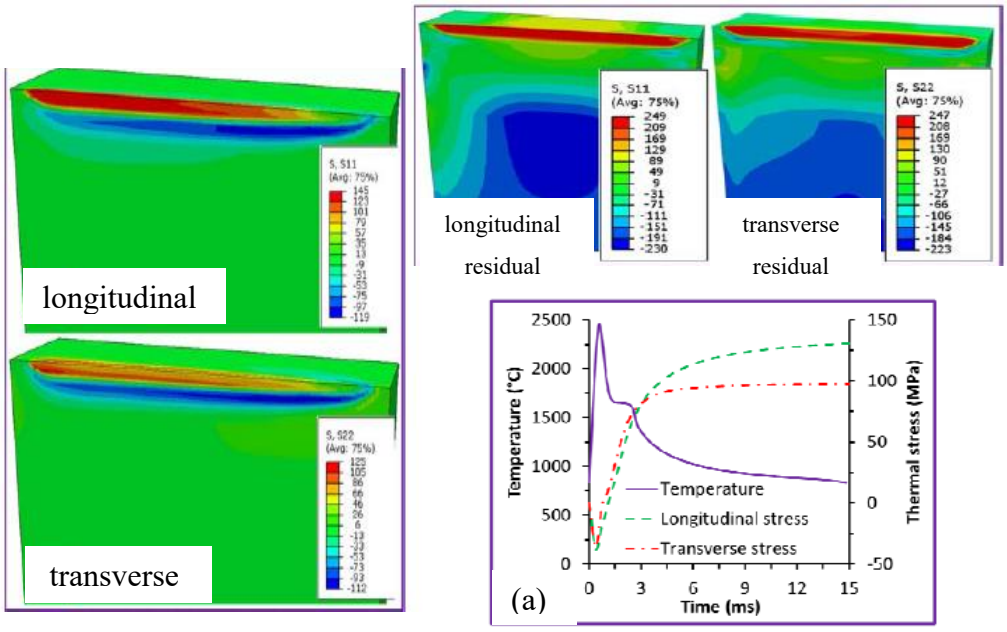


***Fig. 27*** *Results of thermo-mechanical analysis in single scan line case.*

It is therefore noted that the first reaches higher values than the latter in the second and also that the compressive stress occurs at the front of the electron beam and below the melt pool since the upper zones have been heated and expanded first. As shown in (a) when the temperatures drop there is a contraction, and there is a release of about 20-40%. The the final residual stress distributions are reported, which rise following cooling from the preheat temperature to ambient temperature (the cooling time was set at 10 hours), moreover remain residual stresses in the solidified material. In the multi-track simulation two scan lines, with an alternate raster path, on two layers were simulated. The peak temperature is about 100 ° C higher than that of the single rectilinear scan due to the residual heat of the previous trace, moreover the melt pool is longer by about 20% even if the width and depth do not vary too much and there is no plus the "tail". In Fig. 28 are reported the fields of both thermal stress components at the end of the first layer. The extent of the compression state just below the powder

drops by 50% and this stress is deeper as the heat is dissipated downwards. As before, the tensile stress lies in the upper surface layer, except for the scanning front of the beam which is in compression.

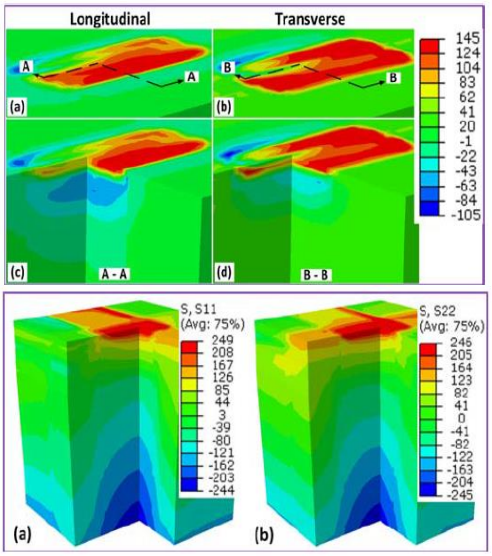


***Fig. 28*** *Results of thermo-mechanical analysis in multi scan line case.*

The magnitude of the tensile stress becomes greater due to the cooling, furthermore the area subjected to compression stress is deeper. By analysing the residual stresses, a deeper tensile zone can be observed in the substrate than in the previous case.

In the work developed by B. Cheng and K. Chou [66] the element activation was used in a 2D thermomechanical model to simulate the overhang warping during the EBM of Ti6Al4V, in particular was investigated the effect of the porosity of the powder on the residual stresses and was found that they decreased as the porosity decreased. A subsequent work [67] pointed out that the low thermal conductivity of powder, and thus a slower heat dissipation, were responsible for the higher residual stresses after the cooling.

*Computational efficiency improvement*

In the work conducted by D. Riedlbauer et al. [54, 55] the implementation of a thermomechanical model is carried out by performing a performance comparative between two possible approaches. In fact, although the adaptive refinement procedure significantly reduces the number of degrees of freedom (mesh nodes) of the problem, the thermomechanical analysis requires a high number of degrees of freedom, therefore it is necessary to reduce these DOF choosing an appropriate algorithm. The first approach consists in the use of a monolithic scheme: in these schemes both the governing differential equations are solved simultaneously with the advantage of unconditional stability but often there is the disadvantage of having large and non-symmetrical equation systems. The second approach consists in the use of a staggered scheme: in these schemes the deformation and temperature variables are solved separately, there are no disadvantages of a monolithic scheme but often they are not unconditionally stable; however on the basis of these, the adiabatic split approach was developed according to which the thermomechanical problem is divided into an elastic adiabatic phase (isentropic) followed by a heat conduction phase, thus obtaining an unconditionally stable scheme. Thus, the comparison is between the performance of the monolithic and the adiabatic approach due to problems with many degrees of freedom. Not all the phenomena of the process have been taken into consideration, such as the effect of evaporation and latent heat. The two approaches were compared on the basis of calculation time considering a linear problem and a non-linear problem. In the linear case the differences between the two approaches were less than 1%, whereas in the non-linear case the differences were more significant and highly dependent on the time step size. Although the computational results are better in the adiabatic approach, the monolithic approach is preferred for the accuracy of the solution.

### 2.4.4 Multi-scale models

To this category belong the models that combine several aspects of the EBM process belonging to different length scales. In the literature, concerning the EBM process, only a model belonging to this category is reported, the work conducted by W. Yan et al. [68] , based on the previous work [35, 36], regarding the

development of a multi-scale modelling framework to investigate and optimize EBM process of functionally graded materials (FGMs) by mixing different powder particles. The model is articulated in three scales: a heat source model derived from the micro-scale electron-material interaction simulations, a meso-scale heat transfer model to predict the thermal evolution of individual different powder particles, and a macro-scale model to simulate the temperature field and the melt pool size, as shown in Fig. 29.

Although the realization of a multi-scale model acquires particular interest for the study and optimization of the process parameters relating to the EBM of FGMs, it is important to highlight that computationally efficient manufacturing models are required for industrial production. Therefore, it is possible to conclude that to obtain this purpose the best compromise between accuracy of the results and computational cost consists in the use of a macro-scale finite element model together with a Monte Carlo micro-scale simulation for the beam-material interaction.

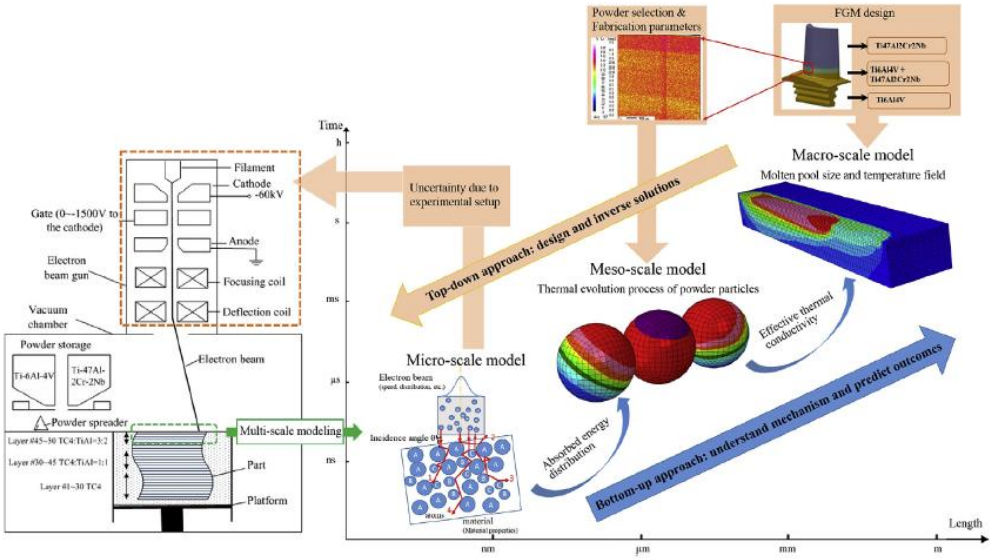


***Fig. 29*** *Multi-scale modelling framework developed by W. Yan et al.* [68].

# 2.5 48Ti-48Al-2Cr-2Nb process parameters

## 2.5.1 Titanium aluminides

The study of titanium aluminides, which has developed for 50 years [69], has aroused great interest in aerospace and automotive applications in the last 20 years [70] thanks to their mechanical properties. This family of intermetallic compounds has excellent specific properties at high temperature such as high strength, high stiffness, good creep and good corrosion and oxidation resistance thanks to their microstructural peculiarities and low density, which makes them comparable to nickel-based superalloys, which currently used as structural parts in the aeronautic field. The low ductility of these materials at ambient temperature, which hinders the conventional production and workability, have made EBM the ideal candidate for processing titanium aluminides obtaining numerous benefits both in terms of consumption and in terms of quality of the final product. However, to obtain the aforementioned benefits careful control of the process, in particular the control of chemical composition during the process is required, which significantly affects the material properties of the final product. In fact, without a special control of chemical composition and microstructure, γ-TiAl may exhibit low ductility and toughness at low and intermediate temperature [69], in particular was proved that the aluminium content significantly affects the ductility of the alloy, and the best percentage about this is around 48 at% Al [69]. Starting from this composition the material properties of the alloys have been improved by inserting suitable alloy elements. The 1$^{st}$ generation was based on a composition Ti–48Al–1V–(0.1–0.3)C which, although they had good ductility and creep resistance, they manifested poor mechanical properties, therefore a 2$^{nd}$ generation of γ-TiAl alloy was developed [69]. In particular, the Ti–48Al–2Cr–2Nb was developed by General Electric Company, which represented an excellent compromise between the material properties sought for structural applications [69], or the γ-TAB by GKSS, or Ti46.5Al-4(Cr, Nb, Ta, B) by Plansee group. A 3$^{rd}$ generation was developed to further improve the properties, based on the highly alloying with refractory

elements (5-10 at% Nb) for application at high temperature. A 4$^{th}$ generation is under development, but no official reference is available in the literature.

### 2.5.2 Generalities on Ti–48Al–2Cr–2Nb alloy

The main characteristics of the second generation Ti–48Al–2Cr–2Nb alloy, developed by GE company, will now be listed, which represents the reference γ-TiAl alloy for the validation of the model developed in this work for optimization of process parameters according to the results found in the literature obtained by the other researchers.

**Chemical composition and alloy elements**

Fig. 30 shows the range of interest for the alloy in question which has a composition between the existence field of the $Ti_3Al$ ($\alpha_2$) phase and that of the TiAl (γ) phase, shifted more towards the second phase. The choice of the alloying elements and therefore the chemical composition significantly influence the microstructure, which in turn influences the mechanical and thermal properties of the alloy. The main alloy elements are the following:

- Aluminium: (α-stabilizing) it is the main alloy element as it increases ductility at room temperature.
- Chromium: (β-stabilizing eutectoid maker) increases ductility and corrosion resistance.
- Niobium: (β-stabilizing isomorphic) improves ductility at high temperature, resistance to oxidation, and creep resistance, also induces high strengths.

It is obviously simplistic to make a generalized description since numerous factors (cooling speed, heat treatments, etc.) can significantly vary the characteristics of the final material.

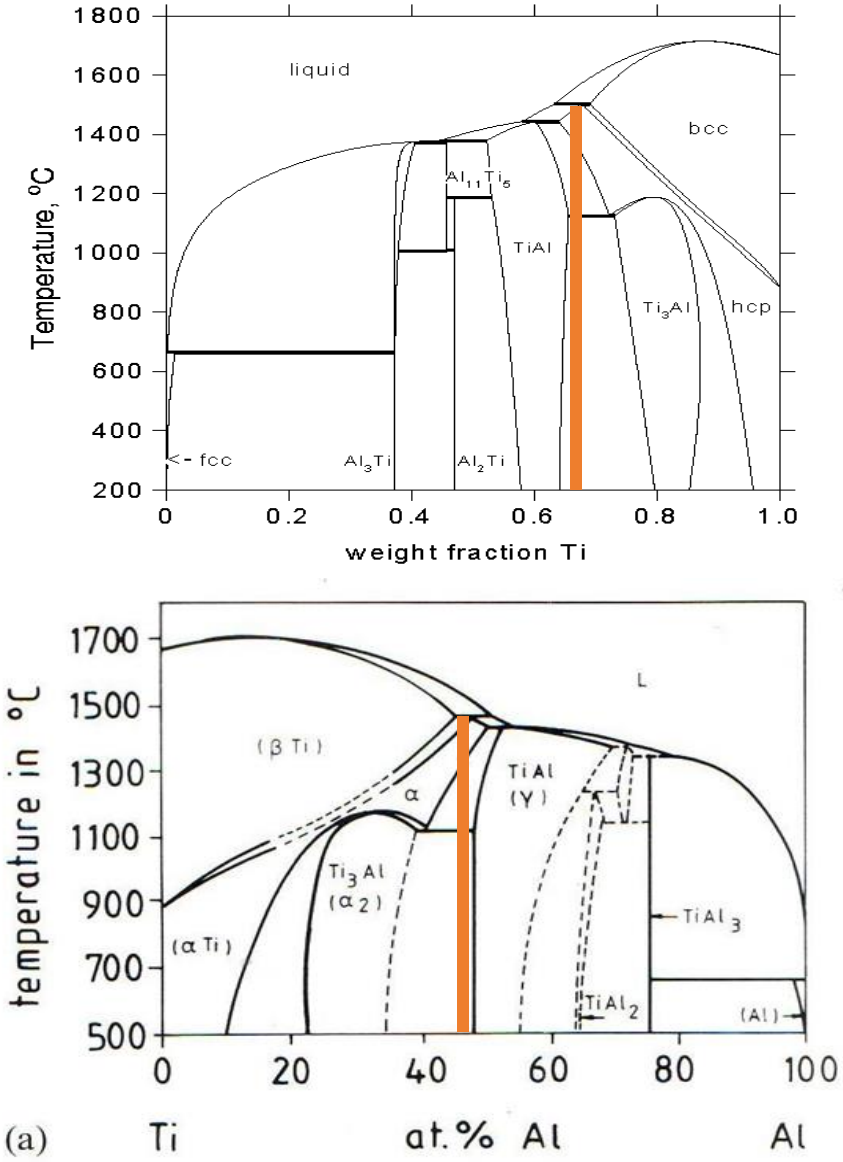


***Fig. 30*** *Ti-Al state diagram in terms of weight fraction of Ti (up) and in terms of atomic percentage of Al (down).*

**Microstructure**

As already mentioned, the control of the chemical composition is essential to obtain the desired microstructure. Depending on the temperature reached during the process and the consequent cooling, it is possible to distinguish four different types of microstructure (Fig. 31) which lead to four different results in terms of microstructure.

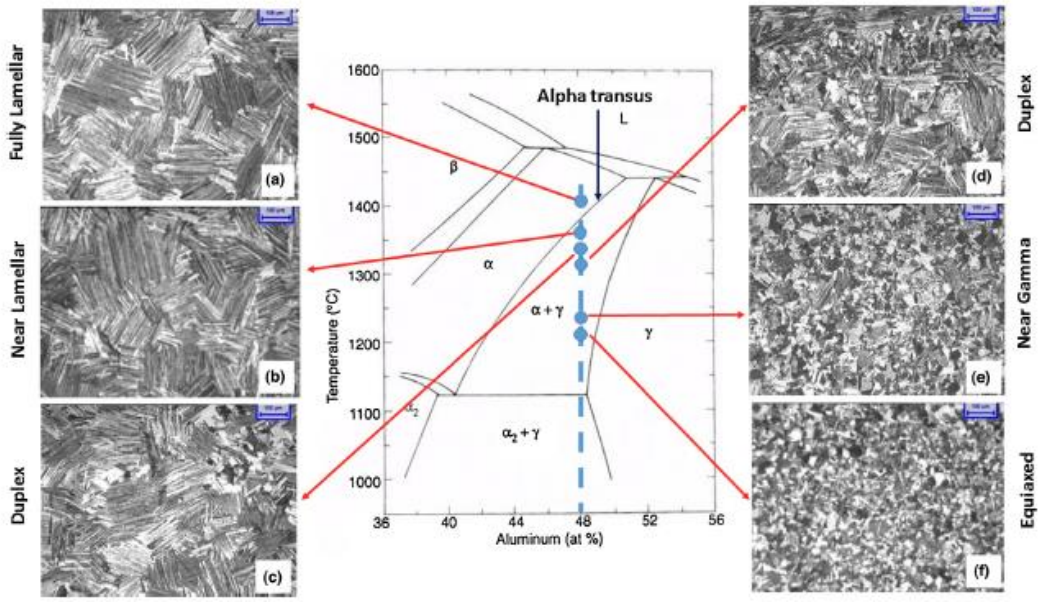


***Fig. 31*** *TiAl phase diagram with different microstructures obtained with heat treatments (blue dots) for a generical alloy with 48 at% in Al.*

- Fully lamellar: (a) fully lamellar microstructure of $\alpha_2$ e γ with coarse grains. It is very useful for temperature applications where creep resistance is important, but it has poor ductility and fracture toughness.
- Near lamellar: (b) predominantly lamellar microstructure with medium-sized equiaxial γ-grains.
- Duplex: (c) microstructure consisting of lamellar colonies with small equiaxial γ-grains. It presents high ductility, mechanical strength and good fatigue properties, it represents a good compromise between lamellar and equiaxial microstructures.
- Equiaxed: (f) microstructure completely equiaxed with high ductility and fracture toughness.

In the Ti–48Al–2Cr–2Nb alloy the ideal microstructure that guarantees a good compromise between creep resistance and good tension performance is the duplex with about 30-40% of lamellar colonies of about 100 microns in diameter, obtaining a plastic deformation of 2%. Therefore, in the working

window of interest two different crystal structures coexist with extremely different properties. In this window the solvus curve is almost vertical, therefore a small variation in composition involves a large temperature variation to obtain the same result. Ultimately it is necessary to carefully choose the process parameters in order to obtain an excellent microstructural mix and a good compromise between the properties mentioned above.

**Material properties**

- Mechanical resistance: it is generally good, comparable with that of common steels and Ni-based superalloys. This property is maintained up to about 750 ° C.
- Young's module: the high specific stiffness makes these alloys competitive with Ni-based superalloys.
- Ductility: the presence of interstitial impurities, especially oxygen, can compromise the ductility of these alloys.
- Creep resistance: the high creep resistance up to about 750 ° C is given by the presence of the lamellar microstructure. The addition of small percentages of carbon further increases creep performances as it hinders slips.
- Oxidation resistance: These alloys have a good resistance to oxidation, thanks to the presence of the phase γ, which can be further improve adding high percentage of niobium and tantalum.

### 2.5.3 Literature review on EBM process parameters

The results achieved by the researchers regarding the investigation of optimal process parameters for the Ti–48Al–2Cr–2Nb alloy via EBM process will now be presented.

The first attempt to investigate the process parameters of the Ti–48Al–2Cr–2Nb alloy is due to D. Cormier et al. [71]. In this study, 50kg of pre-alloyed powders were used to make four test bars measuring 76 mm x 25 mm x 12 mm, by the Arcam S12 system, arranged parallel on a steel start plate 120 mm x 120 mm x 15

mm heated to 900 °C. A 100 mm x 100 mm process area was considered, which was divided into the sections of the four bars, and a layer thickness of 0,1 mm. The acceleration voltage was set constant at 60kV. For preheating the entire area was scanned 50 times using a scanning speed of 8000 mm / s and a linearly increased beam current of 0.5 mA per scan, from 1 mA to 25 mA; instead each section of the bar was scanned 10 times at a speed of 2000 mm / s and at a linearly variable beam current from 15 mA to 25 mA. For the fusion a single scan was used at a speed of 100 mm / s with a current intensity of 13 mA. In this single set of parameters, a composition analysis was conducted, in particular the ICP analysis revealed an aluminium loss of 6.1wt% and 7.4at%. Furthermore, XRD analysis revealed the presence of a $\alpha_2 + \gamma$ resulting microstructure.

A subsequent work was conducted by L. E. Murr et al. [72]. In the study the Arcam A2 was used with Ti-47Al-2Cr-2Nb pre-alloyed powders with average size around 13 μm to obtain test cubes measuring 13.5 mm x 15 mm x 15 mm. The layer thickness was 0.05 mm, acceleration voltage 60kV, for preheating repeated scans have been performed at scan rate of 10000 mm/s, for the melting single scans have been performed at 100 mm/s with beam current of 10 mA. The density of the samples obtained was 3.76 $g/cm^3$ and the last layer had ridges due to beam deviations. SEM analyses revealed areas in which the powders are sintered and partially melted, therefore not very consolidated and areas where the gas deriving from the atomization process (Argon) remained trapped. The pre-alloyed powders had a prevalence of lamellar microstructure, while following the process a predominantly equiaxed microstructure is obtained, with no columnar growth along the construction direction. Analyses testify to minimal aluminium loss.

The work conducted by the Polytechnic of Turin by S. Biamino et al. [25] in collaboration with Arcam et Avio Aero companies is also reported. Although the authors did not report the process parameters used, some results have been reported, in particular an evaporation of Al less than 1wt%, and a maximum porosity of less than 200 microns. Three types of porosity have been reported: a first type of porosity, large and elongated in the direction of the scans that are attributable to the control of process parameters, a second type of small porosity and reducible by HIP treatments and a third type of small and spherical due to the

atomization process (this porosity increases as a result of heat treatments due to gas expansion).

J. Schwerdtfeger and C. Körner [73] carried out an experimental investigation on the alloy Ti-47Al-2Cr-2Nb process parameters. Ten cubes of 15 mm x 15 mm x 15 mm were made in an area of 85mm x 85mm using an Arcam A2 system with a circular steel start plate. Pre-alloyed powders of Ti-48Al-2Cr-2Nb were used. The parameters of the beam during preheating/fusion, the distance and the overlap between two adjacent passes, the layer thickness and the build temperature were considered as process parameters. The acceleration voltage was maintained constant to 60kV. A zigzag scanning path was chosen, varied by 90 ° in each layer. Build temperature and preheating parameters have been varied for each building, while in each single cube the remaining parameters have been varied. Two process parameter windows have been identified: a first window in which the layer thickness has been set to 0.1 mm (i.e. ca. 0.2 mm of powder thickness) and the scanning speed has been varied up to 600 mm/s (intermediate scan speeds), a second window in which was chosen equal to 0.07 mm with speeds up to 6000 mm/s (higher scan speed). The criterion for the evaluation of the process parameters is based on the final density obtained; also here the porosity attributable to the process was distinguished from the porosity deriving from atomization. In general, it has been observed experimentally that build temperatures in combination with more severe pre-heating parameters improve the stability of the process avoiding the so-called "smoke". For intermediate scan speeds the line offset was set up to 0,2 mm and the build temperature was chosen at 930-950°C. Fig. 32 shows that for low scanning speeds the line energy necessary to have sufficiently dense parts is higher since the dissipation of heat in the powder requires a certain minimum beam power.

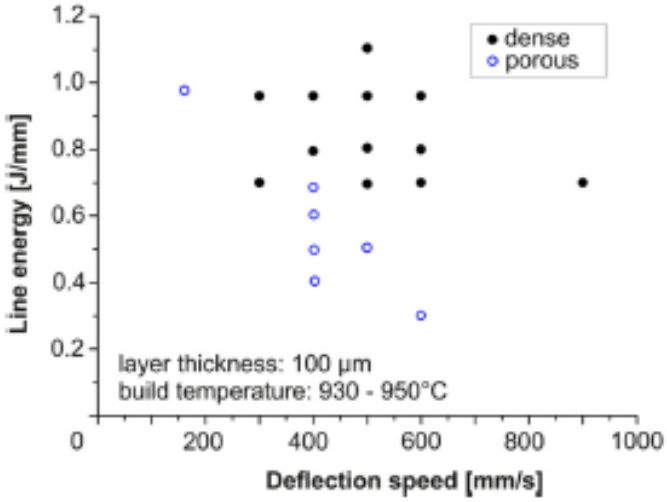


***Fig. 32*** *Process windows for intermediate scan speeds.*

As the speed increases, it is necessary to consider the "return time", i.e. the time between a point on the track and the point immediately next to the next adjacent scan line, it decreases as the beam moves towards the end of the line of scan. So, if this time is short, the heat of the previous pass has not yet dissipated, therefore it is necessary to use a lower LE to avoid overheating, evaporation surface wave phenomena. The experimental results have confirmed that the loss of aluminum depends on LE and the beam current, in particular with the same LE the amount of evaporated aluminum increases as the beam current increases. In the case of high scanning speeds, to avoid overheating, the build temperature was reduced, and the line offset was halved. The high speed has reduced the return time, therefore, the LE necessary to obtain dense parts (Fig. 33), which has been further reduced thanks to the lower line offset (the heat of the adjacent pass can be exploited) and lower layer thickness (the heat of the same pass belonging to the next layer can be exploited). In this way the loss of aluminum was further reduced, and the time required to process the layer was reduced. However, even at high speeds a minimum quantity of aluminium has evaporated, therefore it is necessary to further optimize the process parameters as more energy than necessary has been provided which has also influenced the distribution of aluminium between the various layers.

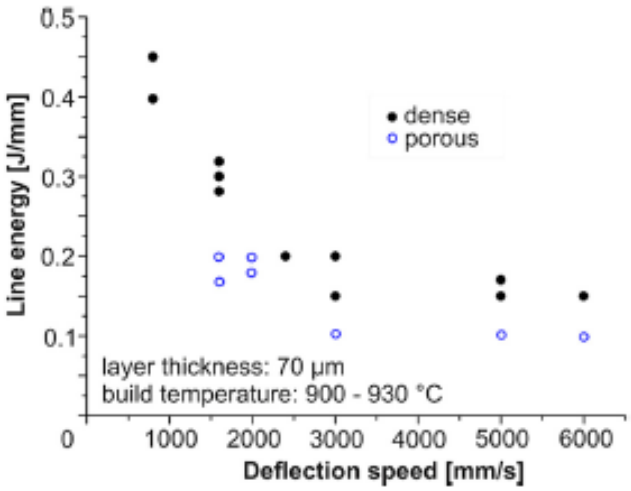


***Fig. 33*** *Process windows for higher scan speeds.*

Finally, the microstructure of the last layer processed in order to investigate the microstructural evolution in each layer was analysed. Essentially, for intermediate scan speed, the last state grows epitaxial on the substrate and presents a microstructural variation from equiaxed to columnar in the build direction. Therefore, it is understood that after the realization of the layer, this is exposed to thermal treatments induced by the successive deposited layers. For high speeds the columnar growth of the grains is not present, probably due to the different cooling conditions. Furthermore, depending on the amount of evaporated aluminium, the solidification conditions are profoundly altered in terms of the microstructure obtained.

M. Todai et al. [74] investigated the microstructure and tensile deformation properties of Ti-48Al-2Cr-2Nb alloy focusing on the development of a unique layered microstructure. The Arcam A2X machine has been used, but the process parameters used were not indicated. However, the survey carried out allows us to understand the microstructural evolution undergone by the different layers during the EBM process, as shown in Fig. 34.

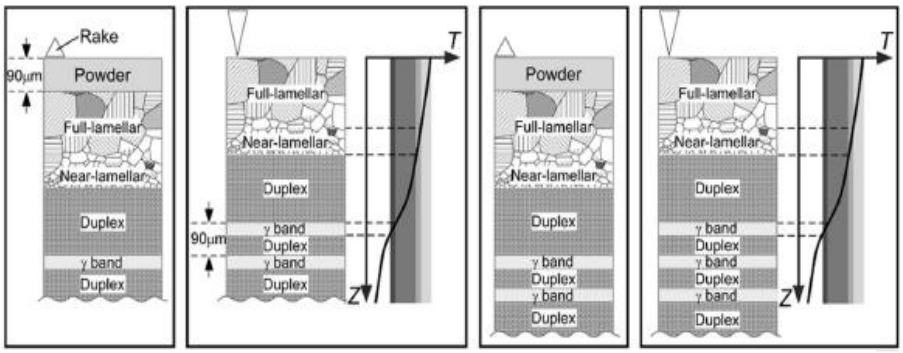


***Fig. 34*** *Evolution of microstructure during EBM process.*

Another work was conducted by J. Wang et al. [75] which used 48Ti-48Al-2Cr-2Nb pre-alloyed powders of to make a vector of nine bars ϕ15x70 vertically built with an Arcam A2 system on a steel start plate 100x100x10. The preheat temperature was set up to 1050°C with a layer thickness of 0.18 mm. For the preheating the current was set to 46 mA and the scanning speed to 12000 mm/s, instead for the fusion a current of 12-17mA was used with a speed of 1600 mm/s. The results showed an aluminium loss of 1.5% wt., A final density of 3.971±0,004 g/$m^3$, with unmelted zones attributable to the non-optimized process parameters.
In the work conducted by A. Mohammad et al. [14] was used an Arcam A2 machine to obtain, from pre-alloyed powders of Ti-48Al-2Cr-2Nb (range diameter 0,045-0,18 mm) 12x12x12 sized cubes on an inox steel start plate 100x100x10. The acceleration voltage was 60kV, the build temperature was set up to 1100°C and the scan rate was kept constant to 2200 mm/s. The area energy was considered as a process parameter, where beam current and line offset have been changed to obtain three energy levels: low, medium and high. First, the extreme values of these parameters were investigated beyond which the process was unstable, in particular the current could vary between 15-25 mA and the line offset between 0.17 and 0.35 mm. First, the extreme values of these parameters were investigated beyond which the process was unstable, in particular the current could vary between 15-25 mA and the line offset between 0.17 and 0.35 mm, after which some intermediate values (not arithmetic mean to avoid systematic errors and to investigate the non-linearity of the process). The scan orientation was alternated 90° between each layer. Experimentally it was observed that at low energies a duplex microstructure

was realized (i.e. lamellar + equiaxed), while with increasing energy the lamellar regions expanded at the expense of equiaxed, moreover the thermal cycles induced by the successive layers modified these microstructures. Furthermore, it has been shown that the accumulation of columnar grains, which grow parallel to the direction of heat extraction (i.e. mainly towards the substrate), can be avoided, therefore having fine grains, if the gradient is less than a certain critical gradient. According to work [22] a substantial loss of aluminium (around 3%) was detected in high energy case. Compared to the case of powders, where the ratio $\alpha_2/\gamma$ was around 2-2.5, in the case of samples this ratio was approximately 1.05-1.1. Finally, while at low energies numerous and large uniformly distributed porosities were detected, thus the lack of a bond, at high energies the number of pores decreased and was confined to the lower layers. This is because after making the first layers the fusion took place in a uniform way. In summary, intermediate energies allowed the realization of a duplex microstructure with pores of negligible dimensions and uniformly distributed. A subsequent work developed from the same group [26] proposed to investigate the effect of the process parameters of the Ti-48Al-2Cr-2Nb alloy on the density and surface roughness. In fact, the density levels provide an estimate of the energy introduced during the fusion, while the roughness reflects the stability of the fusion pool depending on the scanning speed used. The same powders, the same machine, and the same size of cubes were considered, in particular two builds of 25 cubes each. In this case the varied parameters are: build temperature, beam current, focus offset, line offset and speed function. The layer thickness was kept constant to 0.09 mm. For the experimental investigation a CCD (central composite design) table was used in which five aforementioned parameters were chosen. However, with this method some possible combinations of process parameters are not considered. From the experimental results it was found that speed function and line offset have significantly influenced the density, in particular for constant line offset the density increases as the line offset is reduced. As the speed function increases, the density decreases as the input energy decreases as the beam moves faster. In general, it was found that an offset of about 0.18mA and a focus offset of 5mA allow a fast construction without significant defects. The

level at which each parameter is set can qualitatively indicate the amount of energy input, as shown in Tab. 2.

***Tab. 2*** *Qualitative effect of parameter levels on input energy.*

| Input energy levels | Lower level | Higher level |
|---|---|---|
| **High input energy** | Speed function, focus offset, line offset | Beam current, surface temperature |
| **Low input energy** | Beam current, surface temperature | Speed function, focus offset, line offset |

As far as roughness is concerned, low speed and low line offset offer the best surface roughness: for low line offsets there is a low surface roughness for any value of the speed function, this behaviour is less as the line offset increases. Ultimately low speeds lead to lower surface roughness and higher density, while focus offset participates interactively with the line offset to influence density and roughness.

A recent study was developed by H. Yue et al. [76] regarding the effect of beam current on microstructure and mechanical properties of Ti-47Al-2Cr-2Nb alloy. Pre-alloyed powders from an electron induction-melting gas atomization (EIGA) were used, with distribution 0,045-0,2 mm. An Arcam A2 system has been used with three levels of beam current: 4.5 mA, 6.5 mA and 8.5 mA. A zig-zag path scan was used, rotated 90° in each layer, to make 20 x 20 x 20 sized cube samples. The preheating temperature was set up to 1100°C, the acceleration voltage to 60kV, the scan speed was set as 1800 mm/s, the layer thickness used was 0,09 mm and the line offset was 0,1 mm. Results show that by increasing the beam current in the aforementioned range, the microstructure changes from fine duplex to near gamma with doubled grain size. Moreover, the volume fraction of γ-phase decreased and $\alpha_2$ and B2 increased, this is due to the evaporation of aluminium during the process. A subsequent work of the same research group [77] was developed to investigate the effects of scan speed on microstructure, phase composition, texture evolution, porosity and tensile properties of the Ti-47Al-2Cr-2Nb alloy. Machine, powder, scanning strategy, size of samples and build

temperature remained the same as in the previous paper. The parameters used were: scan speed (v), line offset (h), layer thickness (d), beam current (I) and energy density ($E_v$), as shown in Tab. 3. The results showed that increasing scanning speed in the aforementioned range the microstructure changed from near γ to duplex and the grain size was halved.

***Tab. 3*** *Process parameters used in the study developed by H.Yue et al.* [77].

| Sample | $I$ (mA) | $v$ (mm/s) | $d$ (mm) | $h$ (mm) | $E_v$ (J/mm$^3$) |
|---|---|---|---|---|---|
| S1 | 5.5 | 1500 | 0.09 | 0.1 | 24.07 |
| S2 | 5.5 | 1800 | 0.09 | 0.1 | 20.37 |
| S3 | 5.5 | 2100 | 0.09 | 0.1 | 17.46 |
| S4 | 5.5 | 2400 | 0.09 | 0.1 | 15.27 |

By increasing the scanning speed, the $\alpha_2$ and B2 content decreased and the γ content increased, while the porosity increased due to low energy input. The high scanning speed also led to a refinement of the microstructure. A more recent study conducted by the same group [78] investigated the effect of energy density on microstructure mechanical properties. In particular, the researchers found that increasing energy density the microstructure transformed from equiaxed to elongated with a significative change in the texture.

## 2.6 Summary

The present review it is proposed to present the state of the art of the simulation regarding the EBM process. In this thesis work we tried to organize the various models according to appropriate criteria. As seen the classification of the various models is quite articulated and complex and is subject to continuous updates since the computational resources are constantly evolving.

All the models presented were able to simulate the EBM process focusing on some aspects considered important. We have seen how most simulation models belong

to the grey-box category. These represent a natural compromise between the needs previously discussed and sought in a simulation model. It has been seen that depending on the modelled aspects of the process it is further possible to have micro-scale, meso-scale and macro-scale models. Therefore, in the perspective of considering aspects of different scales it is advisable to use a multi-scale model which allows a better representation of the EBM process. As already mentioned, since the time factor is important in the industrial field, the macroscopic aspect is the one to pay the most attention to, then the development of the model discussed in this thesis is about a macro-scale model in order to obtain results in times compatible with those required in the workplace.

Finally, an overview of the 48Ti-48Al-2Cr-2Nb alloy was presented, highlighting the main potential and applicability within the additive manufacturing world.

Finally, the main process parameters used by the researchers regarding the optimization of the EBM process were presented. The various researchers, as seen, use different parameters to describe the amount of energy supplied to the powder layer during the process. It is therefore essential to identify the correct process parameters to obtain the best results.

# 3 Generalities on element activation

## 3.1 A powerful tool to improve runtime

The element progressive activation it is the heart of the work conducted in this thesis. As we will see in the following chapter, similar devices have already been used in different additive manufacturing techniques and in the welding field as well. However so far no one has applied the activation of the elements to the additive process in question, therefore this work aims to lay the groundwork for future work in terms of improving computational efficiency of the EBM process. The activation of the elements, although so far has been applied in a restricted class of applications in the future will probably involve more areas of simulation, especially the non-linear thermal-mechanical phenomena. Over the years various strategies for the progressive activation of the elements have been implemented, some of which involved the creation of numerical errors during the simulation, therefore they deserved some attention and a good knowledge of the phenomenon to be simulated. Despite some defects this feature allows to considerably reduce the calculation time in order to make the simulation model more efficient. In this sense it is possible to use finer meshes, thus obtaining more precise results, especially in areas where there is a noticeable variation in the quantity considered.

In additive manufacturing techniques, as well as in welding, many layers of material are progressively deposited to build the part, and this introduces a certain computational cost [79] that must be appropriately lowered by numerical expedients.

In the following paragraph the main uses in the literature of the element activation will be presented, providing a historical excursus.

## 3.2 Use of the element activation in literature

Over the years, many researchers have equipped their models with numerical techniques based on the activation of the elements of a mesh. Although the result in a certain sense is the same, these techniques present different approaches both in terms of managing the properties of the material and the dependence of the "switch" on some parameters. A first study of these techniques was conducted by P. Michaleris [79], which essentially identified two methods with which the material could be deposited.

The first is the "quite element approach" where the elements are presented from the start of the analysis, but their assigned properties do not affect it because each property of the material is appropriately scaled according to a scale factor. In this sense, if we consider a purely thermal analysis, the thermal conductivity and the specific heat are reduced to low values so as not to allow thermal transfer. According to the author, this approach has some advantages, such as ease of implementation, especially in commercial software using subroutines. Moreover, since the number of elements is constant, no further equations are required, neither renumbering, nor initialization of the solver. The disadvantages of this approach arise when using a scale factor that is too low or not low enough, and this can lead to numeric errors or ill-conditioning problems.

The second is the “inactive element approach” in which inactive elements are not included in the analysis until their status has become active. This entails some advantages such as the absence of numerical errors or ill-conditioning problems that occurred in the previous method. Moreover, being considered only active

nodal degrees of freedom, the system of algebraic equations will be smaller. However, this approach cannot be easily implemented in commercial software using subroutines. Furthermore, the numbering of the equations and the initialization solver must be repeated every time the elements are activated, and this reduces the advantage obtained by having smaller systems of equations. The results conducted on numerical 1D or 3D examples are identical both for the inactive and for the quiet method (using appropriate scale factors but, an artificial generation of heat occurs at the transition from inactive/quiet to active elements unless the temperature of the active/quiet elements is reset to the initial temperature during activation. However, although there was a reduction in the runtime in the early stages of the analysis thanks to the active approach, the quiet approach has been resulted more faster than the inactive one because of the continual equation renumbering and solver initialization. Fig. 35 shows a picture of the interface between active and inactive (or quite) elements.

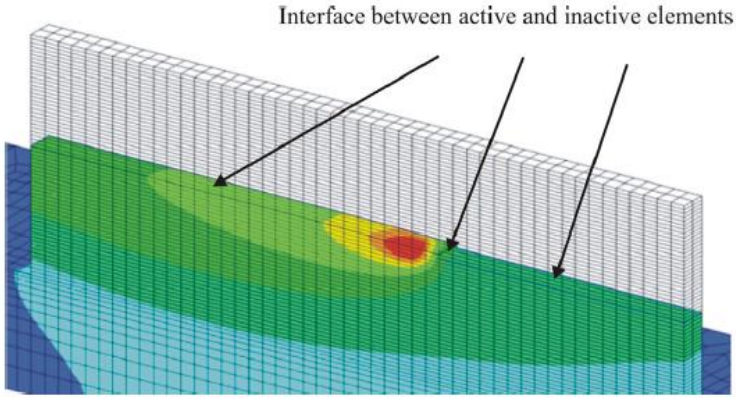


***Fig. 35*** *Interface between active and inactive (or quiet) elements.*

A hybrid model for EBAM (which is different from EBM) process has also been proposed, in which the elements are initially inactive and at each layer the elements are switched to quiet [80].

As regards the application of "inactive element approach" in the modelling of industrial processes the oldest work was conducted by Jendrzejewski et al. [81, 82] according to laser cladding, where the "birth/death" option of the ADINA code

was used. Ye et al. [83] used the "element birth method" for the modelling of LENS process. A. Lundback and L. Lindgren used the inactive quite approach in metal deposition (MD) process [84], and Zhu et al. [85] in laser direct metal deposition (LDMD) process using ANSYS as solver.

Recently a new subroutine was introduced in the ABAQUS software package, the UEPACTIVATION VOL which follows the "quiet element approach" defined by Michaleris. A more accurate description of the subroutine will be presented in the following chapters.

One of the first applications of the UEPACTIVATION VOL subroutine was carried out by M. Asadi et al. [86] in reference to the multi-pass welding process. In this case the Modelling management is entrusted to an appropriate AWI interface (Abaqus Welding Interface) and the activation of the elements was performed defining a minimum distance from the centroid of the element with respect to the centre of the torch, Fig. 36.

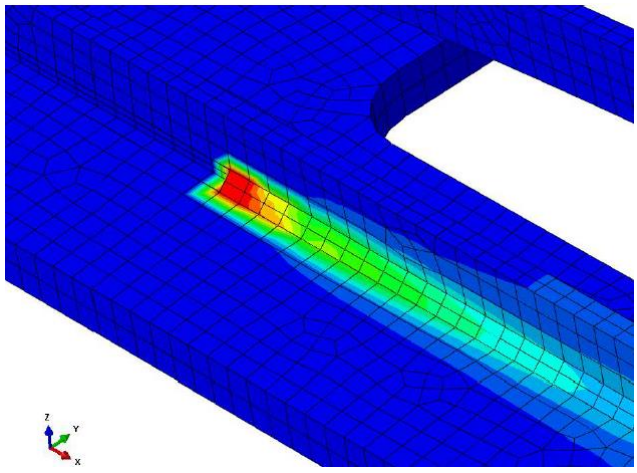

***Fig. 36*** *Temperatures of bead at activation.*

Another work in which this novel subroutine was used has led by A. Favaloro and his team [87, 88, 89] according to EDAM process (also known as Fused Deposition Modelling). The activation of the elements is conducted on the base of the temporal and spatial history of the extruder, provided to the software in the form of an event

series. In this way, by appropriately managing the information provided in the form of an event series, it is possible to process objects of any geometry by activating only the relevant elements as a real printing process.

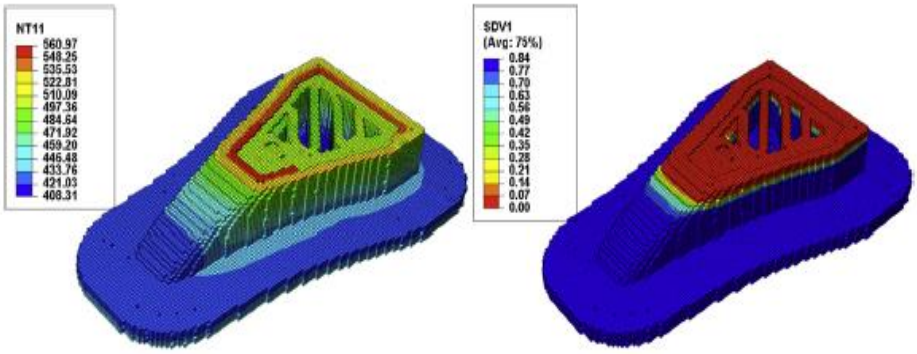


***Fig. 37*** *Illustration of a point in time during a transient printing simulation.*

A further contribute was developed by T. K. Ales [90]. In this work, according to EBAM process, the way of activation of the elements occurs according to the position of the beam as shown in Fig. 38.

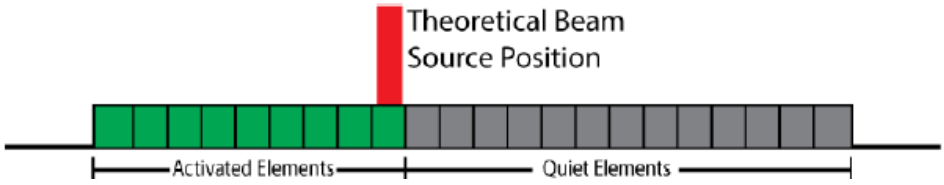


***Fig. 38*** *Activation of the elements according to T. K. Ales model.*

The study conducted by Ales shows how a sort of "barrier" is created between active and quiet elements that prevents heat transfer as shown in Fig. 39.

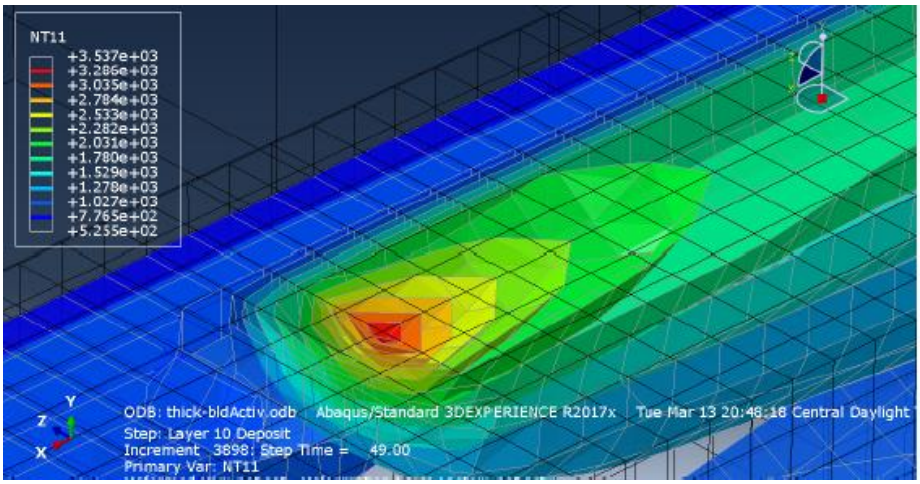


***Fig. 39*** *Nodal temperature of a simulation. The inactive elements forming a barrier ahead of the beam centre and on the side of the track.*

In this model a routine has also been developed for the management of the multilayer scanning, this management occurs according to a multistep approach. We will see in the paragraph dedicated to the implementation of the multilayer that this will be one of the possible approaches conducted in this thesis work. Each layer has a deposition and a cooling step associated with it. The step number is accessible in each subroutine of Abaqus using the KSTEP parameter. The code was created in such a way that if KSTEP is odd, then a deposition event occurs, otherwise a cooling event occurs, and the deposition head returns to the home position. The return of the deposition head to the starting position is achieved by exploiting the TIME(2) vector. TIME(1), which is the vector that provides the total simulation time, is distinguished from TIME(2) i.e. the step simulation time, which returns to zero at the end of each step.

The layer activation order is shown in Fig. 40, it is carried out from left to right. The motion control code developed by Ales is very simple and uses the division module to carry out the scanning path however as reported by the author himself this is not the most efficient method, in fact it is applied to a simple case of a thin-wall geometry with only 3 tracks. To control the layer position Ales develops a function that takes the current simulation step and returns the nearest integer associated with the number of the layer, as shown in Fig. 41.

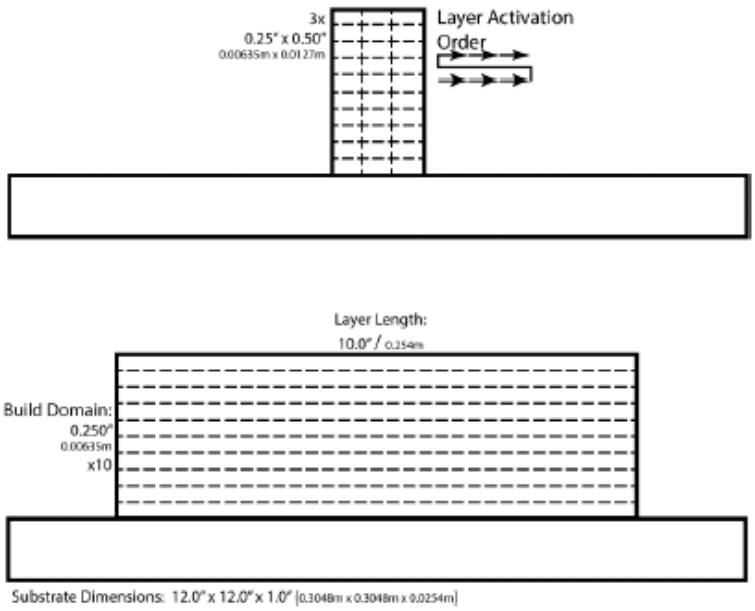


***Fig. 40*** *Thickwall build geometry and layer activation order according to T. K. Ales model.*

$$LayerNo = NINT(0.5 * REAL(KSTEP) + 0.5)$$

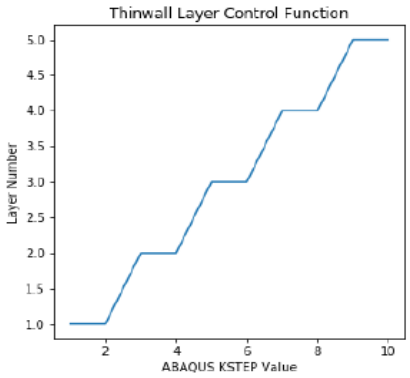


***Fig. 41*** *Plot of the function developed to provide the layer number.*

One of the most recent and interesting works is attributed to M.J. Dantin et al. [91] who have developed an open-source pre-processing framework for the DED (direct

energy deposition) process. The work seems to follow the guidelines of the work conducted by Favaloro et al. [87].

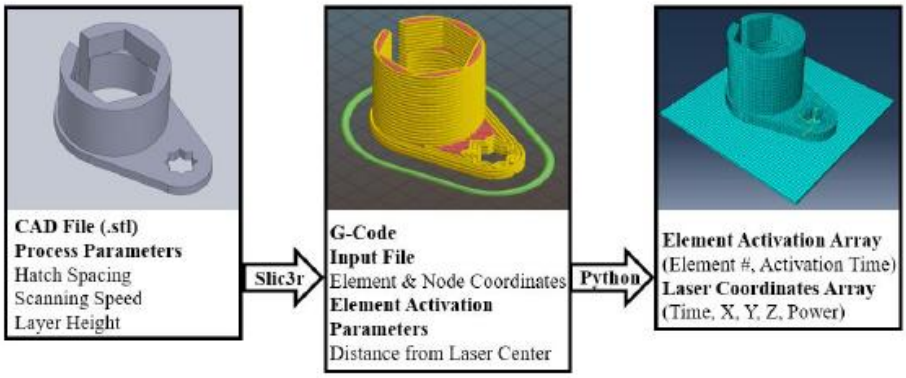


***Fig. 42*** *Pre-processing framework flowchart according to M. J. Dantin et al. pre-processing framework.*

As shown in Fig. 42, the pre-processing network can be divided into three steps. A first step in which, the component's stl file is imported into a CAM software (Slic3r) for generating the G-code. The slicer allows to set some parameters such as hatch spacing, laser power, layer height in order to obtain the deposition path. The CAD it is imported in Abaqus as well, in order to mesh it and to obtain the input file which contains some information useful for next steps, such as element numbers, nodal coordinates ecc. To avoid convergence problems the size of the mesh has been selected so that the laser travels the length of one element per timestep. The purpose of the second step is to create an array 1 which contains the centre coordinates of the laser at each timestep and another array 2 containing element number and activation time. Through a script realized in Python starting from the G-code the vector 1 is realized, moreover from the input file the vector of the centroids of the elements is created. To create the vector 2 each element centroid is compared to the centre laser coordinates at each timesteps: if the element centroid fall below the z coordinate of the top current layer and if the distance between laser centre and element centroid is less or equal than a minimum distance fig. 38 (as the same way of Favaloro approach), the element is activated.

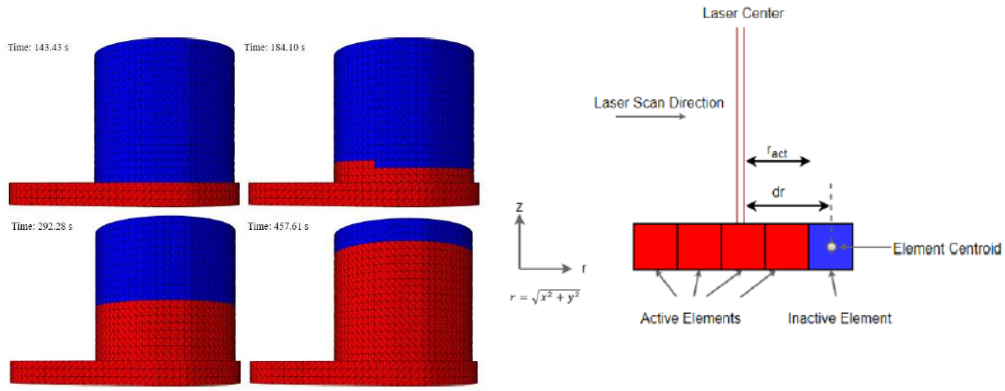


***Fig. 43*** *Element progressive activation according to M. J. Dantin et al. pre-processing framework.*

The array 1 is passed to the Abaqus input file as an event series to DFLUX subroutine, and the array 2 is passed as a parameter table to the UEPACTIVATION VOL subroutine.

In conclusion, the most recent work was made by P. Bajerski et al. [92] who have done a similar work to the one performed by M.J. Dantin according to FDM process. A flowchart is reported in Fig. 44.

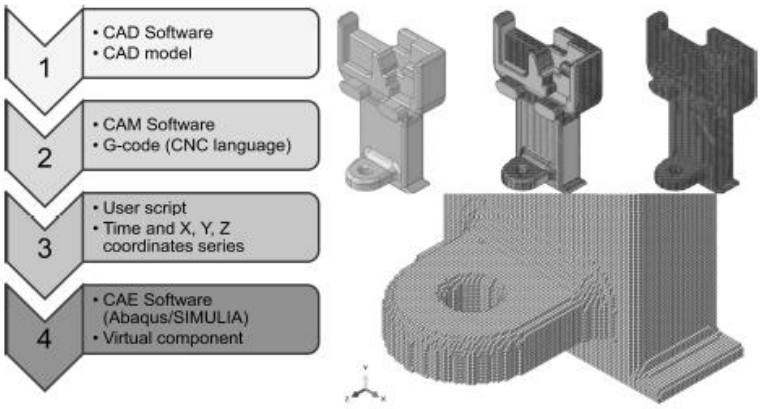


***Fig. 44*** *Virtual Additive Manufacturing according to P. Bajerski et al. work*

In literature this approach is present under the name "Virtual Additive Manufacturing".

## 3.3 Final considerations

As seen, the activation of the elements is widespread as regards the simulation of additive manufacturing processes. However, according to the particular process under examination, the elements are often activated according to the coordinates of the points of the part to be simulated extracted from slicing processes or fixed a priori. This constitutes a limitation of the simulation model and increases the number of hypotheses at its base. Therefore, no process defects or possible interruptions due to the conditions of application of the material can be simulated. This limit therefore translates into a lower reliability of the results.

# 4 Uncoupled single-layer implementation

This chapter will present the work carried out with reference to the implementation of element progressive activation according to thermal uncoupled analysis.
Criteria will be established for the progressive activation of the elements, and, based on these, a code will be created for the movement of the beam on a single layer. The activation criteria will be analyzed according to appropriate methodologies and the benefits and drawbacks of the use of one criterion with respect to another will be discussed.

## 4.1 EPA and UEPACTIVACTION VOL

Nowadays, as seen in the previous chapter, the use of the UEPACTIVATION VOL subroutine is increasingly widespread for the modelling of additive manufacturing processes. This because, as already anticipated, it allows to considerably reduce the calculation time, since there is an increase in computational cost due to the numerous tracks and layers deposited.
This subroutine, as already mentioned, uses the so-called "quite element approach" defined by Michaleris [90]. Abaqus also support the "inactive element approach" using the *MODEL CHANGE procedure, but this procedure is uneasy to use in additive manufacturing modelling as it requires that the elements to be added are previously defined and not through a condition. Furthermore, the "quite inactive" hybrid approach in Abaqus it is not possible to implement since it is not possible

to use both keywords in the same step within the input file [90]. According to the UEPACTIVACTION VOL the elements are considered at the beginning of the analysis, but they are characterized by scaled parameters as already mentioned by Michaleris.

$$c_{p,quiet} = s_{c,p} c_p$$
$$k_{quiet} = s_k k \qquad (4.3)$$

The equation 4.3 express thermal conductivity $k_{quiet}$ and specific heat $c_{p,quiet}$ of quiet elements. The size of the scale factors $s_{c,p}$ and $s_k$ is suitably chosen to obtain the best compromise between activation errors and stability of the Jacobian.

### 4.1.1 EPA feature

The Element Progressive Activation (EPA) is a recent feature of the Abaqus software package. All information provided in this paragraph about this feature was provided by the official Abaqus user guide. This feature allows to activate elements in each increment of a step. To do this it is first necessary to define the set of elements to be activated during the analysis. It is possible to specify different EPA features for each set of elements considered, so as to be able to perform multiple activations. To activate a given set of elements in a step it is necessary that the appropriate EPA feature referred to by the element set is switched on within the considered step. If the EPA feature of an appropriate set of elements is turned on it is possible to activate the elements. This activation takes place by assigning a volume fraction of material in the element at the beginning of each increment of the step considered. It is not possible to partially activate the elements so the added material volume fraction can only be zero or one. In this sense, this fraction acts as a material state variable, therefore the status of the elements can be "active" or "inactive" (i.e. quiet). By default, the EPA feature is switched off in the step.

The assignment of the volume fraction material must be done by the user subroutine UEPACTIVATION VOL which is called at the beginning of each

increment. The main parameters belonging to the interface of the UEPACTIVATION VOL subroutine that were used in the scripts created in this thesis work are reported in appendix A.1 Interface parameters.

## 4.2 Preliminary considerations according to EBM process

The steps followed for the implementation of the element progressive activation according to EBM process will now be presented. Firstly, it is necessary to specify that the realization of the codes was performed only on an uncoupled thermal heat transfer analysis. In future work it will be possible to consider adapting the code for a thermo-mechanical analysis, in fact through the user subroutine interface it is possible to access the nodal displacements of the elements so it will be possible to define an appropriate activation criterion in order to reduce calculation time. It should also be specified that initially only the activation of the elements within the single layer is considered. Subsequently, the activation of elements on multiple layers of deposition will be dealt with.

### 4.2.1 Heat source implementation

It is important to recall some considerations already discussed in the review developed by Galati et al. as they are preliminary to the implementation of an element progressive activation criterion.

The displacement of the heat source as seen is managed by the DFLUX subroutine. For the definition of the heat source the guidelines of the Galati et al. Model have been followed, in particular, the hypothesis of uniform circular distribution according to the heat input. Then a surface heat flux is applied on the surface of the layer, by defining an area (flux area) within which the flow is constant and equal to a specific value experimentally calculated. The chosen area has a circular geometry according to the equation 5.3.1 [13].

$$q = \begin{cases} \eta \frac{UI}{S} & (x_1 - x_{1c0} - \dot{x}_1 t)^2 + (x_2 - x_{2c0} - \dot{x}_2 t)^2 \leq \left(\frac{\emptyset}{2}\right)^2 \\ 0 & (x_1 - x_{1c0} - \dot{x}_1 t)^2 + (x_2 - x_{2c} - \dot{x}_2 t)^2 > \left(\frac{\emptyset}{2}\right)^2 \end{cases} \quad (5.3.1)$$

$$\text{where } \eta = \int_{\Gamma} \frac{1}{2\pi\sigma^2} exp \left\{ -\frac{(x_1 - x_{1c})^2 + (x_2 - x_{2c})^2}{2\sigma^2} \right\} d\Gamma$$

- $\boldsymbol{q}$*: heat flux* $[W/mm^2]$*;*
- $\boldsymbol{\eta}$*: correction coefficient of the global flux according to the real distribution of the electrons (with an effective diameter greater than the nominal diameter of the focus beam);*
- ***U:*** *acceleration voltage [kV] (calculated as the ratio between the incident electron energy* $E_0$ *and the elementary charge e);*
- ***I:*** *beam current [mA];*
- ***S:*** *cross section of the beam* $[mm^2]$*;*
- $\boldsymbol{\phi}$***:*** *beam diameter [mm];*
- $\boldsymbol{x_1, x_2}$: *cartesian coordinates on the XZ plane [mm];*
- $\boldsymbol{x_{1c}, x_{2c}}$: *beam center coordinates [mm];*
- $\boldsymbol{x_{1c0}, x_{2c0}}$***:*** *beam center starting coordinates [mm];*
- $\boldsymbol{\dot{x}_1, \dot{x}_2}$***:*** *scan speeds along X and Z respectively [mm].*

Through the interface of the DFLUX subroutine it is possible to access the vectors COORDS and TIME(2) which allow to easily implement the algorithm of movement of the heat source.

### 4.2.2 Terminology

In the following paragraphs, reference will be made to some terms to facilitate the comprehension.

- **Activation zone:** is the three-dimensional zone in which the UEPACTIVATION VOL subroutine assigns the unit material the fraction volume value, therefore it consists of the total set of elements activated up to a certain value of the total simulation time. Abaqus allows you to view this area by highlighting it in red, as shown in Fig. 45.

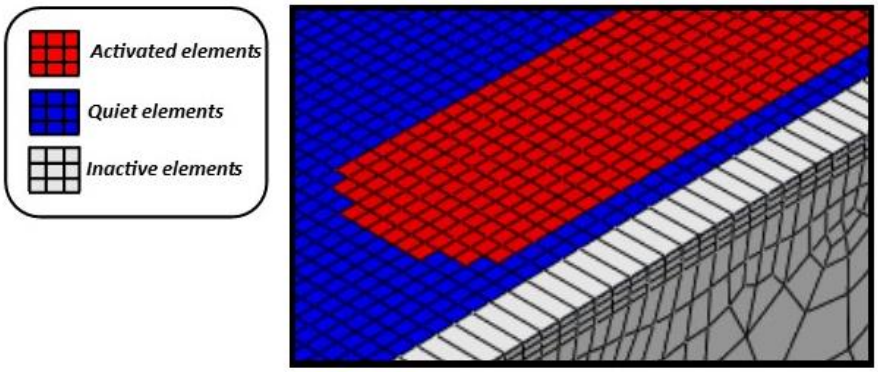


***Fig. 45*** *Activation zone.*

The inactive element in figure are not included in the EPA feature, but they belong to the overall computational load.

- **Activation front:** represents the initial portion of the activation zone;
- **Flux area:** represents the surface in which the heat flow is applied using the DFLUX subroutine. The radius of the flux area is $r_b$ (beam radius) which represents the radius of the electron beam during the melting phase.
- **True area**: Since the application of the flow occurs on a solid meshed it is important that, when defining the radius of the flux area, there is an integer number of elements on the flux area. Thus, we define a radius $R_{true}$ greater than $r_b$, as shown in Fig. 46.

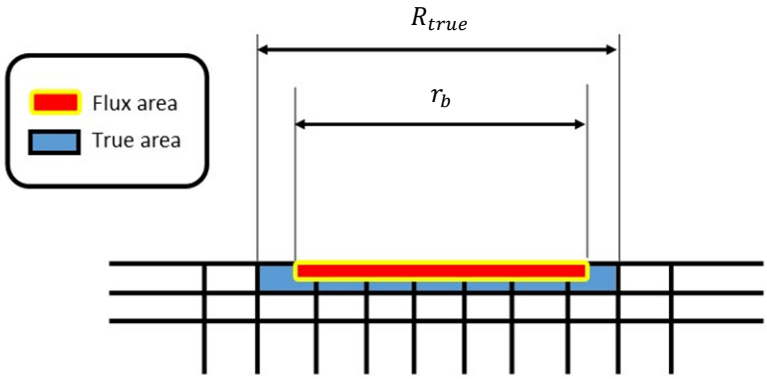


***Fig. 46*** *True area and Flux area.*

## 4.3 Element progressive activation criteria

The first step in implementing the code that allows the progressive assignment of the volume fraction material to the elements is to establish an appropriate criterion to do that. For the EBM process three possible criteria for the activation of the elements have been developed with reference to the EBM process.

We will see that not all the criteria for activating the elements are representative of the EBM process, but it is appropriate to present them all to understand their limits.

As already anticipated in the introductory paragraph relating to the description of the EPA feature and to the user subroutine, it is only possible to switch-on the elements, therefore once activated they cannot be deactivated for the whole duration of the simulation. This in a sense represents a limitation of the EPA feature as the switch-off of the elements is not allowed.

## 4.4 Targets

Each criterion at each time increment allows the activation of a different number of elements. Obviously on one hand the lower the number of activated elements, the lower the runtime will be. On the other hand, a smaller number of activated

elements could lead to convergence errors since the flux area must be contained in the activation zone.

Another target to be defined is the positioning of the activation zone with respect to the flux area where the fusion pool is centered. At each time point it is advisable for the fusion pool to be contained within the activation zone. Therefore, it is necessary to activate a number of elements so that the phase transition occurs within them and the inactive elements simulate the powder.

It is also important to reduce the number of parameters that are not known because often these cannot be established a priori. This in a sense promotes the stochasticity of the model; we will see that the purely thermal activation criterion meets this requirement.

Therefore, the main target will be to obtain the best compromise among all the needs that will be presented in the following paragraphs.

## 4.5 Starting assumptions

Although this criterion is the best of the three proposed, some initial assumptions should be made.

In this thesis work an uncoupled thermal analysis will be performed, therefore the mechanical aspect is not considered. In fact, the EPA can only be used only in heat transfer or static analysis. It would be possible to decouple mechanical analysis from thermal analysis; this approach is used by many commercial softwares but not adequate to represent the EBM process as some information is lost as all deformations are due to thermal loads. Furthermore it is also specified that the substrate has not been simulated.

As already anticipated the inactive elements possess thermal properties scaled according to appropriate coefficients with respect to the properties of the bulk material. It is not possible to access these parameters to modify them, but it is necessary to use the USLFLD, GETVRM and UMATHT subroutines to assign the material properties. Future work will be devoted to implementing the activation of elements with property assignment using appropriate state variables.

As far as mesh size is concerned, this is chosen next to the powder particle size medium, thus creating a correspondence between elements and powder particles.

No boundary conditions are applied, and the analysis is carried out assuming that the powder bed is at a temperature, assigned through a predefined field, corresponding to that reached after preheating.

The heat dissipation takes place towards the substrate and the surrounding inactive elements (albeit in small part). It is therefore assumed that the entire job is thermally isolated from the external environment.

## 4.6 Spatial-time criterion

### 4.6.1 Starting approach

The approach followed for the first criterion of element activation is similar to that followed for the Modelling of the heat source. In fact, through the UEPACTIVATION VOL subroutine interface it is possible to access the vector COORDNODES of the nodal coordinates of the elements to be activated. By this vector it is possible to easily re-adapt the code developed for the DFLUX in such a way as to define a dynamic activation zone.

### 4.6.2 Activation front geometry

It is possible to choose a specific geometry of the activation front. This geometry is determined by the envelope solid chosen to make the activation zone dynamic and must be chosen appropriately according to some requirements:

- Runtime reduction;
- Promote convergence;
- Good accuracy of results.

It is important to see how some of these needs move in opposite directions. For example, to reduce runtime, the front needs to gradually activate a few elements at a time, but this can lead to convergence errors. Therefore, since there is a trade-off between some of these needs, it will be necessary to find the best compromise.

Three possible geometries of the activation front have been identified, as shown in Fig. ***47***: prismatic, semi-cylindrical, quarter of a sphere. Since the heat source is

applied on a circular surface, it is easy to understand that the geometries of the activation front that best meet the previous requirements are the last two.

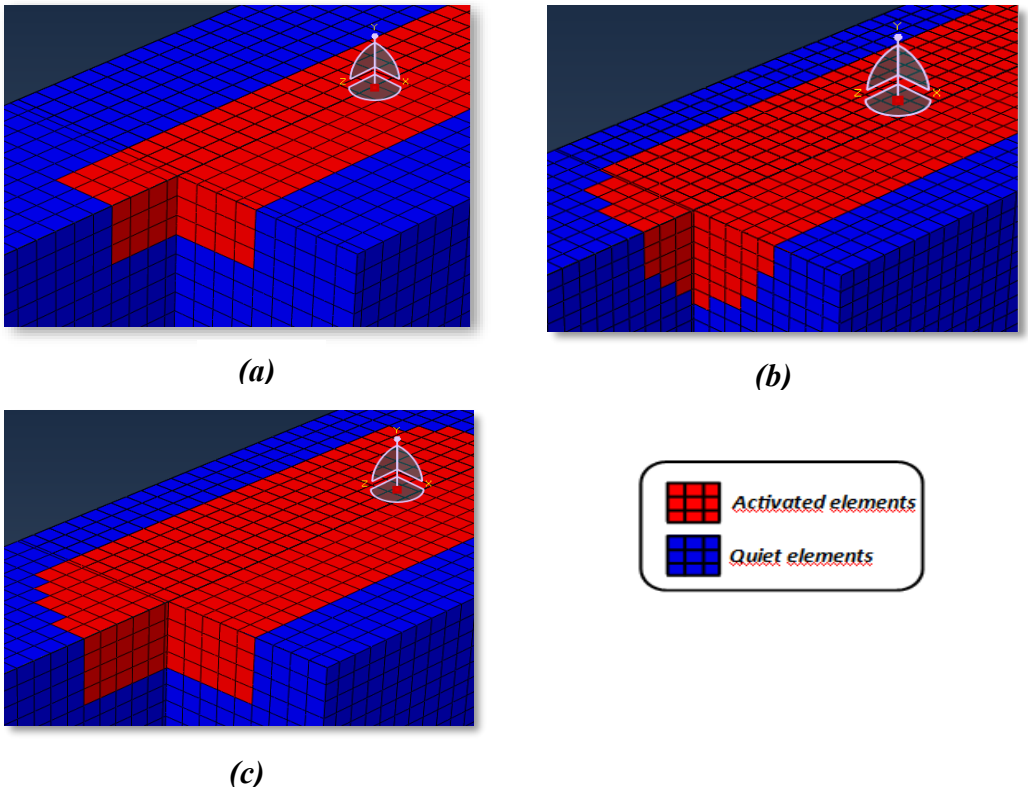


***Fig. 47*** *Different activation fronts: prismatic (a), quarter of a sphere (b), semi-cylindrical (c).*

Furthermore, the prismatic activation front leads to a distortion of the pool of fusion, given that part of the heat will be dissipated towards the edges of the prism.

Several tests on the model have shown that a quarter of a sphere front leads to greater convergence errors with respect to a semi-cylindrical front. This is because the non-linearity of the heat transfer process is right at the flux area. The quarter of a sphere front involves a smaller number of elements activated in the y direction during each time increment with respect to the semi-cylindrical activation zone, therefore there will be a greater accumulation of heat which can lead to convergence problems. This drawback could be avoided by increasing the number

of elements to be activated in the y direction, but this would be against the runtime benefits obtained by having a low number of elements to be activated during the time increment.

For the meshing, DC3D8 (heat transfer brick) elements will be used, so to be able to appreciate a good curvature of the cylindrical (or hemisphere) activation front, the size of the elements must be sufficiently low. Obviously, the size of the elements must be chosen according to the level of detail one wants to have and the computational cost one intends to accept. According to the EBM process the mesh size should be equal to that of the average size of the powder particles used.

### 4.6.3 Activation zone dimension

It is appropriate to consider two dimensional parameters, the radius of the activation front $r_a$ (in the case of prismatic activation front the activation radius is equal to half of the longer side of the front) and the height of the activation front $h$, Fig 48.

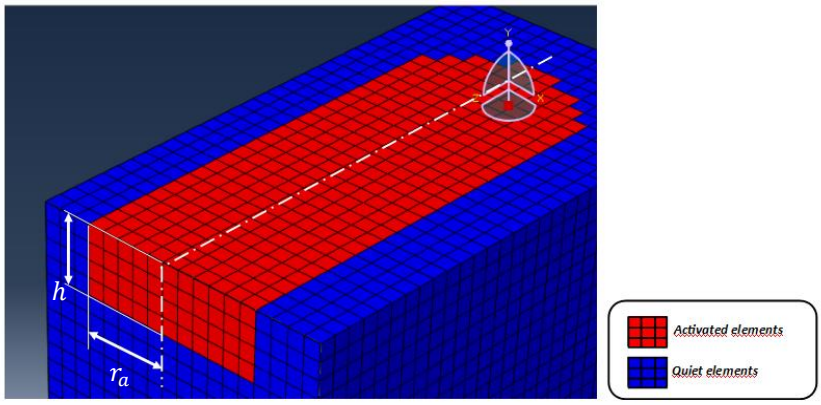


***Fig 48*** *Activation zone dimensions.*

In this way we have two dimensional degrees of freedom with which to manage the extension of the activation area. Both these parameters will have to be chosen in a suitable way to satisfy the same requirements for the activation front, a

presence of a temperature gradient on xz plane and in y direction and avoid heat build-up which result in convergence errors.
The determination of the radius of the activation front as well as the height of the activation front will be decided during the calibration phase of the model parameters. This operation is very laborious as the dimensions of the activation zone are not known a priori but depend on multiple factors such as the material and process parameters. This approach goes against the principles listed in the previous chapters regarding the correct simulation of the process.

### 4.6.4 Activation speed

The implementation of the code for the movement of the activation zone as already mentioned is similar to that for the movement of the heat source, therefore there are the same parameters, including the speed. The activation speed is assumed constant and has been chosen equal to the handling speed. Since a semi-cylindrical activation front was chosen with radius greater than the radius of the flux area, since the two speeds are equal, there will be no "barrier effect" for the heat transfer reported by T.K. Ales. Therefore, there will be a set of activated elements arranged on a greater area of the flux area and this configuration is maintained at every moment of time during movement. Obviously, one could opt for an activation speed greater than the speed of the beam but in this case, there would be a gap that would progressively increase in the scanning path. In this case the activation zone would not be optimized on the scanning path since, as anticipated, the activation zone must be coaxial with the flux area, and the set of activated elements must be contained around the melt pool.

### 4.6.5 Implementation

The implementation of the code to define the geometry of the activation front and the consequent movement along the x axis is quite intuitive. As already mentioned, we follow an approach similar to that used for the definition of the flux area through the DFLUX subroutine. **Errore. L'origine riferimento non è stata trovata.** shows a flowchart of the logic used.

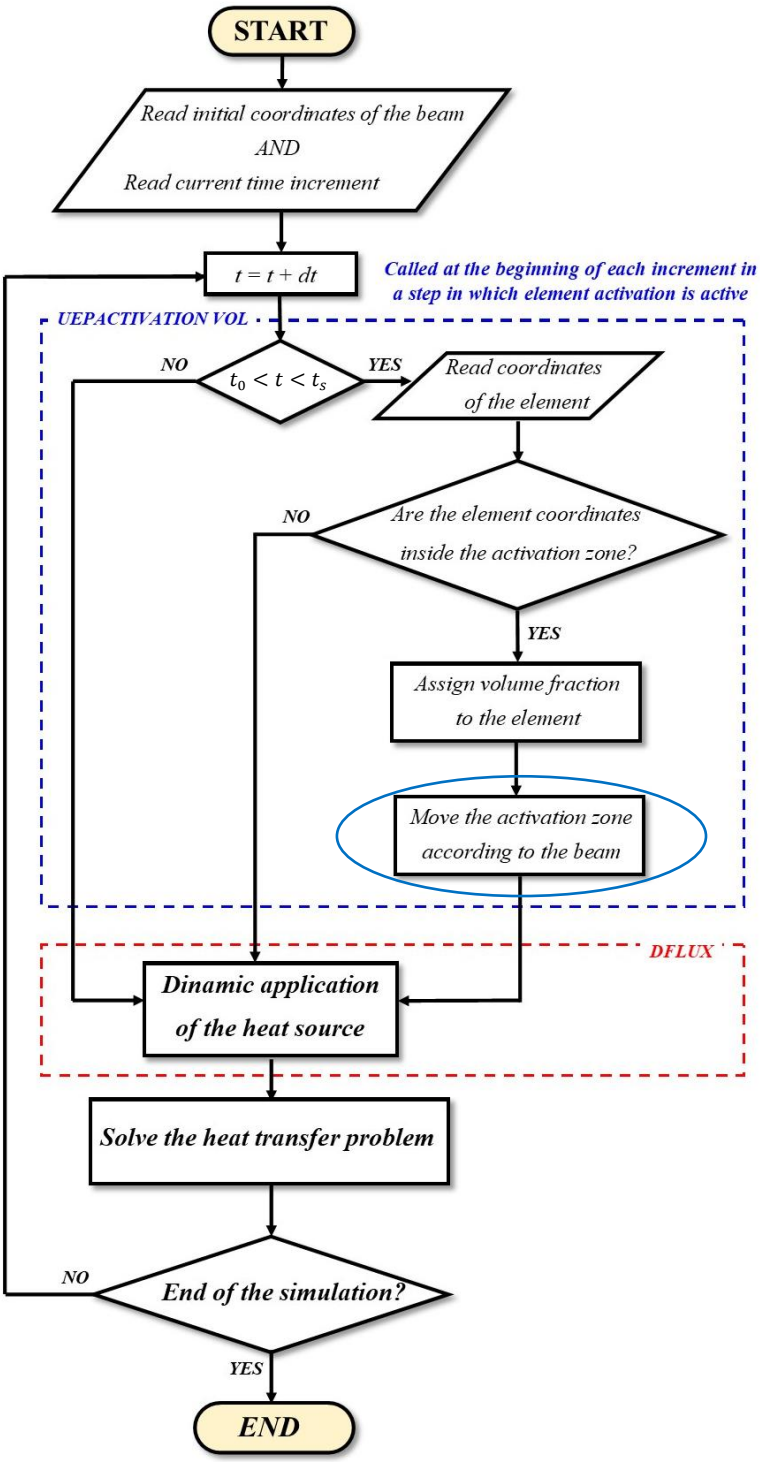


***Fig.49*** *Space-time activation criterion, flowchart.*

According to the realized code, if the time increment data is between an initial time $t_0$ and the time required to complete a scan segment $t_s$ and the coordinates of the element nodes are within the defined activation zone then the elements are activated. The activation zone geometry varies according to the type of activation front, but follows the same logic, that is the movement of the heat source. Therefore, the activation zone is moved over time regardless of the motion of the heat source (command circled in blue).

## 4.7 Hybrid thermal-time-spatial criterion

This second activation criterion is based on a more realistic approach than the previous one. It uses the spatial activation criterion already discussed as an input to carry out temperature activation.

The starting point for the development of the code is the SOL vector present in the interface of the UEPACTIVATION VOL. This vector contains the solution (temperature) at the beginning of the increment in the nodes of the element to be activated. For this reason, it is necessary to activate a set of elements following the time-spatial activation criterion in order to have a temperature field. The thermal activation is therefore realized by imposing a minimum activation temperature through a condition on the vector SOL. In this way at the beginning of one generic time increment there is already an activated zone concentric with the beam and as a function of the activation temperature the elements are activated. Thus, an activation propagation occurs, where the first activation criterion only acts as input to provide an initial temperature field.

### 4.7.1 Activation propagation

Activation propagation determines the progressive activation of the elements. However, it is necessary to check it appropriately because if the number of activated elements during each time increment is excessive, the benefits in terms of runtime reduction are lost. Fig.50 shows a comparison between the time-spatial

criterion and hybrid criterion: Both simulations were set for the same activation radius, with a snake path to facilitate the visualization of the thermal activation. It is possible to note that in the case (1) the number of activated elements is greater therefore there is a greater thermal dissipation with respect to criterion (2). In criterion (2) we can also observe a maximum temperature higher than in case (1), although the difference is minimal.

The propagation takes place not only on the xz plane but also in the y direction, so it is necessary to limit the activation of the elements along z. The height of the layer to be processed is chosen as the limit. Thus, following the application of the flow on the top surface of the layer, the activation zone will extend from this surface to a maximum depth given by the height of the layer.

The activation radius of the spatially activated set of elements must be greater than the radius of the flux area so that the entire thermal flow reaches the spatially activated elements. However, this radius must be low enough not to overestimate the melting process, since the activation zone surrounding the spatially activated elements must be able to trigger the activation propagation according to the set minimum temperature.

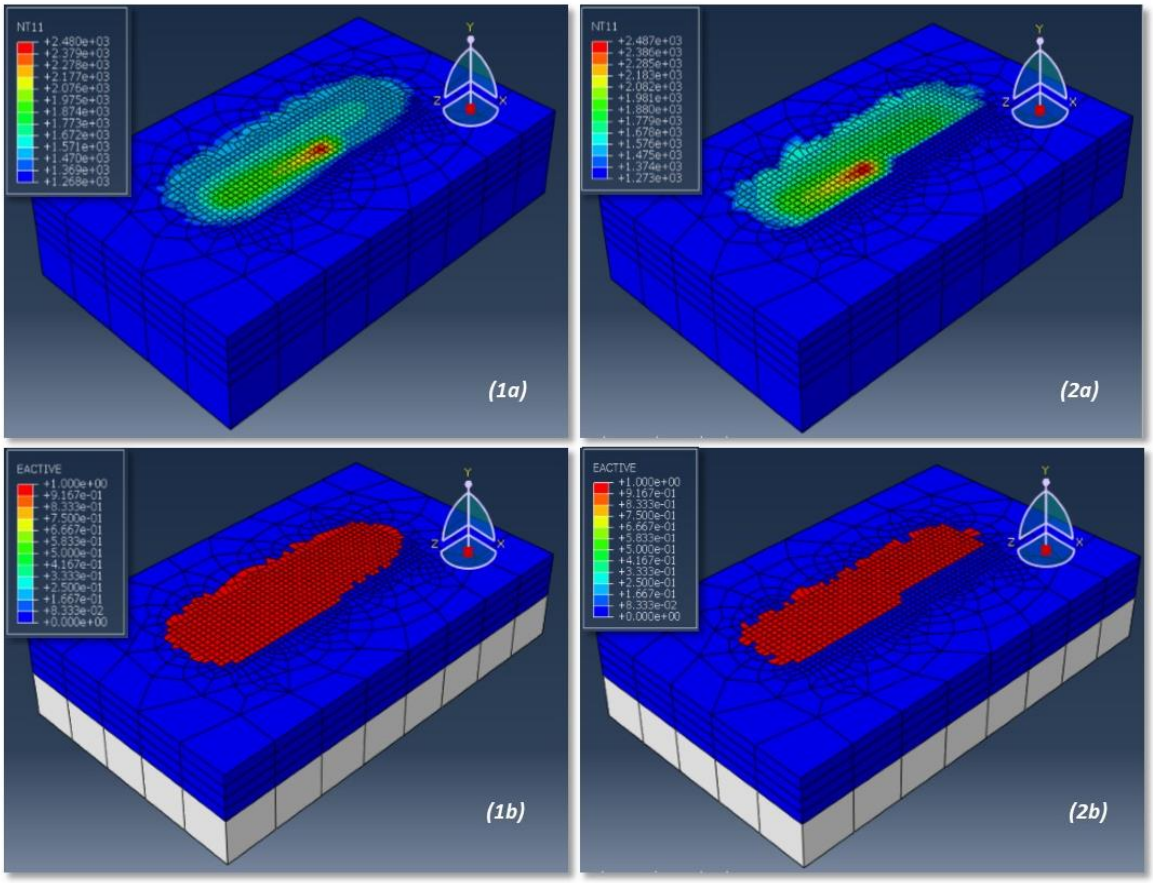


***Fig.50*** *Comparison between hybrid (1) and time-spatial (2) activation criteria: plot of elements activated (a), field temperature (b).*

### 4.7.2 Minimum activation temperature $T_{m,a}$

An important role for this second activation criterion is played by the minimum activation temperature $T_{m,a}$ since, depending on the magnitude of this temperature, a greater or lesser number of elements will be activated. If the minimum activation temperature is high, the number of activated elements will be low (only the elements close to the zone of application of the thermal flow will be active), on the other hand more elements will be activated. In particular, in the space they will

activate up to the iso-surface of the thermal field corresponding to the minimum activation temperature.

In Fig.51 some simulations are reported conducted at different values of the minimum activation temperature. As can be seen the higher the minimum activation temperature, the lower the number of activated elements, the activation zone is more reduced, and temperatures are higher. Theoretically, if a minimum activation temperature was chosen equal to the maximum temperature present in the temperature field, the activation zone would be equal to that obtained with the first activation criterion.

The minimum activation temperature must be chosen close to the solidus temperature of the material. In fact, when the powder particle reaches this temperature, the conditions for the phase transition are established. The particles that do not reach this temperature will be characterized by conductivity and specific heat different from the metal powder in phase transition. A correspondence is therefore achieved between activated elements and powder in phase transition or molten material. The set of non-activated elements, characterized by thermal properties scaled according to the appropriate coefficients, will instead correspond to the surrounding dust that hinders the heat transfer.

Since part of the set of activated elements is chosen regardless of the temperature they reach, it is necessary to calibrate the minimum activation temperature which entails a certain time in setting up the model. Ultimately, although the results of the analysis are more realistic than those obtained with the first criterion, a greater number of activation parameters is involved which make the setup of the model very expensive.

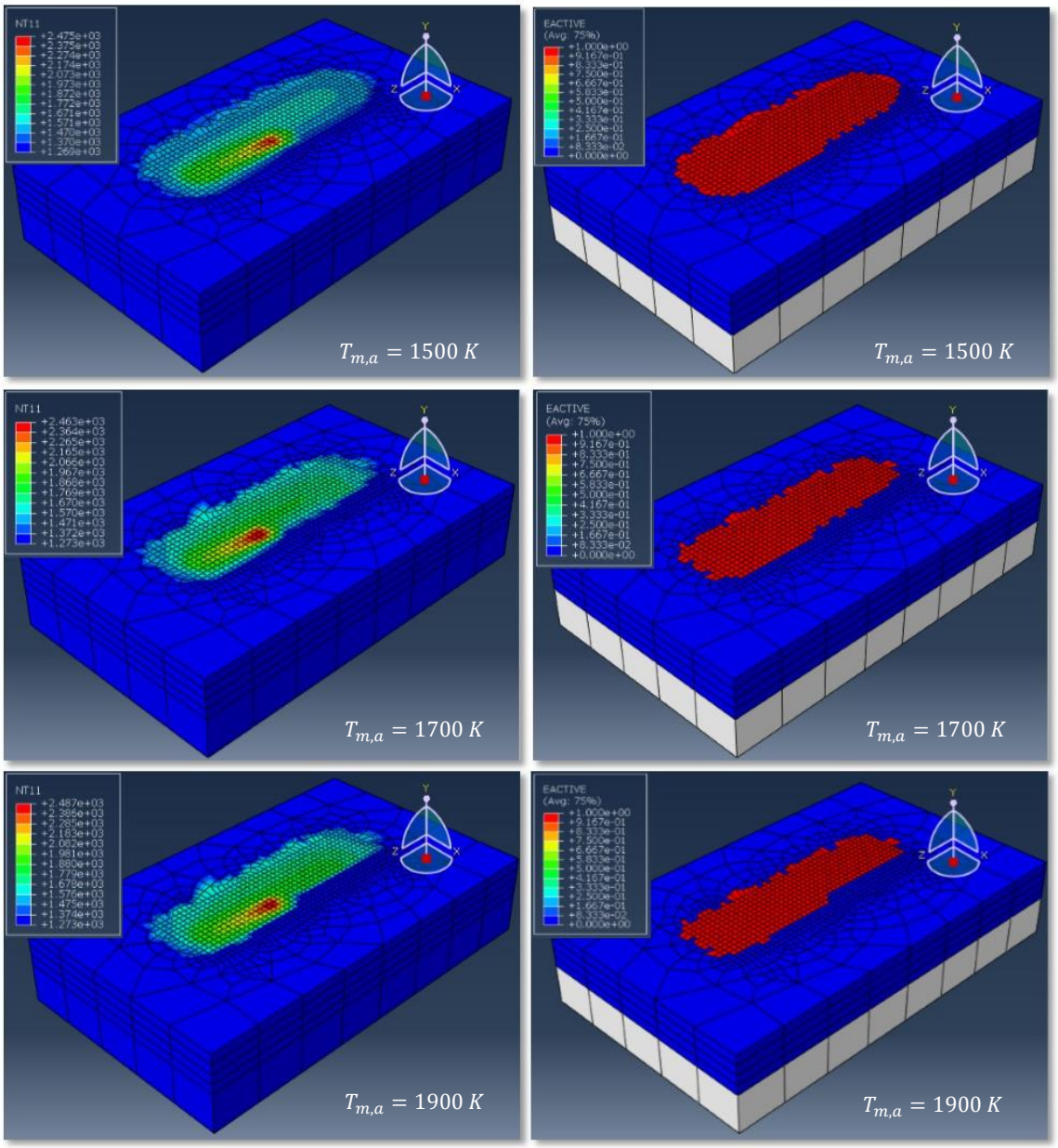


***Fig.51*** *Hybrid thermal-time-spatial: minimum activation temperature.*

### 4.7.3 Implementation

**Errore. L'origine riferimento non è stata trovata.** shows the flowchart related to the code of the activation of the elements according to the hybrid criterion.

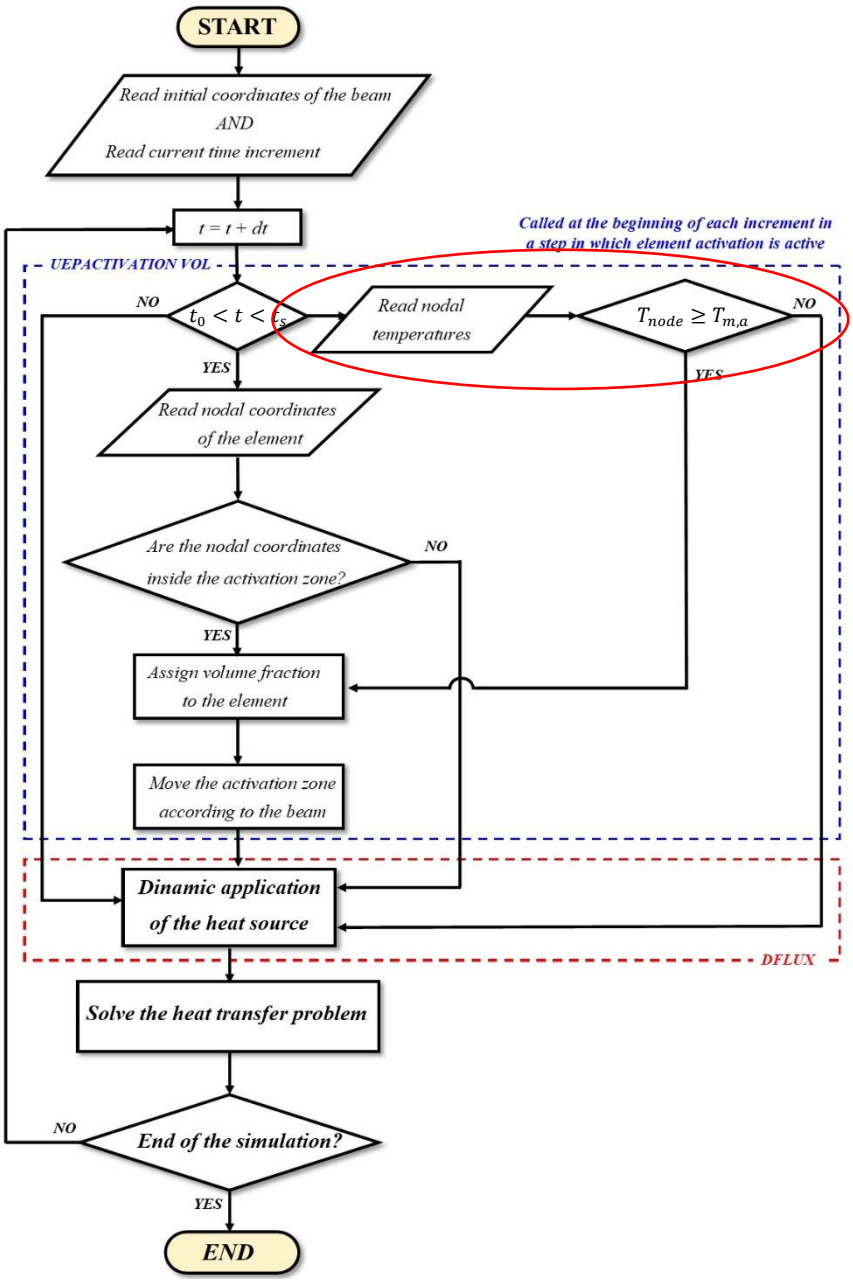


***Fig.52*** *Hybrid temperature-time-spatial criterion, flowchart.*

It can be seen that the main difference with the time-spatial criterion code is the branch circled in red. This adds an additional condition on the nodal temperature at the beginning of the increment to define the activation criterion. As time spatial criterion, the activation zone is moved independently of the heat source and the temperature condition refers to this activation zone to trigger activation propagation.

## 4.8 Pure thermal criterion

The last activation criterion involves the progressive activation of the elements purely as a function of temperature. This methodology does not exploit at each time increment a set of elements activated according to the time-spatial criterion as an input to trigger the propagation of activation but only uses an initial static activation area, of sufficient size to trigger propagation and which is present at time initial increment of the scan segment.

### 4.8.1 Initial activation zone

The initial activation zone has a cylindrical geometry, with a height equal to the layer thickness and radius equal to $R_{true}$. Since the initial activation zone is greater than the flux area, stability is guaranteed in the execution of the analysis in the first increments. In this way it will be possible to set a higher time increment lowering the runtime at the beginning of the simulation. At the initial activation zone there is a lower dimensional accuracy of the melting pool and of the temperature field since a number of elements higher than the one actually activated by the heat exchange is activated. In a single-layer (or multi-track) context, the initial activation area belongs to the first scanning segment. Since the elements cannot be deactivated, it was chosen to insert this area within the section to be processed, as shown in Fig.53. This area could not be inserted outside the area to be processed, as it possesses the properties of the bulk would allow a greater heat transfer towards it, thus compromising the temperature range and the size of the melt pool.

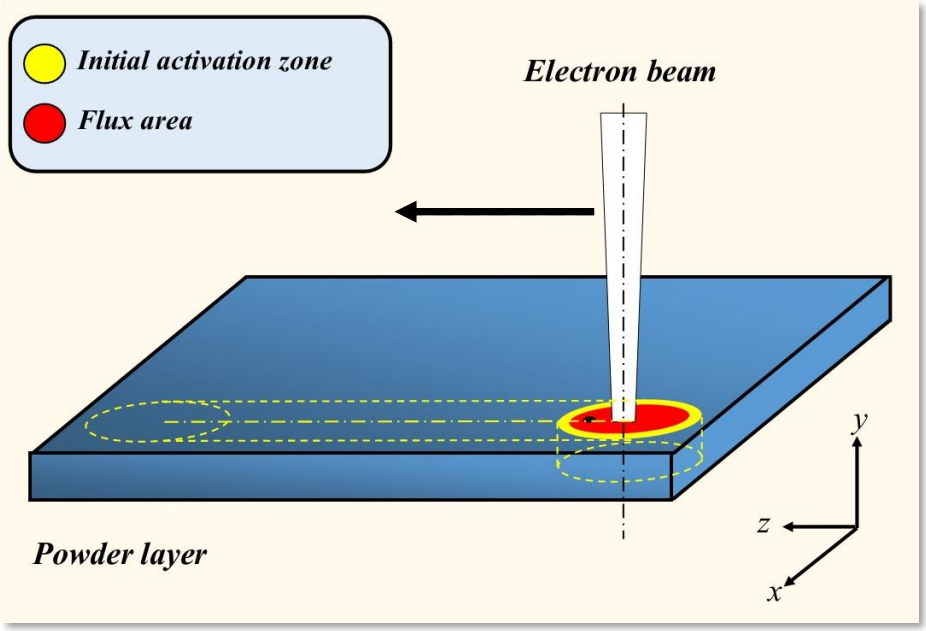


***Fig.53*** *Initial activation zone.*

The presence of the initial activation zone activated according to the time-spatial criterion results in a minimum loss of detail compared to the benefits obtained from a purely thermal activation.

### 4.8.2 Minimum activation temperature $T_{m,a}$

Compared to the hybrid criterion, the minimum activation temperature can be set equal to the solidus limit. This is not always possible, in fact often this temperature is too high to activate a sufficient number of elements to ensure a requested time increment not too low. In this case, either a very heavy time discretization parameter setup is used, which could compromise the runtime or set a minimum activation temperature lower than the solidus limit and create a status variable to exclude the elements below a certain temperature. In the latter case, the results are less accurate, but the runtime is not compromised much.

It has been said that a mesh size will be used which is approximately the same as the average size of the powder particles. However, discontinuities often arise in the activation zone, i.e. elements that do not reach the minimum activation temperature

and therefore are not activated. If the number of elements not activated in a generic time increment is such as to create a complete interruption in the scanning path then the simulation stops because at the beginning of the next time increment there is no temperature field, and the activation propagation thermal cannot be triggered. To cope with this problem, it is possible to reduce the maximum allowed time increment or lower the minimum activation temperature so as to activate a greater number of elements and thus avoid the interruption of the scanning path.

### 4.8.3 Activation front

The activation front is determined by the activation propagation triggered by the displacement of the heat source. Which has a huge advantage since the geometry of the front cannot be known a priori. However, as shown in Fig 54**,** it can be seen that the geometry of the activation front is similar to the quarter of a sphere in zx plane, but along z the activation height depends on layer thickness chosen. In fact, adding a limit on the activation depth the thermal activation propagation will be blocked by that limit.

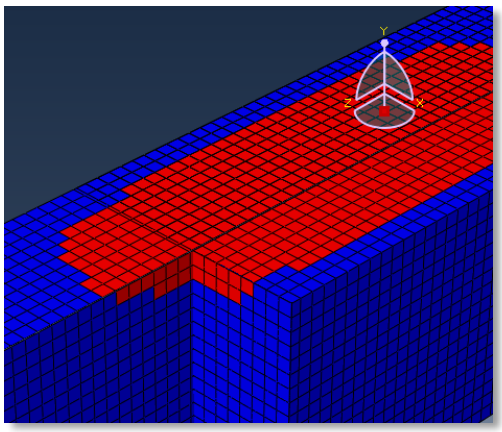

***Fig 54*** *Pure thermal criterion, activation front.*

### 4.8.4 Implementation

Unlike the first two criteria presented, in this the code uses a general time condition and within this is defined by a first condition, an initial activation zone that will be exploited to have a temperature field at the beginning of the first increment. While

thermal activation is defined by a second condition. In this case the activation of the elements according to the temperature depends on the heat source, in fact if this were true there would be no activation propagation.

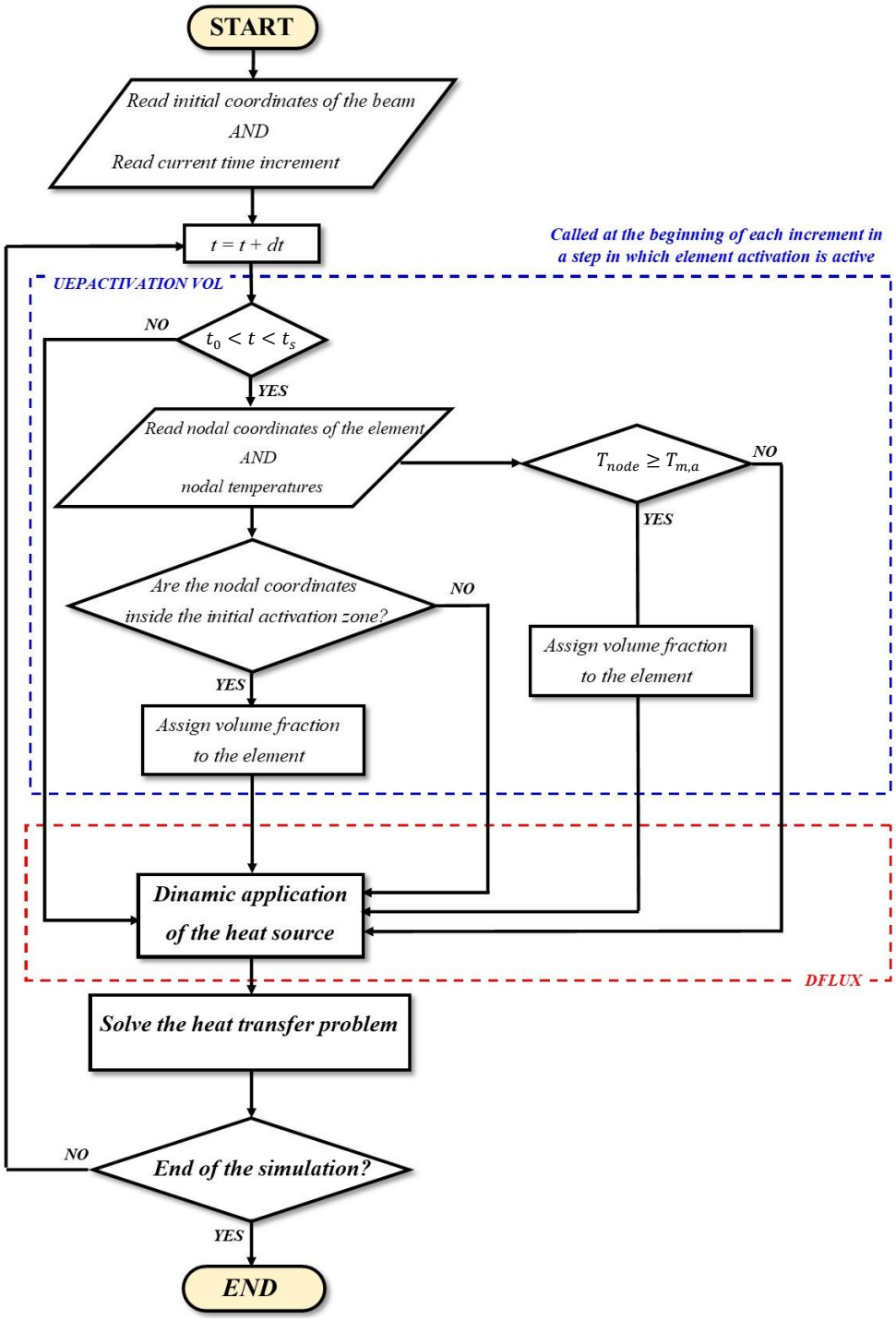


***Fig.55*** *Pure thermal criterion, flowchart.*

## 4.9 Benefits and drawbacks of the criteria

### 4.9.1 Time-spatial activation criterion

The time-spatial criterion is the least suitable to represent the EBM process since the activation zone is a priori established and not by the physics of the process, which constitutes a limit. Using this criterion would entail an onerous calibration of the activation parameters according to the process parameters and the material used, which goes against the principles listed in the first chapter regarding the realization of the simulation model. Moreover, another disadvantage of the criterion is the imposition of the activation front, which can lead to distortions of the pool of fusion.

Although this criterion is not recommended to be used for element progressive activation, it is fairly stable: there is no activation propagation which strongly depends on the time discretization increment.

### 4.9.2 Hybrid thermal-time-spatial criterion

The hybrid activation criterion is based on a more realistic approach to the simulation problem with respect to the first criterion as part of the set of elements to be activated is chosen as a function of the minimum activation temperature. However, there will always be a set of elements activated according to the time-spatial mode as it is necessary, as already mentioned, to have a temperature field at the beginning of the time increment to be able to have an activation propagation of the elements. Since there is an activation propagation that depends on the time increment this method is less stable than the previous one, however the presence of a set of parameters activated with the first criterion prevents any simulation stops due to the time increment required to perform the analysis. The setup of the activation parameters is less expensive than the first criterion.

For these reasons, although this criterion represents a fair compromise between an adequate level of detail and stability of the simulation, in order to be applied some hypotheses must be made. In fact, since a set of elements is activated regardless of the temperature reached, it should be assumed that the powder present in this set is

completely melted, therefore assuming that there are no process defects such as areas not merged or partially translated into porosity in the final part.

### 4.9.3 Pure thermal criterion

The purely thermal activation criterion defines a mode of activation of the elements exclusively as a function of temperature, thus making the computational analysis more representative of the simulated process. This criterion will constitute, as we will see in the following chapters, the basis for the development of a multilayer analysis, which will be validated by an analysis of surface roughness that is closely related to the temperature reached by the powder, therefore to the temperature reached by the elements. With this criterion it is possible to reduce the number of hypotheses on which to base the analysis and the number of activation parameters with respect to the hybrid criterion, which entails considerable advantages given that, as already mentioned, some parameters require an expensive calibration dependent on the parameters of process and material. For example, it is not necessary to choose a geometry of the activation front, but this is determined by the propagation of activation following the displacement of the heat source. The activation parameters are in fact reduced to the radius of the initial activation zone and to the minimum activation temperature. However, as already mentioned, to guarantee an adequate stability of the computational analysis it is necessary to set a minimum activation temperature that is not too high, and this must be chosen close to the solidus limit. For some materials the solidus temperature can be high so in such cases the minimum activation temperature must be chosen lower than the solidus temperature or in any case choose a configuration of the simulation parameters which is disadvantageous in terms of runtime. It must be considered, however, that the lower the minimum activation temperature is below the solidus limit, the lower the accuracy of the results in terms of the size of the melting pool and temperature, the more elements will be activated. However, it is possible to define appropriate status variables to exclude elements below a certain temperature depending on the type of analysis to be performed.

# 4.10 Single-layer motion control

A great importance is assumed by the motion control of the heat source and of the activation zone that must be coupled to the various activation criteria presented in order to be able to achieve the dynamic activation of the elements. It is important that there is synchrony between the displacement in time of the flux area and the displacement of the activation zone. In accordance with the time-spatial and hybrid criteria it is necessary to establish a motion control for the activation zone, while as regards the purely thermal criterion the movement of the activation zone is delegated to the temperature of the elements.

## 4.10.1 Heat source motion control

The movement of the heat source in a single track was carried out based on what was said in subsection 5.3.1. Based on this, the code for multi-track handling was developed, creating two different types of scanning path:

- "snaking"mode;
- parallel scan lines mode.

The snaking mode is achieved through a composition of scanning segments alternating back and forth, as shown in Fig.56.

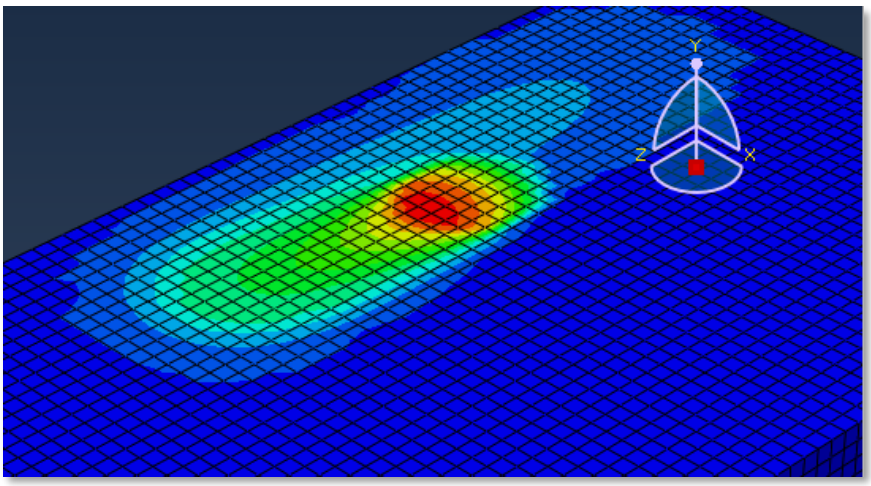


***Fig.56*** *Snaking scanning mode.*

While the second mode does not alter the direction of motion, Fig. 57.

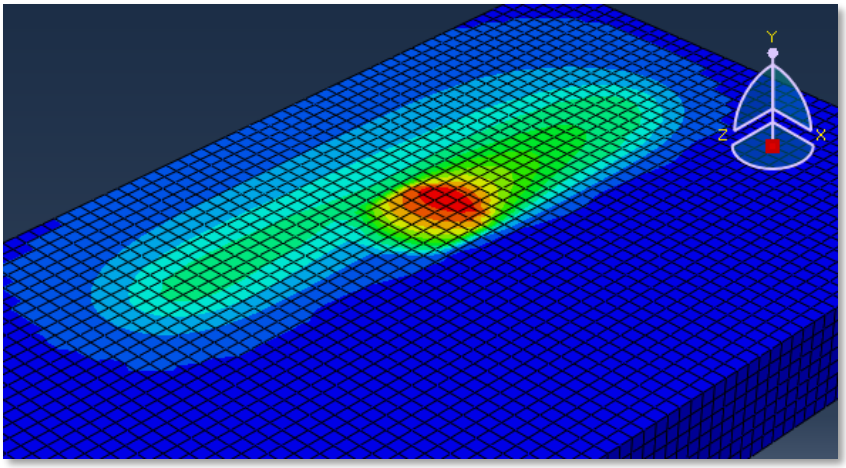


***Fig. 57*** *Parallel lines scanning mode.*

In both modes the scan segments are spaced by an amount equal to the line offset parameter, which is between zero (excluded) and $2 \cdot r_b$. In the latter case, traces are are placed side by side, for all other cases an overlap between the tracks is realized,

### 4.10.2 Activation zone motion control

According to what is said in the paragraphs dedicated to the activation criteria, it can be understood how the movement of the activation zone plays an essential role in the time-spatial criterion and in the hybrid criterion. In both cases it is necessary to synchronize this movement with that of the heat source. The speed of movement of the activation zone can be greater than or equal to that of displacement of the beam. In the first case there is a much greater number of elements activated before the application of the flow, this involves a greater heat dissipation especially in the heat application front, which involves an alteration of the shape and size of the melt pool. For this reason, it was decided to use the same speed for activation zones and heat sources.

As regards instead the criterion of purely thermal activation there is no motion of the activation zone, but it depends on heat source movement. Consider Fig.58, suppose that in a given time increment the element (a) is activated and that the element (b) is quiet. In general, the temperatures at the integration points are interpolated by the temperatures in the nodes. Since the nodal temperatures of (a) and (b) are different, Abaqus automatically generates a body heat flux in some integration points to compensate for the temperature difference [93].

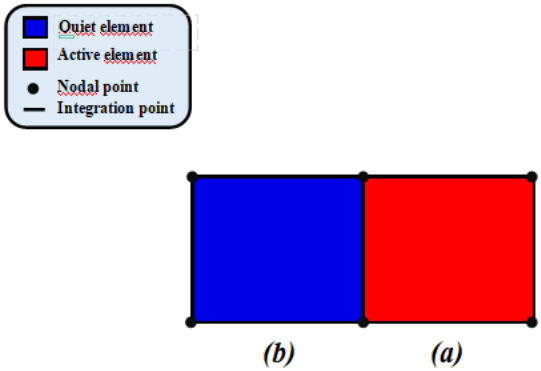


***Fig.58*** *Abaqus element activation management*

In this way, when the heat source moves, there is a heat propagation and at the beginning of the time increment there is a temperature field in the nodes of the element (b) which is therefore activated according to the activation criterion. So, the activation zone is moved according to the position of the heat source.

## 4.11 Time comparison

The main advantage for which the element progressive activation has been implemented in the uncoupled thermal analysis of the EBM process is the advantage in terms of runtime. It is interesting to make a comparison in terms of calculation time with the same process parameters, mesh size and time discretization parameters as the parameters of the activation zone vary.

The comparison was carried out single track of length equal to 1.8 mm, with the process parameters listed in **Tab. 4**. The tests were carried out on the 48Ti-48Al-2Cr-2Nb alloy whose properties are also included.

**Tab. 4** *Process parameters and material properties for runtime comparison.*

| ***Process parameters*** | ***Value*** |
|---|---|
| *Scanning speed* | *v = 2800 mm/s* |
| *Layer thickness* | *LT = 0.09 mm* |
| *Room temperature* | $T_{room} =$ *1323 K* |
| *Preheat temperature* | $T_{preheat} =$ *1323 K* |
| *Beam diameter* | *D =0.633 mm* |
| *Heat flux* | $q = 790.140 W/mm^2$ |

| ***Material properties*** | ***Value*** |
|---|---|
| *Density at 323 K* | *4.18 Kg/mm*$^3$ |
| *Solidus temperature* | $T_s$*=1737.5K* |
| *Liquidus temperature* | $T_l$*=1800K* |
| *Latent heat* | *377 KJ/kg* |

### 4.11.1 Runtime comparison with and without EPA

First, it is important to make a runtime comparison between an uncoupled thermal analysis in which the EPA was implemented and one without. To carry out this comparison, the first activation criterion was chosen which, among all the criteria, activates the least number of elements per increment necessary for the displacement of the melt pool with the same dimensions of the activation zone, thus allowing the maximum runtime savings.

Tab. 5 shows the calculation times necessary to carry out the analysis using the EPA with semi-cylindrical activation front and the calculation time in case the EPA is not used.

***Tab. 5*** *Runtime comparison between analyses with and without EPA.*

| | ***with EPA*** | ***without EPA*** |
|---|---|---|
| *Wall-clock time* | *4180 s* | *8066 s* |

Comparing the times, a clear reduction of the wall-clock time can be noticed in case the EPA is present. In fact, the presence of a large number of elements involves a greater extension of the temperature range. Therefore, the solver at each time increment will have to calculate a variation of the temperature field distributed over a greater number of elements. The number of equations to be solved in the quite element approach, as already mentioned, remains the same but the non-linearity is distributed over a greater number of nodes which increases the computational cost. Instead, if there is the EPA, this non-linearity is confined within the set of activated elements, resulting in a significant reduction in the runtime.

From the results it can be seen that the runtime required with EPA is halved. However, this is not a general rule as the runtime needed to perform an analysis depends on numerous factors such as step parameters, the number of mesh nodes, etc. In general, it can be said that the EPA has considerable benefits in terms of calculation time.

### 4.11.2 Comparison between different activation criteria

A more interesting time comparison was carried out according to the different activation criteria. A more interesting time comparison was carried out according to the different activation criteria. The process parameters and the material used are the same as shown in Tab. 4.. First of all, the purely thermal criterion was considered which, as already mentioned, activates a sufficient number of elements depending exclusively on the temperature reached by the melt pool. The width and height of the activation zone obtained according to this criterion have subsequently been measured. The same parameters were used by performing a simulation according to the time-spatial activation criterion. In this way it was possible to make a comparison with more or less the same total elements (activated at the end

of the track) in both criteria. It is expected that the best results in terms of runtime are those obtained using a quarter of a sphere geometry activation front given that for each time increment the number of activated elements is smaller than the other three geometries. In fact, if compared to the semi-cylindrical geometry we have the same elements activated on the xz plane for each increment, but in the y direction the number of elements activated by the quarter of a sphere geometry is lower. However, the smaller number of elements activated in the radial direction could lead to convergence instability, therefore the quarter of a sphere activation front does not necessarily result in lower runtime. Instead the prismatic geometry activates by time increment a number of elements, in the three directions, higher than both. The same activation height $h$ was chosen for the three activation fronts and equal to layer thickness, with activation radius equal to $R_{true}$.
Tab. 6 shows the results of the simulations.

**Tab. 6** Runtime comparison between different activation front geometries according to the time-spatial criterion.

| | ***Prismatic*** | ***Quarter of a sphere*** | ***Semi-cylindrical*** |
|---|---|---|---|
| *Wall-clock time* | *N. A.* | *4374 s* | *4180 s* |

The results in terms of runtime confirm what has been said: the semi-cylindrical activation front involves a minor runtime. In fact, we have the 3 rows of elements activated along the thick of the layer that involve a better convergence stability. While in the front quarter of a sphere there is a slight delay probably due to the few elements activated on the layer thickness at the front. The prismatic front involves a distortion of the pool which, in quite complex materials from the point of view of thermophysical properties, such as TiAl, can lead to convergence errors. The simulation stopped at 70% with a wallclock time of 3395 s.

Subsequently, the activation parameters related to the hybrid activation criterion were set up. A semi-cylindrical activation front was chosen for the hybrid criterion. A minimum activation temperature was chosen close to the solidus temperature of the material and an activation radius equal to the minimum allowed to trigger the activation propagation for the same time discretization parameters. Finally, the runtime comparison between the three different activation criteria was carried out; The results are shown in Tab. 7.

***Tab. 7*** *Runtime comparison between activation criteria.*

| | ***Spatial-time*** | ***Hybrid*** | ***Pure thermal*** |
|---|---|---|---|
| *Wall-clock time* | *4180 s* | *4438 s* | *3870 s* |

As already announced, the activation criterion that reduces the computational cost the most is the purely thermal one because it activates for each time increment a sufficient number of elements for the displacement of the melt pool with the same dimensions of the activation zone.

As regards the hybrid criterion, the temperature of 1720 K (set for the purely thermal criterion) gave some problems of convergence therefore it was lowered to 1650 K. Therefore, this entailed the activation of a greater number of elements which resulted in a greater wall-clock time with respect to the time-spatial criterion.

Ultimately, the purely thermal criterion is not only the best choice for the simulation of the EBM process but also the one that allows the lowest runtime.

### 4.11.3 Final considerations

Although the progressive activation of the elements allows a considerable reduction of the runtime, it is appropriate to make some considerations in this regard. The simulation of the EBM process on single layer, and also on multi-layer involves a computational cost that grows progressively as the number of tracks and layers processed increases. This concept is also reflected in the element progressive

activation. In fact, during the activation of the tracks the number of active elements increases, therefore the area of the analysis domain in which the solver must find the solution to the thermal problem increases. Therefore, there is a progressive increase in the computational cost as the number of processed material increase.

# 5 Single-layer verification

In this chapter we will discuss the steps taken to verify the model made by performing a single-layer thermal uncoupled analysis. The verification will be carried out by comparing it with the model developed by Galati, which has already been discussed in Chapter 3. This comparison aims to highlight the difference in the results produced by the model developed in this thesis work with reference to the Galati model, already experimentally validated. It is important to be aware of the deviation of the results from the reference model as on the basis of these deviations it will be decided whether to further improve the model on the predecessor's guidelines or to use a new approach.

## 5.1 The reference model

The work conducted by Galati et al. [13, 51, 94], was the starting point for this thesis work. The model developed belongs to the category of macro-scale models because the powder is modelled as a continuum. However, thanks to the results obtained through a micro-scale simulation, based on the Monte Carlo method, it was possible to derive appropriate considerations on the modelling of the heat source. According to the previous classification, the model can be classified as uncoupled but recently it has been improved by developing a thermomechanical analysis [64]. Although the model developed by Galati et al. has given optimal results in terms of simulation of the EBM process, the need to increase the runtime is great.

This reference model, as already mentioned, uses the so-called "material change", therefore assigns the thermophysical properties according to a logic cycle that

exploits a material state variable (MAT_ID). According to the code developed by Galati, if the material state variable is not the powder identifier (MAT_ID = 0) it will be necessary to assign the thermophysical properties of the bulk material, if instead it is that identifying the powder the discriminant is the temperature: if the temperature in the nodes it is lower than the solidus limit then it is necessary to assign the properties of the powder material, if instead it is greater than the solidus it is necessary to update the state variable (MAT_ID = 1) and assign the properties of the bulk material [13], Fig. 59. As regards the containment of the computational cost, the reference model consists of a layer in hexahedral elements with a suitable mesh refining of the central area with respect to the peripheral where there is a mesh size of 0.05 mm.

The model developed in this work as already announced does not take into account the thermophysical properties of the powder, therefore we expect a gap in the results obtained from the simulations with respect to the reference model.

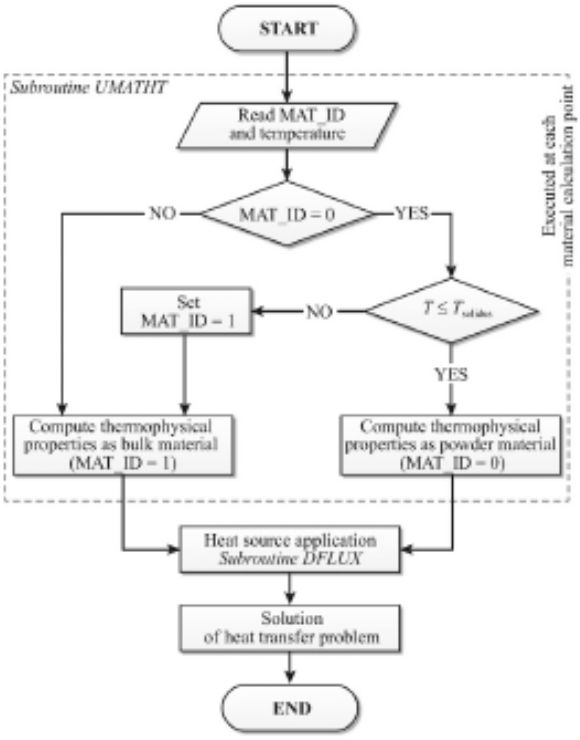


***Fig. 59*** *Flow chart of the user subroutine developed by Galati et al.* [13].

## 5.2 Methods

In this section the steps that led to a first validation of the single layer model will be presented.

### 5.2.1 Preparation of the part

The part on which the verification will be carried out is shown in Fig.60. The internal prismatic partition highlighted in green represents the layer to be processed with section 3 mm x 1.8 mm. The rest of the part represents the surrounding powder. The external dimensions are 6 mm x 2.4 mm with 1 mm of substrate below the layer to be processed for heat dissipation.

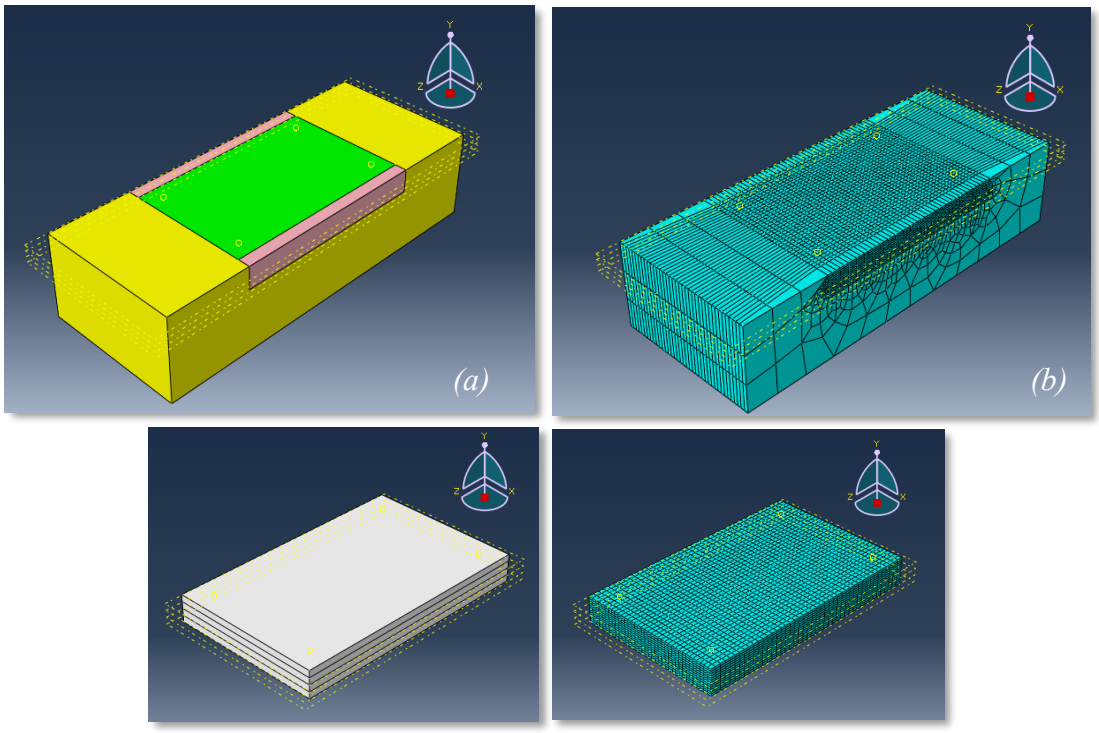


***Fig.60*** *Partition of the model (a), mesh (b). Below, the partition made on the layer set (including 0.1 mm off-set)*

A hexahedral mesh with DC3D element (heat transfer brick) was used. A refinement was performed using three different mesh sizes. The smaller size 0.03 mm was chosen along the build direction in order to have 3 rows of elements along

the layer thickness. Instead on the section of the layer a mesh size of 0.05 mm was set according to the average particle size (0.045 mm). Finally, a mesh of 0.3 mm was used for the surrounding substrate and perimeter.

### 5.2.2 Process parameters and material properties

The verification was carried out on the 48Ti-48Al-2Cr-2Nb alloy whose thermophysical properties of the bulk are listed in ***Tab. 8***. *Fig. 61* shows the conductivity and specific heat curves as a function of temperature. Process parameters listed in ***Tab. 8*** were used for the processing of the layer. The layer is obtained by 6 tracks adjacent with overlap dictated by the line offset of 0.2 mm. The scanning strategy used is the parallel scan line mode.

The analysis starts immediately after the preheating phase, which is not simulated. Therefore, the temperature of the element to be activated is assigned with a predefined field as the initial condition with a temperature ($T_{preheat}$) equal to the room temperature ($T_{room}$).

***Tab. 8*** *Process parameters and 48Ti-48Al-2Cr-2Nb material properties (bulk) for model verification.*

| ***Process parameters*** | ***Value*** |
|---|---|
| *Scanning speed* | *v = 2800mm/s* |
| *Layer thickness* | *LT = 0.09 mm* |
| *Line offset* | *LO = 0.2 mm* |
| *Room temperature* | $T_{room} =$ *1323 K* |
| *Preheat temperature* | $T_{preheat} =$ *1323 K* |
| *Beam diameter* | *D = 0.633mm* |
| *Heat flux* | $q = 790.140\ W/mm^2$ |

| ***Material properties*** | ***Value*** |
|---|---|
| *Density at 323 K* | *4.18 Kg/mm³* |
| *Solidus temperature* | $T_s$*=1737.5K* |
| *Liquidus temperature* | $T_l$*=1800K* |
| *Latent heat* | *377 KJ/kg* |

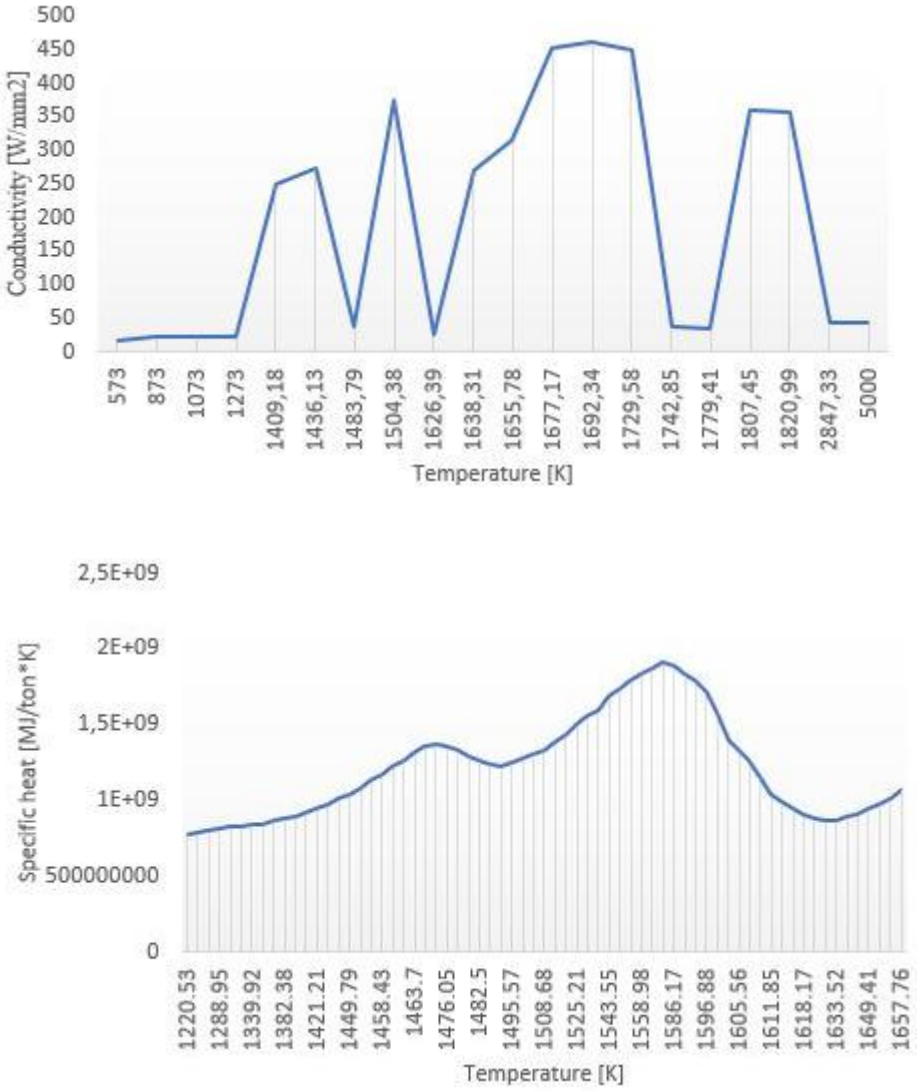


*Fig. 61 conductivity and specific heat curves as a function of temperature*

### 5.2.3 Activation zone parameters setup

As regards the setting of the activation zone parameters, a radius of the initial activation zone equal to beam radius. The activation zone is located within the section to be processed, Fig.62. Since the solidus temperature is high enough and the element progressive activation involved interruptions to the track, it was

decided to lower the minimum activation temperature, with respect to the solidus limit, to 1700 K.

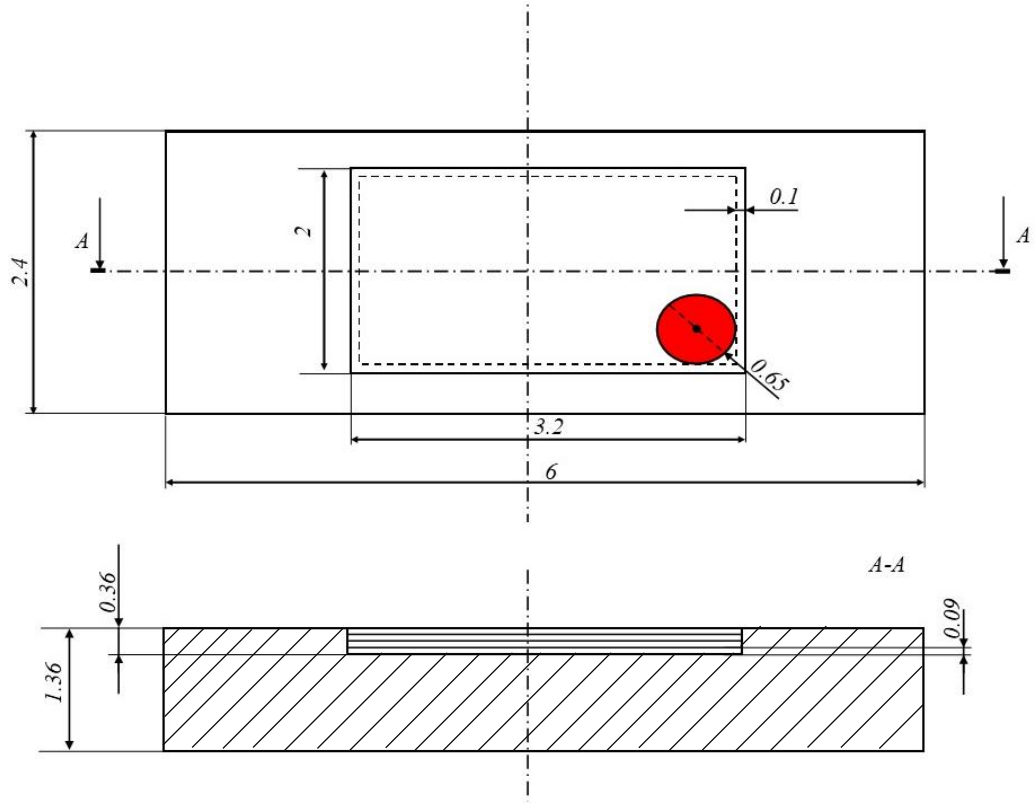


***Fig.62*** *Geometry of the part and position of initial activation zone (in red).*

### 5.2.4 Motion control

The comparison was made on the single layer with scanning on the long side (3 mm track). The scanning method used is the parallel scan lines. Depending on the line offset chosen on this layer, 6 scan lines will be processed.

The scan will consist of two sub-phases, a melting phase and an idle phase, in which there is no heat source in the model. The absence of beam occurs for a time equal to the time to process the remainder of a hypothetical track, 30 mm long (including the 3 mm already melted). So, the idle track is long 27 mm. This is because the test reference sample is a cube with 30 mm side length.

## 5.3 Results

### 5.3.1 Melt pool, size, geometry and temperature

The main reason for this comparison check was to measure the deviations in terms of melt pool size, melt pool geometry and temperature field. This allows us to estimate the gap between the model created and a model already validated experimentally. It also allows us to check the level of detail achieved in the model. A comparison was made between the dimensions of the melt pool and the maximum temperature considering the first and the third scan track. Since the parts considered in the respective models are different, the comparison was made with the same spatial coordinate z and equal to 1.5 mm.

***Tab. 9*** *Comparison between melt pool temperatures and size.*

| *TRACK 1* | $T_{max}$ *[K]* | $l_{pool}$ *[mm]* | $w_{pool}$ *[mm]* | $h_{pool}$ *[mm]* |
|---|---|---|---|---|
| *Model* | *2403* | *1.656* | *0.600* | *0.090* |
| *Reference model* | *2707* | *1.250* | *0.650* | *0.050* |

| *TRACK 3* | $T_{max}$ *[K]* | $l_{pool}$ *[mm]* | $w_{pool}$ *[mm]* | $h_{pool}$ *[mm]* |
|---|---|---|---|---|
| *Model* | *2773* | *1.440* | *0.600* | *0.090* |
| *Reference model* | *2729* | *1.300* | *0.600* | *0.050* |

From the results obtained for the values of the temperature field (Tab. ***9***) it can immediately be noticed that there is a great variation of the maximum temperature on the first scan track obtained from the model with activation with respect to that obtained from the reference model with material change. This is because the reference model takes into account the thermophysical properties of the powder, which isolates the heat exchange and causes an increase in the temperature of the melt pool. Instead the model with activation in part dissipates with the initial

activation zone and partly with the quiet elements, which do not have the thermophysical properties of the powder, but those of the bulk climb.

The difference between the maximum temperatures is attenuated as regards the tracks following the first one, with an overestimation, compared to the reference model, of about 70 K. This is because, according to the rather low line offset chosen, there is a large overlap between adjacent tracks. This is because, according to the rather low line offset chosen, there is a large overlap between adjacent tracks. If the line offset were lower, a smaller number of elements would be activated on the sides of the melt pool, which would lead to a lower maximum temperature. In fact, the maximum temperature reached is the result of the balance between two factors: the first goes to reduce the maximum temperature, since there is a dissipation towards the solidifying material; the second one goes to increase the maximum temperature, due to the overlap with the adjacent track.

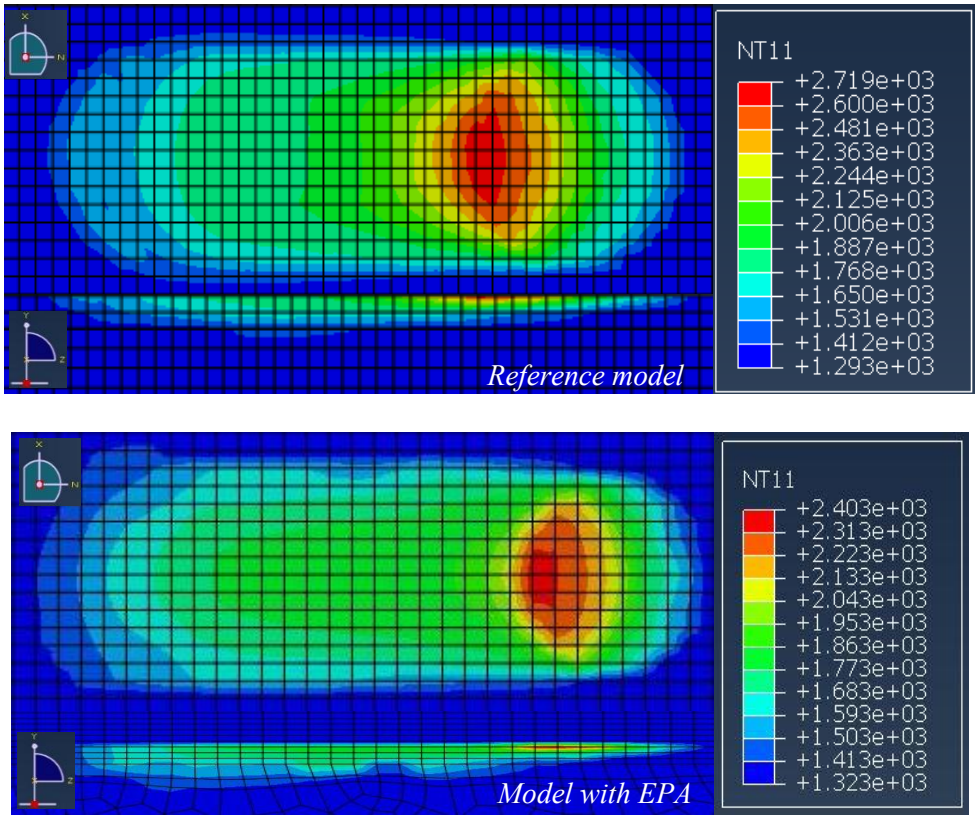


***Fig. 63*** *Temperature field, track 1*

Regarding the size of the melt pool the two models are almost similar. An overestimation of length and height can be seen in the case of the EPA model in both cases. In Fig. ***63*** and Fig. ***64*** the temperature distribution obtained is shown. We can observe an almost similar temperature field. Along y there are some differences as the models are made on solid parts with different mesh and geometry strategies. It can be seen in the third track a distortion of the melt pool towards the previous tracks, since the heat is transferred in this direction.

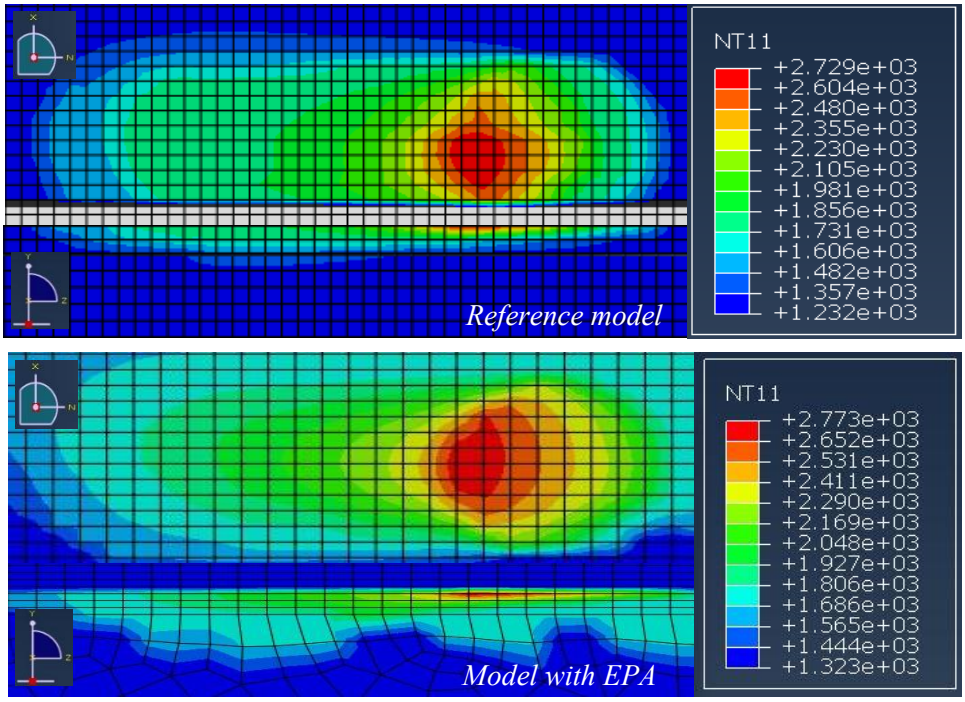


***Fig. 64*** *Field Temperature comparison, track 3*

## 5.3.2 Runtime comparison

***Tab.10*** shows the results obtained in terms of runtime for both models.

***Tab.10*** *Runtime comparison*

| ***Time*** | ***Model*** | ***Reference model*** |
|---|---|---|
| *Wall-clock time* | *20652 s* | *28800s* |
| *Actual time required for the process* | *0.065s* | |

Both models do not use the same mesh size, the EPA model uses an element size of 0.03 mm along y, while the reference model has a 0.05 mm mesh everywere. This entails an increase in the runtime in the case of the model with EPA compared to the reference model, due to the additional number of nodes present. Furthermore, in the case of the EPA model, simulations were conducted on a notebook with an Intel® Core™ i5-6200U 2.3GHz processor, while in the case of the reference model with an Intel® Core ™ i7-6700K 4.00 GHz processor.

## 5.4 Final considerations

As already announced, the model developed in this thesis work, with reference to a single-layer thermal uncoupled analysis, allows a considerable saving of the runtime required to perform the analysis. The model, although subject to a lower computational load since the "material change" was not implemented for the assignment of thermophysical properties, has produced fairly reliable results with reference to the model developed by Galati.

In particular, there is a difference of about 270 K with regard to the maximum melt pool temperature on the first track. For the following ones instead, the results are quite similar.

According to the geometry of the melt pool it was possible to observe a slight difference between the values of the length and height with respect to the reference model, while the width is almost similar.

Finally, we have seen how the implemented model allows a considerable saving in terms of both computational resources and runtime. In future work, therefore, the implementation of the material change will be evaluated in association with the element activation to obtain more accurate results.

# 6 Uncoupled multi-layer implementation

Performed a first verification on a single layer and analyzed the deviations from the reference model, the next step in the development of the model realized in this thesis work was to extend the simulation of the EBM process to a higher scale by implementing a multi-layer analysis, Fig.65.

In this way it was possible to consider the macroscopic aspects of the EBM process such as the temperature distribution between the layers and the surface roughness.

In this chapter the steps that led to the implementation of the code for the movement of the beam on multiple layers will be illustrated.

Compared to the single-layer, this analysis is more complex and deserves considerable attention on the management of the time parameters and the synchronization of the DFLUX and UEPACTIVATION VOL subroutines according to motion control. As for the progressive activation of the elements it was necessary to discriminate the various activation zones in each layer, in order not to have interference between contiguous layers.

The implementation of the multilayer, although currently realized for simple geometries, represents an important step for the successive improvements of the model. The analysis conducted aims to lay the foundations for a more accurate future analysis of the EBM process in order to allow a better choice of process parameters.

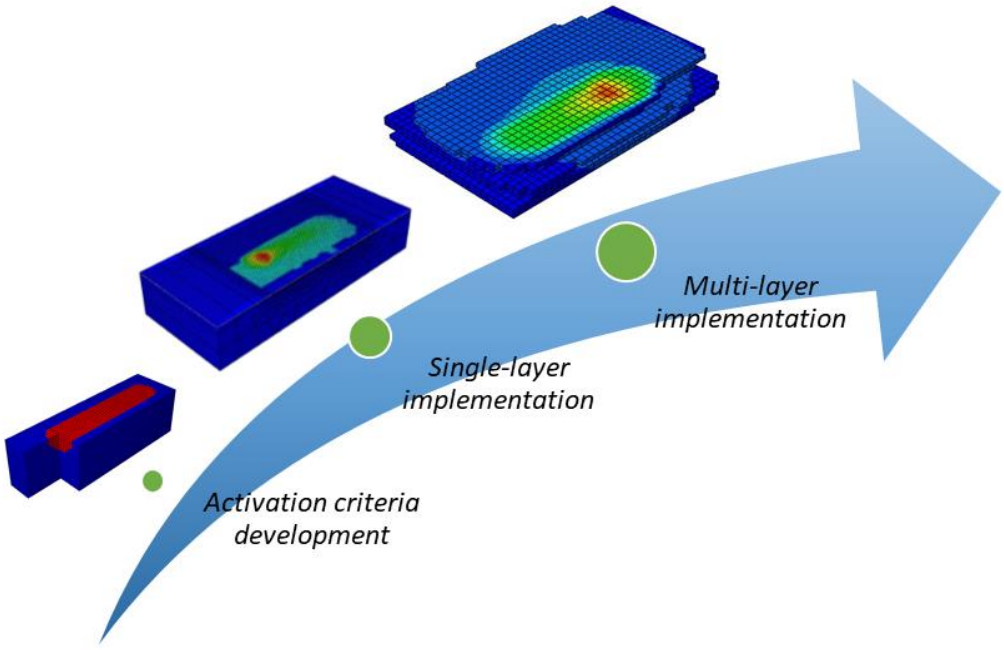


***Fig.65*** *Workflow from single-layer to multi-layer implementation.*

## 6.1 Steps of the analysis

The developed analysis can be summarized in Fig.67. As we can see, a multi-layer analysis was carried out on four layers to simulate the growth of the job. Initially, it was decided to conduct the analysis within a single step for each phase of the EBM process and to manage the various times through the subroutines. But this has brought some problems of activation of adjacent layers according to the developed code, since the EPA feature was enabled for the entire layer set. Unfortunately, within a single step it is possible to activate the EPA feature only for a single set of elements. Therefore, multi-step analysis was carried out, and for each analysis step a different set of elements, in their respective EPA, is activated, as shown in Fig.66.

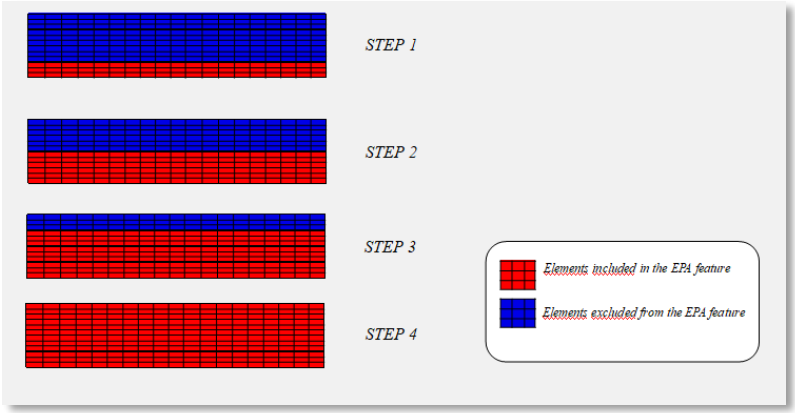


***Fig.66*** *Multiple EPA swtiching-on.*

Once the activation domains have been defined within each step, it is only necessary to develop the code to define the initial activation zones.

The analysis involves the processing of four layers, but it could be replicated on a larger number of layers. For each layer the pre-heating phase (with appropriate simplifying hypotheses which will be discussed in the dedicated subparagraph) has been considered, the melting phase and, inside this, the idle phases in which the heat source is turned off. A post-heating phase was not considered. This choice of process phases was made in accordance with the validation carried out with the reference model developed by Galati. In any case it would be possible to simulate a post-heating phase but on this it would not be possible to benefit from the element progressive activation since at the end of the melting phase all the elements are already activated, and it is not possible to switch off the elements.

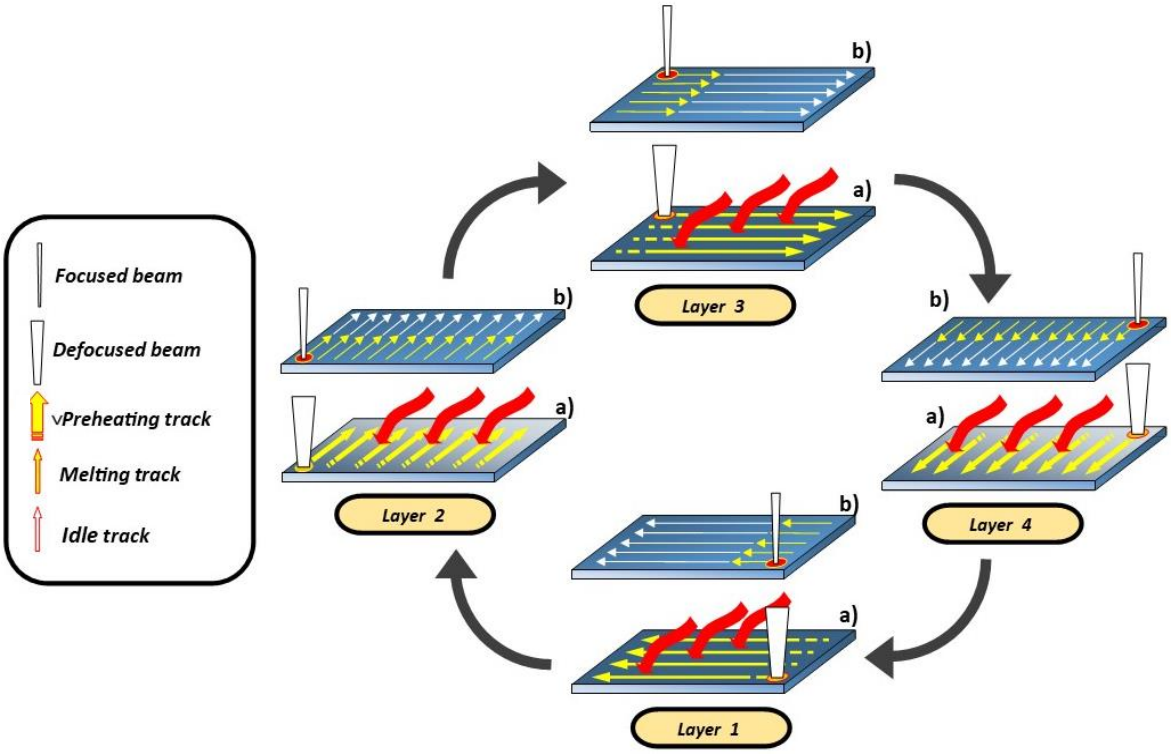


***Fig.67*** *Multi-layer analysis: a) preheating phase, b) melting phase.*

### 6.1.1 Pre-heating phase

As already anticipated in the chapter concerning the single-layer implementation, some simplifying hypotheses have been conducted regarding the preheating phase. Similarly to post-heating it is not possible to make tracks at high speed and defocused beam combined with element progressive activation as this would mean that, at the beginning of the melting phase, all the elements are active. For this reason, it was decided to associate an initial condition to the elements to be activated by assigning a predefined field temperature with constant amplitude and apparently magnitude at the pre-heating temperature. Theoretically it would be advisable to assign a temperature field, depending on the position of the various elements, which takes into account the historical temperature reached following the scanning at defocused beam and high speed. However, it was preferred to opt

for a simple solution, choosing a constant field since the high speeds involved and the presence of the powder that prevents heat exchange.

### 6.1.2 Melting and idle phases

As far as the melting phase is concerned, the same considerations made in the case of the single-layer apply, only that it happens on four layers. In the case of layers with scans that occur on the short side, the fusion takes place only for a track of length equal to 1.8 mm, and the source is turned off for a distance equal to 28.2 mm (30 mm total).

## 6.2 Multilayer motion control and scanning strategy

The multilayer analysis carried out deserves some attention with regard to motion control and timing synchronization. In fact, depending on the various process phases of the given layer, time determines the switching on of the various zones of initial activations. While the displacement of the heat source determines the propagation of thermal activation.

### 6.2.1 Heat source motion control

As regards the displacements of the heat source, as shown in Fig.67, the scanning strategy used is the parallel scan lines on the single layer. Instead, as regards the control of the initial position of the beam at the beginning of the process phases of the generic layer, a clockwise rotation with respect to the previous position is considered. Therefore, considering four layers the rotation is completed, and so repeatability can be obtained for multiple sets of four layers.

## 6.3 Code implementation and activation zone motion control

With regard to the switching on of the four initial activation zones it was decided to activate them in four different time intervals, as shown Fig.68.

Each activation zone is positioned at the height of the layer to which it refers. Each activation zone is cylindrical with a radius equal to $R_{true}$ and height equal to the height of the layer (0.09 mm). The coordinates (z, x) of the initial activation zone, at the beginning of each time interval are rotated 90° around an axis parallel to the y axis in a clockwise direction starting from the position of the initial activation zone of the first layer.

Each time interval has a necessary duration so that the beam travels a length equal to the sum of the melting track and the idle track. Fig.68 shows the timetable where the durations of the phases involved are listed. It can be seen that the distribution of the times during the processing of the four layers is quite differentiated. This is because there are 6 tracks on the first and third layers, and 11 tracks on the second and fourth. The idle times are dictated by the idle lengths which, as mentioned, are 27 mm in the case of the long side of the part and 28.2 mm in the case of the short side. This influences the history of heat distribution and therefore the temperature distribution on the final component.

The implemented code is depicted in Fig.69. The UEPACTIVATION VOL is structured according to alternative conditions on the times and sub-conditions on the space, defining the position and the instant of switch on of the initial activation zone. Specifically, if the instant time is within one, of the four, time intervals defined by the main conditions then the respective sub-condition is activated which selects the range of ordinates in which the activation zone is switched-on. A similar code is implemented inside the DFLUX for the motion control of the displacement of the heat source. Ultimately at the beginning of the melting phase each trace has, at the initial instant, an initial circular activation zone thanks to which it activates the element thermal progressive activation for each movement of the heat source.

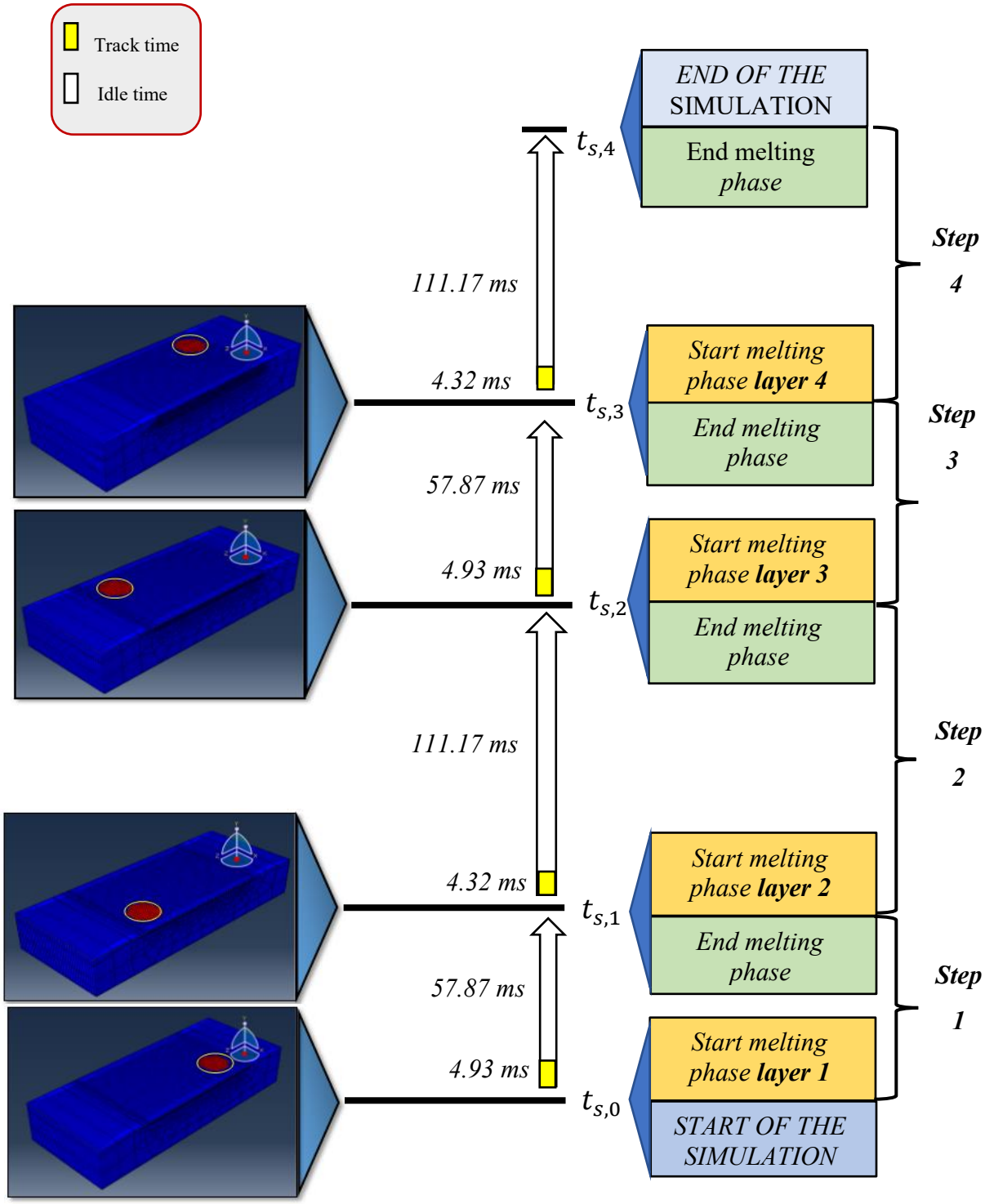


***Fig.68*** *Timetable of multilayer analysis.*

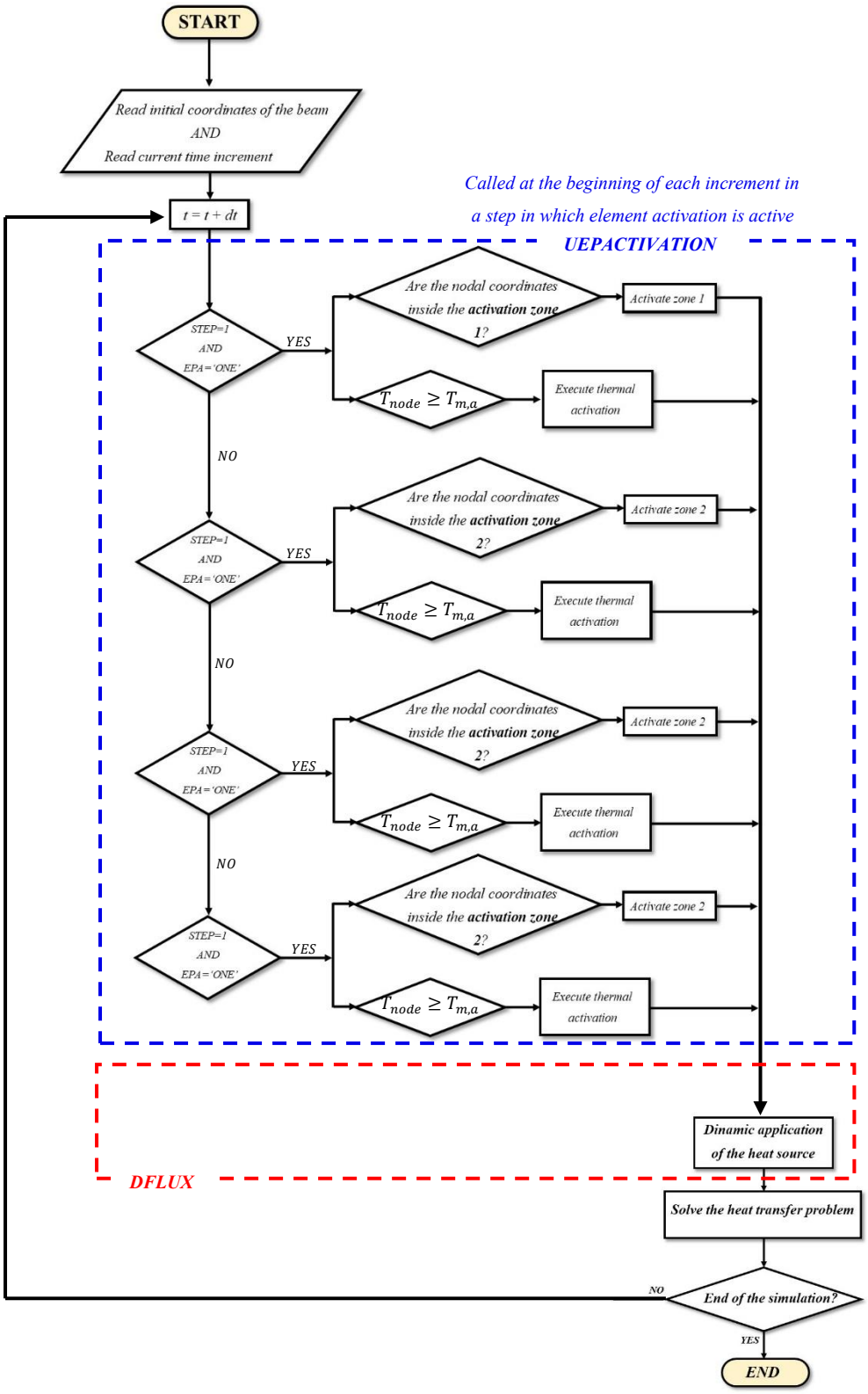


***Fig.61*** *Multilayer code implementation, flowchart.*

According to the EPA management presented, in each step a set of elements is included for activation, which includes the current layer and, in the steps following the first one, the previous layers. Therefore, according to the code developed, the thermal activation of the elements does not only occur in the current layer, but also in the underlying layers. This therefore simulates what really happens and defines the thermal history of the additive process.

## 6.4 Test simulation post-processing

A test simulation of the multilayer model was conducted. In this case a single mesh was used for the single layer with two rows of columns of elements (0.045 mm size along y) instead of three rows to reduce the runtime. The activation temperature was chosen equal to 1500 K to facilitate convergence and avoid interruptions in the tracks. The material used is the same used in the single-layer analysis. Fig.70 shows the simulation results in the different analysis steps considered.

Each processed layer involves the activation of a set of elements on the previous layer. Basically, according to the part considered, the maximum number of rows of elements that can be activated along the y direction is equal to 2. Obviously, depending on the temperature reached by the various elements in question, there will be a complete activation or not. Possible discontinuity between the layers are caused by the nodal temperatures which do not reach the minimum activation temperature. This phenomenon reproduces what happens in the EBM process where often there are process porosities in the layers, due precisely to a wrong choice of process parameters that leads to a lack of melting of the powders. On the other hand, the complete activation of the rows of elements involves the interaction between the bulk of the current track and the bulk of the previous layers, therefore a heat dissipation towards the lower layers, therefore a consequent activation of the elements not activated in the previous steps.

Fig.70 shows a circled area activated on the fourth layer by the temperature field generated by the third layer. This is due to the low activation temperature of the elements (1500 K) which caused a heat dissipation from the underlying layer towards the one above.

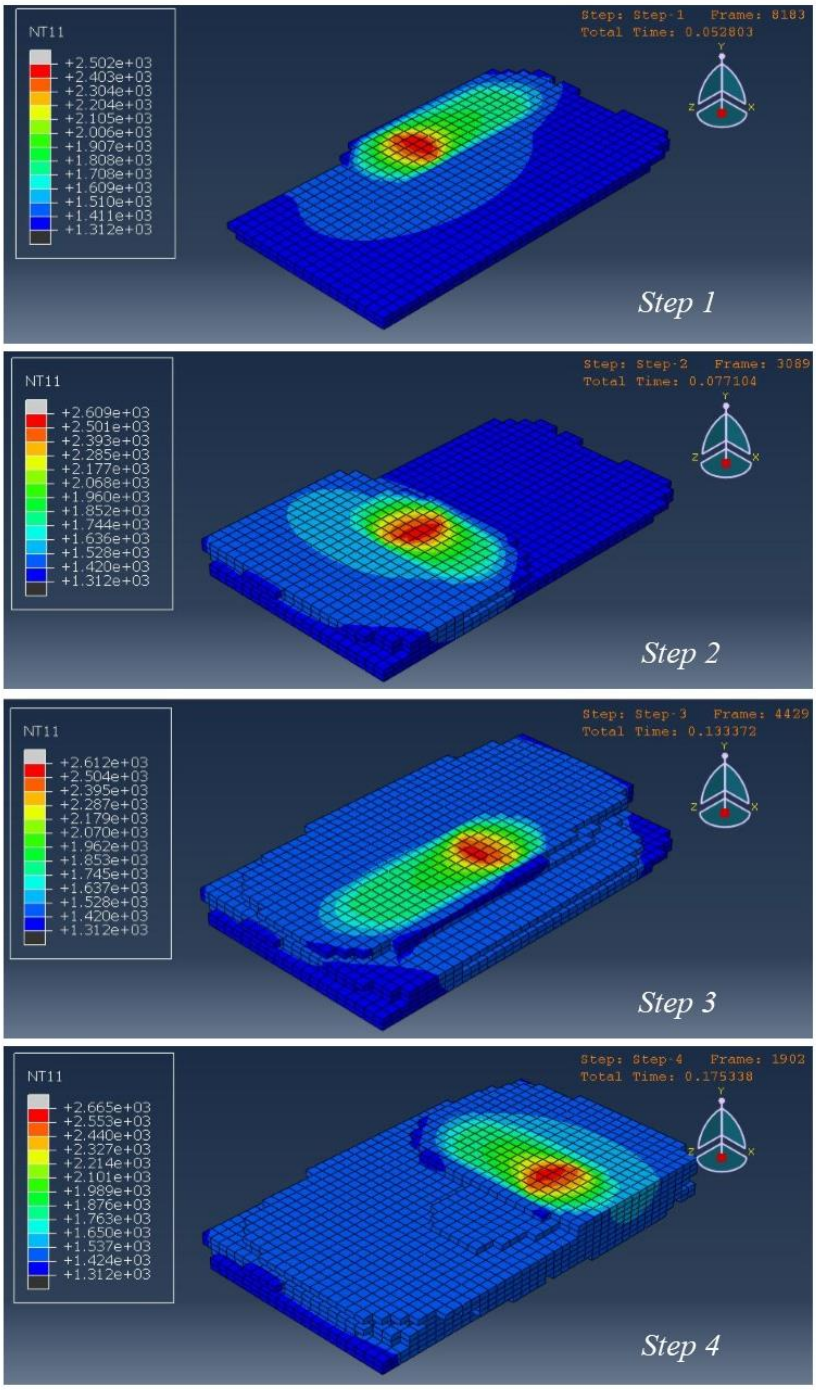


***Fig.70*** *Multilayer simulation, field temperatur on activated elements.*

The simulation was also performed on the Ti-6Al-4V as well as the 48Ti–48Al–2Cr–2Nb. The time comparison is shown in Tab. ***11***.

***Tab. 11*** *Runtime comparison according to multilayer simulation with Ti-6Al-4V and 48Ti-48Al-2Cr-2Nb.*

| ***Time*** | ***Ti-6Al-4V*** | ***48Ti–48Al–2Cr–2Nb*** |
|---|---|---|
| *Wall-clock time* | *22106 s* | *92021 s* |
| *Actual time required for the process* | *0.1393 s* | |

The substantial difference immediately emerges between the two materials in terms of complexity. Nevertheless, the simulation has produced results in a reasonable time thanks to the element progressive activation. All simulations were performed using a notebook with a processor Intel® Core™ i5-6200U 2.3GHz.

# 7 Multi-layer validation

## 7.1 Lateral surface roughness prediction

The analysis carried out allows, through a more accurate setting of the simulation parameters, the detection of the profile of the lateral molten surface of the part, which is determined by the activated elements that reach the solidus temperature (Fig.71). This discrete surface can be actively interpreted as lateral surface roughness.

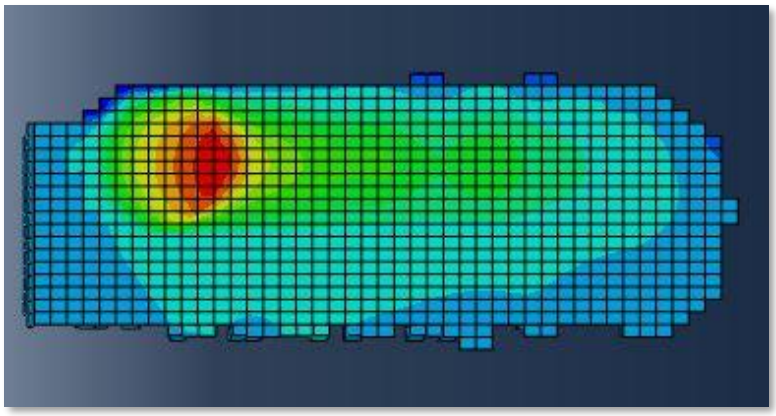

***Fig.71*** *Molten surface profile determined by thermal activation of the elements.*

## 7.2 Material state variable implementation

As already mentioned, to facilitate the convergence of the model the minimum temperature of activation of the elements with respect to the solidus temperature has been lowered. To be able to determine a reliable roughness profile, however, it is necessary to activate the elements at the solidus temperature. To overcome this problem, it was decided in any case to maintain the minimum activation temperature next to the solidus (1600 K) in order to have a better reliability of the results. To select the elements activated at the solidus temperature it was decided to implement a status variable (ID) using the USDFLD subroutine combined with the GETVRM utility routine, as shown in Fig.72. In particular, the USDFLD allows to define field variables at a material point as functions of time, while through GETVRM it is possible to obtain material point information. In this way it is possible, for each increment, to access the value of the solution (temperature) in the given material point, to use the variable ID as field variable, and update it within the USDFLD. This allows to create a historical output of the activated elements at the solidus temperature. The final code, including the DFLUX, UEPACTIVATION VOL and USDFLD subroutines is reported in appendix B.1 DFLUX, UEPACTIVATION VOL, USDFLD.

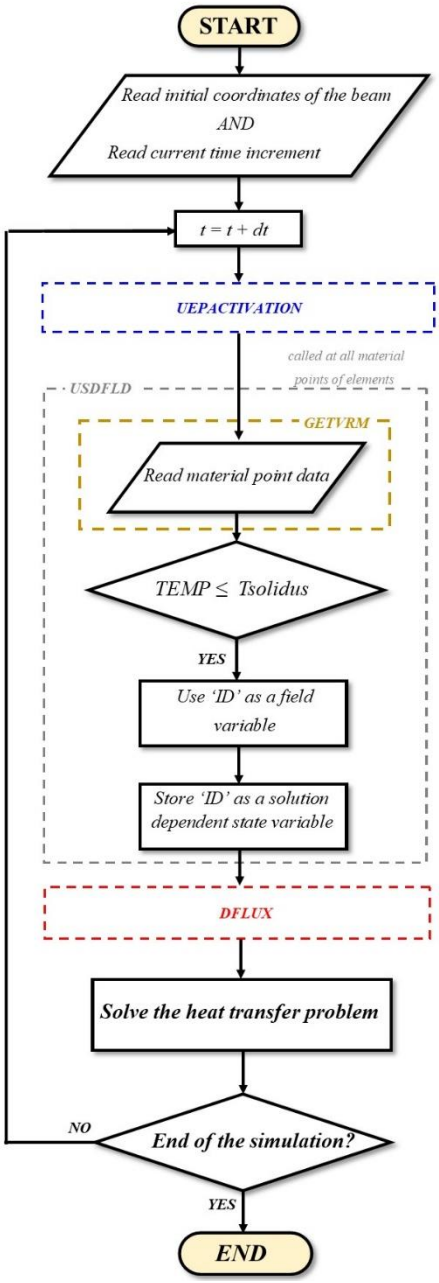


***Fig.72*** *USDFLD and GETVRM subroutine code implementation.*

# 7.3 Experimental validation

A first validation of the model was done on a cubic specimen with a side length of 30 mm. The sample was produced using an Arcam A2X system with Ti–48Al–2Cr–2Nb powders.

The following sub-chapters describe the measurement methodology and the instrument used for roughness measurements. All technical surveys and measurements were carried out at the Polito Integrated Additive Manufacturing (IAM) research center.

## 7.3.1 Surface roughness parameters definition

As a descriptor of surface characteristics, the parameters $R_a$, $R_q$ and $R_z$ are adopted. These parameters are defined in eq. 7.3.1. Fig.73 shows a representation of parameters considered [95].

$$R_a = \frac{1}{L} \cdot \int_0^L |z| \, dx$$

$$R_q = \sqrt{\frac{1}{L} \cdot \int_0^L z^2 \, dx} \qquad [7.3.1]$$

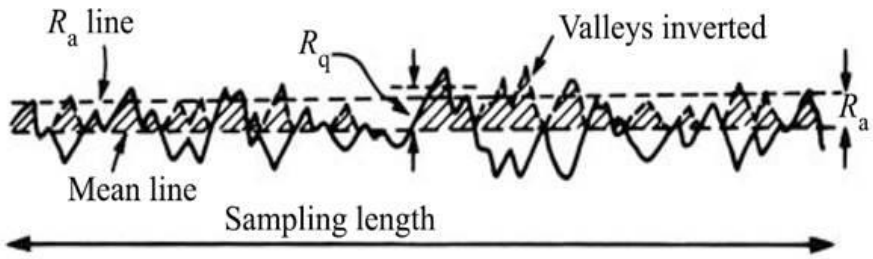


***Fig.73*** *Ra and Rq parameters .*

Where z is the distance between the mean line and the roughness profile, expressed as z=f(x) and L is the sample length. The last parameter, Rz, is defined as follow:

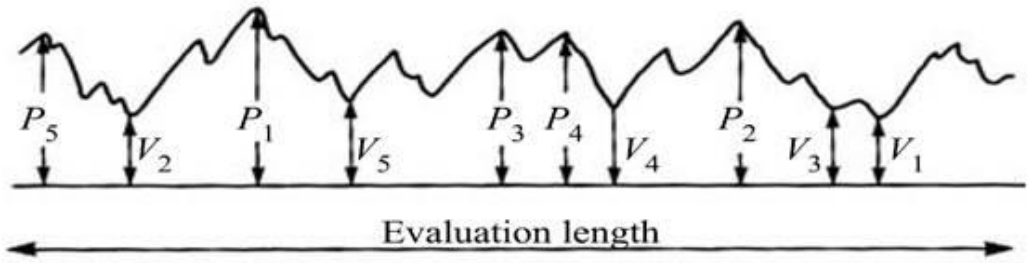


$$R_z = \frac{P_1 + P_2 + P_3 + P_4 + P_5 - (V_1 + V_2 + V_3 + V_4 + V_5)}{5} = \frac{\sum_{i=1}^{5} P_i - \sum_{i=1}^{5} V_i}{5}$$

Where Pn are the peaks, while Vn are the valleys measured always respect to a reference length. The adopted parameter to describe surface characteristics is Ra, although Rq has a greater statistical value, but is more difficult to be measured from a profile. Furthermore, Ra is the most adopted parameter in literature [95]

### 7.3.2 Instrument and methods

The instrument adopted to measure the profile is an RTP-80 profilometer (Metrology Systems, Volpiano, Italy) equipped with a TL90 drive unit.

The profile was measured adopting a cut-off length of 0.8 mm and a sampling length equal to five cut-off lengths, according to ISO 4288:1997 [97].

The roughness profile adopted for the evaluation of the profile characteristics is filtered, because an half of the cut-off length is removed at the beginning of the profile and an half of the cut-off is removed at the end of the profile, as clearly visible in Fig.75 ( the X axis starts at 0.4 mm and ends at 4.4 mm).

The surface considered for the evaluation of the characteristics is that one facing the machine door and the profile is acquired at the top position of the sample. The direction of the measure is parallel to the building direction, and goes from the centre of the surface toward the top of the sample ah shown in Fig. 74

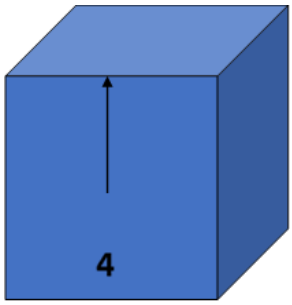


***Fig. 74*** *Sample.*

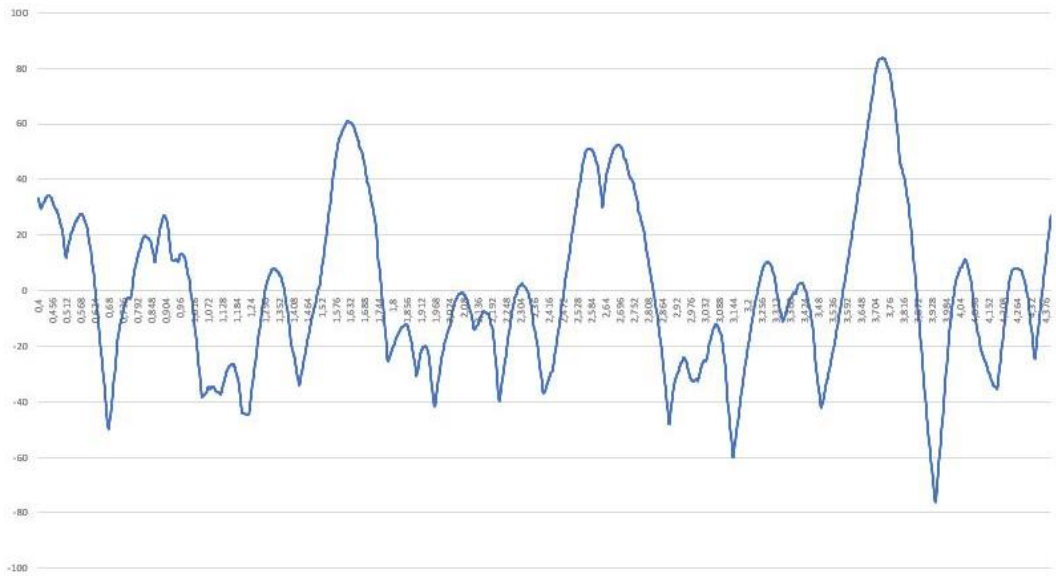


***Fig.75*** *Roughness profile sample*

The detected surface roughness parameters are reported in Tab.12

**Tab.12** Surface roughness parameters detected in 5 cut-off lengths

| *Cut-off* | $R_a$ *[µm]* | $R_q$ *[µm]* | $R_z$ *[µm]* |
|---|---|---|---|
| *1* | *20,899* | *26,475* | *108,504* |
| *2* | *22,831* | *26,429* | *93,663* |
| *3* | *23,694* | *28,453* | *107,51* |
| *4* | *21,671* | *26,461* | *103,067* |
| *5* | *25,607* | *30,638* | *112,702* |
| *mean* | *22,9404* | *27,6912* | *105,0892* |

The analysis carried out shows a qualitative correspondence of the simulated profile with respect to the range considered, as shown in Fig.76. It is possible to note a marked deviation of the simulated profile compared to the one detected at the first layers. It should be remembered that the substrate has not been simulated and the start of the detection is carried out starting from the center of the side face of the sample. Further future improvements to the model, together with the substrate simulation will allow a greater correspondence in the numerical results.

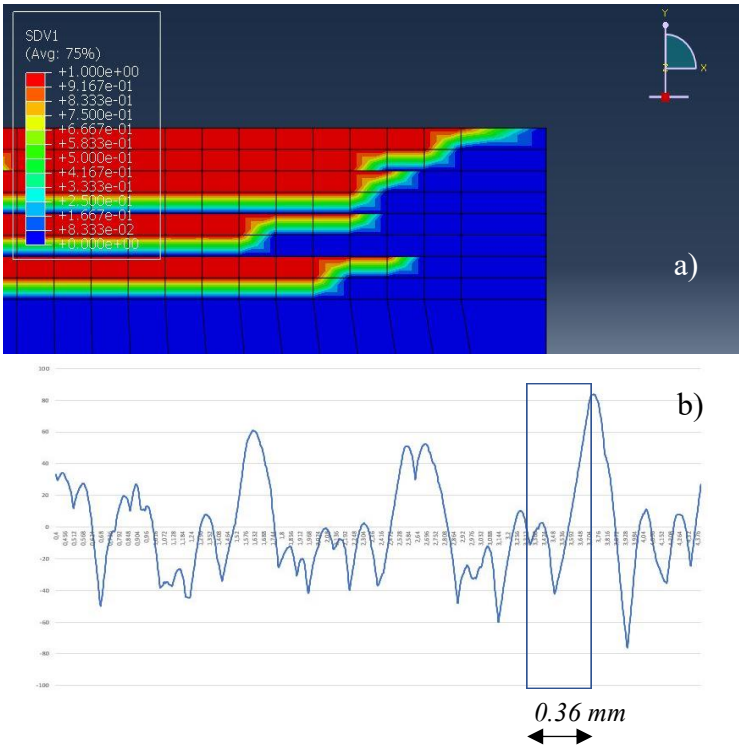


***Fig.76*** *Simulation of lateral surface roughness: a) simulated profile, b) detected profile.*

# 8 Conclusion

The present paper was aimed at deepening the state of the art on the Electron beam melting process simulation. The use of element progressive activation in the developed simulation model has allowed a better understanding of the process and a reduction in the calculation time compared to traditional simulation models.

In accordance with the activation criteria presented a comparison has been made, both in terms of runtime and temperature accuracy prediction, and it emerged that the best results are obtained using a pure thermal activation criterion.

The results of the single-layer verification showed a certain difference between the maximum temperature values for the first track, that tended to zero for the tracks following the first one. Therefore, it is deemed necessary to implement the material change, for greater accuracy in the results, combined with the progressive activation of the elements, to benefit from the runtime reduction. Once these differences were accepted, it was decided to extend the modeling scale and analyze macroscopic phenomena such as lateral surface roughness. Experimental validation of the results obtained from a multilayer analysis carried out on a sample made in 48Ti-48Al-2Cr-2Nb alloy was conducted. The implementation of a material state variable together with the element progressive activation has allowed to reconstruct a history of the elements melted at the solidus temperature of the material. Since the mesh size is equal to the average size of the powder particles, excluding the activated elements at temperatures lower than that of solidus allows the determination of the molten surface profile.

From the analysis of the simulated profile, some differences emerged with respect to the profile detected on the specimen, however both profiles, in the small range considered, show a qualitative similar trend. Therefore, from these results it emerged the need for further future improvements of the model, and further validations in view also of the possibility of use in the prediction of the residual porosity in the components produced by EBM.

# 9 Future work and further validations

- ## Development of material change

The uncoupled model realized in this thesis work, as seen, allows the prediction of the temperature field and the size of the melt pool with results quite comparable with those of the reference model developed by Galati et al. However, for better accuracy of the results, especially in the first tracks, or in any case in subsequent ones if the line offset is high, it will be necessary to implement the change of the thermophysical properties of the material. Therefore, the future works will see the improvement of the code on this front.

- ## Prediction of residual process porosity

As shown in the chapter dedicated to multi-layer implementation, the code developed allows the interaction between the layers to be simulated by thermal activation of the elements. The combination of a sufficiently high activation temperature together with an ad hoc material state variable also allows the identification of any residual porosity deriving from the process. Therefore, according to this aspect, further improvements will be made to the code in future works.

- ## Further future validations

In this thesis work, a first simulation validation and a single experimental validation of lateral roughness on a specimen were carried out. Further validations will be carried out in the future to certify the actual reliability of the model presented in the prediction of the physical quantities required. further future validations

# References


[1] F. Calignano, D. Manfredi, E. P. Ambrosio, S.Biamino, M. Lombardi, E. Atzeni, A. Salmi, P. Minetola, L. Iuliano and P. Fino, "Overview on Additive Manufacturing Technologies," *Proceedings of the IEEE,* vol. 105, no. 4, pp. 593-612, 2017.

[2] M. Markl and C. Körner, "Additive manufacturing using selective electron beam melting," *Welding and Cutting,* vol. 16, no. 3, pp. 177-184, 2017.

[3] B. Dutta and H. F. Froes, "The Additive Manufacturing (AM) of titanium alloys," *Metal Powder Report,* vol. 72, no. 2, pp. 96-106, 2017.

[4] H. Tang and W. J., "Review on metals additively manufactured by SEBM," *Materials Technology,* vol. 31, no. 2, pp. 86-89, 2016.

[5] Arcam, "Arcam History," Arcam, [Online]. Available: http://www.arcam.com/company/about-arcam/history/. [Accessed 06 04 2019].

[6] D. W. Rosen, "Research supporting principles for design for additive manufacturing," *Virtual and Physical Prototyping,* vol. 9, no. 4, p. 225–232, 2014 .

[7] Arcam, "EBM Aerospace," Arcam, [Online]. Available: http://www.arcam.com/solutions/aerospace-ebm/. [Accessed 1 4 2019].

[8] G. Additive, "Arcam," [Online]. Available: https://www.ge.com/additive/additive-manufacturing/materials/arcam. [Accessed 1 4 2019].

[9] S. Biamino, B. Klöden, T. Weißgärber, B. Kieback and U. Ackelid, “Properties of a TiAl turbocharger wheel produced by electron beam melting,” 2014.

[10] Arcam, “EBM Hardware,” Arcam, [Online]. Available: http://www.arcam.com/technology/electron-beam-melting/hardware/. [Accessed 04 04 2019].

[11] T. Mahale, “Electron beam melting of advanced materials and their structures,” Raleigh, North Carolina, 2009.

[12] Arcam, “Arcam Brochure,” [Online]. Available: http://www.arcam.com/technology/products/arcam-a2x-3/. [Accessed 04 04 2019].

[13] M. Galati and L. Iuliano, “A literature review of powder-based electron beam melting focusing,” *Additive manufacturing,* vol. 19, pp. 1-20, 2017.

[14] M. Ashfaq, M. M. Khan, A. Abdulrahman and R. K. R., “Effect of Energy Input on Microstructure and Mechanical Properties of Titanium Aluminide Alloy Fabricated by the Additive Manufacturing Process of Electron Beam Melting,” *Materials,* vol. 10, no. 211, pp. 1-16, 2017.

[15] B. Cheng, S. Price, J. Lydon, K. Cooper and K. Chou, “On process temperature in powder-bed electron beam additive manufacturing: model developmentand validation,” *J. Manuf. Sci. Eng. Trans. Asme,* vol. 136, 2016.

[16] N. P. and H. P. W., “Recyclability Study on Inconel 718 and Ti-6Al-4V Powders for Use in Electron Beam Melting,” *METALLURGICAL AND MATERIALS TRANSACTIONS,* vol. 47B, p. 762, 2016.

[17] J. V. V. Popov, K.-D. A., G. A. and B. M., “The effect of powder recycling on the mechanical properties and microstructure of electron beam melted Ti-6Al-4 V specimens,” *Additive manufacturing,* vol. 22, pp. 834-843, 2018.

[18] M. Sigl, S. Lutzmann and M. F. Zaeh, “Transient Physical Effects in Electron Beam Sintering,” Austin, TX, 2006.

[19] A. E., “Simulation of Selective Electron Beam Melting Processes,” University of Erlangen, Nuremberg, Germany, 2011.

[20] M. Agarwala, D. Bourell, J. Beaman and J. B. H. Marcus, “Direct selective laser sintering of metals,” *Rapid Prototyping Journal,* 1995.

[21] M. L. E., “Metallurgy of additive manufacturing: Examples from electron beam melting,” *Elsevier,* vol. Additive manufacturing , no. 5, pp. 40-53, 2015.

[22] J. Schwerdtfeger and C. Körner, “Selective electron beam melting of Ti-48Al-2Nb-2Cr: Microstructure and aluminium loss,” *Intermetallics,* vol. 49, pp. 29-35, 2014.

[23] G. Gruosso, “Le potenzialità della simulazione avanzata nell’Industria 4.0,” [Online]. Available: https://ricomincioda4.fondirigenti.it/le-potenzialita-della-simulazione-avanzata-nellindustria-4-0/. [Accessed 12 04 2019].

[24] M. I. Kellner, R. J. Madachy and D. M. Ra, “Software process simulation modeling: Why? What? How?,” *The Journal of Systems and Software,* vol. 46, pp. 91-105, 1999.

[25] S. Biamino, A. Penna, U. Ackelid, S. Sabbadini, O. Tassa, P. Fino, M. Pavese, P. Gennaro and C. Badini, “Electron beam melting of Ti-48Al-2Cr-2Nb alloy: Microstructure and mechanical properties investigation,” *Intermetallics,* no. 19, pp. 776-781, 2011.

[26] A. M., A. Alfaify, A. Al-Ahmari and M. M. Khan, “Effect of melt parameters on density and surface roughness in electron beam melting of gamma titanium aluminide alloy,” *Rapid Prototyping Journal,* vol. 23, no. 3, pp. 474-485, 2017.

[27] C. J. Smith, F. Derguti, E. H. Nava, M. Thomas, S. Tammas-Williams, S. Gulizia, D. Fraser and I. Todd, “Dimensional accuracy of Electron Beam Melting (EBM) additivemanufacture with regard to weight optimized truss structures,” *Journal of Materials Processing Technology,* 2016.

[28] S. Tammas-Williams, H. Zhaoa, F. Léonarda, F. Derguti, I. Toddb and P. Prangnell, "XCT analysis of the influence of melt strategies on defect population in Ti–6Al–4V components manufactured by Selective Electron Beam Melting," *Materials Characterization,* 2015.

[29] H. B. Qi, Y. N. Yan and R. J. Zhang, "Scanning method of filling lines in electron beam selective melting," *Proc. IMechE ,* vol. 221, pp. 1685-1694, 2007.

[30] C. Korner, E. Attar and P. Heini, "Mesoscopic simulation of selective beam melting processes," *Journal of Materials Processing Technology,* 2011.

[31] M. Ashfaq, A. Abdulrahman, M. M. K. and R. R. K., "Effect of Energy Input on Microstructure and Mechanical Properties of Titanium Aluminide Alloy Fabricated by the Additive Manufacturing Process of Electron Beam Melting," *Materials,* 2017.

[32] M. F. Zäh, S. Lutzmann, M. Kahnert and F. Walchshäusl, "Determination of Process Parameters for Electron Beam Sintering (EBS)," 2008.

[33] S. L. Zah M. F., "Modelling and simulation of electron beam melting," *Prod. Eng. Res. Devel.,* vol. 4, pp. 15-23, 2010.

[34] G. M. Mladenov, E. G. Koleva and D. N. Trushnikov, "Mathematical modelling for energy beam additive manufacturing," *Journal of Physics: Conf. Series,* 2018.

[35] W. Yan, J. Smith, W. Ge, F. Lin and W. K. Liu, "Multiscale modeling of electron beam and substrate interaction: a new heat source model," *Comput Mech,* vol. 56, p. 265–276, 2015 .

[36] W. Yan, W. K. Liu and F. Lin, "An effective Finite Element heat transfer model for Electron Beam Melting process," in *Conference: Advances in Materials and Processing Technologies Conference*, Madrid, Spain, 2015.

[37] H. J. Harding, "Mesoscopic modelling," *Solid State & Materials Science,* vol. 2, pp. 728-732, 1997.

[38] H. Xiaoyi and L. Li-Shi , "A priori derivation of the lattice Boltzmann equation," *Physical review,* vol. 55, no. 6, 1997.

[39] S. Chen and G. D. Doolen, “Lattice Boltzmann method for fluid flows,” *Annual Reviews Inc.,* vol. 30, p. 329–364, 1998.

[40] E. Attar and C. Körner, “Lattice Boltzmann method for dynamic wetting problems,” *Journal of Colloid and Interface Science,* vol. 335, p. 84–93, 2009.

[41] E. Attar and C. Korner, “Lattice Boltzmann model for thermal free surface flows with liquid–solid phase transition,” *International Journal of Heat and Fluid Flow,* vol. 32, p. 156–163, 2011.

[42] R. Ammer, C. Korner, M. Markl and U. Ljungblad, “Simulating fast electron beam melting with a parallel thermal free surface lattice Boltzmann method,” *Computers and Mathematics with Applications,* vol. 67, pp. 318-330, 2014.

[43] R. Ammer, C. Korner, U. Rude and M. Markl, “Modeling of Thermodynamic Phenomena with Lattice Boltzmann Method for Additive Manufacturing Processes,” in *23rd International Conference on Discrete Simulation of Fluid Dynamics (DSFD)*, Paris, 2014.

[44] A. Klassen, E. F. V., V. Juechter and C. Körner, “Numerical simulation of multi-component evaporation during selective electron beam melting of TiAl,” *Journal of Materials Processing Tech.,* vol. 247, p. 280–288, 2017.

[45] A. Klassen, V. E. Forster and C. Korner, “A multi-component evaporation model for beam melting processes,” *Modelling and Simulation in Materials Science and Engineering,* 2017.

[46] A. Klassen, “Simulation of evaporation phenomena in selectrive electron beam melting,” Nürnberg, 2017.

[47] W. Yan, Y. Qian, W. Ge, S. Lin, K. W. Liu, F. Lin and G. J. Wagner, “Meso-scale modeling of multiple-layer fabrication process in Selective Electron Beam Melting: Inter-layer/track voids formation,” *Materials and Design,* vol. 141, pp. 210-219, 2018.

[48] A. Neira Arce, “Thermal Modeling and Simulation of Electron Beam Melting for Rapid Prototyping on Ti6Al4V Alloys,” 2012.

[49] M. F. Zah and L. S., “Modelling and simulation of electron beam melting,” *Prod. Eng. Res. Devel,* vol. 4, pp. 15-23, 2010.

[50] N. Shen and K. Chou, “Thermal Modeling of Electron Beam Additive Manufacturing Process: Powder Sintering Effects,” in *International Manufacturing Science and Engineering Conference Collocatedwith the 40th North American Manufacturing Research Conference and inParticipation with the International Conference on Tribology Materials andProcessing,*, 2012.

[51] M. Galati, L. Iuliano, A. Salmi and E. Atzeni, “Modelling energy source and powder properties for the development of a thermal FE model of the EBM additive manufacturing process,” *Additive Manufacturing,* vol. 14, pp. 49-59, 2017.

[52] N. K. Tolochko, M. K. Arshinov, A. V. Gusarov, V. I. Titov, T. Laoui and L. Froyen, “Mechanisms of selective laser sintering and heat transfer in Ti powder,” *Rapid Prototyping Journal,* vol. 9, pp. 314-326, 2003.

[53] S. S. Sih and J. W. Barlow, “Emissivity of powder beds,,” in *Solid FreeformFabrication Symposium Proceedings, Center for Materials Science andEngineering, Mechanical Engineering Department and ChemicalEngineering Department*, the University of Texas at Austin, 1995.

[54] B. Cheng, S. Price, J. Lydon, K. Cooper and K. Chou, “On Process Temperature in Powder-Bed Electron Beam Additive Manufacturing: Model Development and Validation,” *J. Manuf. Sci. Eng. Trans. Asme,* vol. 136, 2014.

[55] D. Riedlbauer, T. Scharowsky, R. F. Singer, P. Steinmann, C. Korner and J. Mergheim, “Macroscopic simulation and experimental measurement of melt pool characteristics in selective electron beam melting of Ti-6Al-4V,” *Int. J. Adv. Manuf. Technol.,* vol. 88, p. 1309–1317, 2017.

[56] A. Klassen, A. Bauereiß and C. Korner, “Modelling of electron beam absorption in complex geometries,” *J. Phys. D: Appl. Phys.,* vol. 47, no. 065307, 2014 .

[57] D. Soldner and J. Mergheim, “Thermal modelling of selective beam melting processes using heterogeneous time step sizes,” *Computers and Mathematics with Applications,* no. https://doi.org/10.1016/j.camwa.2018.04.036., 2018.

[58] J. A. Koepf, D. Soldner, M. Ramsperger, J. Mergheim, M. Markl and C. Korner, “Numerical microstructure prediction by a coupled finite element cellular automaton model for selective electron beam melting,” *Computational Materials Science,* vol. 162, p. 148–155, 2019.

[59] T. M. Rodgers, J. D. Madison and V. Tikare , “Simulation of metal additive manufacturing microstructures using kinetic Monte Carlo,” *Computational Materials Science,* vol. 135, pp. 78-79, 2017.

[60] M. Jamshidinia, F. Kong and R. Kovacevic*, “Temperature distribution and fluid flow modeling of Electron Beam Melting® (EBM),” in *Proceedings of the ASME 2012 International Mechanical Engineering Congress & ExpositionNovember 9-15* , Houston, Texas, USA, 2012.

[61] M. Jamshidinia, F. Kong and R. Kovacevic, “Numerical modeling of heat distribution in the Electron Beam Meltingof Ti-6Al-4V,” *Journal of Manufacturing Science and Engineering,* vol. Vol. 135 , no. 061010-1, 2013.

[62] M. Jamshidinia and R. Kovacevic, “The Coupled CFD-FEM Model of Electron Beam Melting® (EBM),” in *Mechanical Engineering Research. Paper 4. http://digitalrepository.smu.edu/engineering_mechanical_research/4*, 2013 .

[63] G. Vastola, G. Zhang, Q. Pei and Y. W. Zhang, “Controlling of residual stress in additive manufacturing of Ti6Al4V by finite element modeling,” *Additive Manufacturing,* vol. 12, p. 231–239, 2016.

[64] M. Galati, L. Iuliano and A. Snis, “Powder bed properties modelling and 3D thermo-mechanical simulation of the additive manufacturing Electron Beam Melting process,” *Additive Manufacturing,* 2019.

[65] N. Shen and K. Chou, “Simulation of thermo-mechanical characteristics in Electron Beam Additive Manufacturing,” in *Proceedings of the ASME 2012 International Mechanical Engineering Congress & Exposition*, Houston, Texas, USA, 2012 .

[66] B. Cheng and K. Chou, “Thermal stresses associated with part overhang geometryin electron beam additive manufacturing: process parameter effects,” *Proc.Annu. Int. Solid Freeform Fabr. Symp.,* no. 1076, 2014.

[67] B. Cheng and K. Chou, “Geometric consideration of support structures in part overhang fabrications by electron beam additive manufacturing,” *Computer-Aided Design,* vol. 69, p. 102–111, 2015.

[68] W. Yan, W. Ge, J. Smith, S. Lin, O. L. Kafka and F. Lin, “Multi-scale modeling of electron beam melting of functionally graded materials,” *Acta Materialia,* vol. 115, pp. 403-412, 2016.

[69] M. Terner, S. Biamino, P. Epicoco, A. Penna, O. Hedin, S. Sabbadini, P. Fino, M.Pavese, U. Ackelid, P. Gennaro, F.Pelissero and C. Badini, “Electron Beam Melting of High Niobium Containing TiAl Alloy: Feasibility Investigation,” *steel research int. ,* vol. 83, no. 10, pp. 943-949, 2012.

[70] G. Baudana, S. Biamino, D. Ugues, M. Lombardi, P. Fino, M. Pavese and C. Badini, “Titanium aluminides for aerospace and automotive applications processed by Electron Beam Melting: Contribution of Politecnico di Torino,” *Metal Powder Report,* vol. 71, no. 3, pp. 193-199, 2016.

[71] D. Cormier, O. Harrysson, T. Mahale and H. West, “Freeform Fabrication of Titanium Aluminide via Electron Beam Melting Using Prealloyed and Blended Powders,” *Hindawi Publishing Corporation, Research Letters in Materials Science,* no. Article ID 34737, doi:10.1155/2007/34737, 2007.

[72] L. Murr, S. Gaytan, A. Ceylan, E. Martinez and J. Martinez, “Characterization of titanium aluminide alloy components fabricated by additive manufacturing using electron beam melting,” *Acta Materialia,* vol. 58, p. 1887–1894, 2010.

[73] J. Schwerdtfeger and C. Körner, “Selective electron beam melting of Ti-48Al-2Nb-2Cr: Microstructure and aluminium loss,” *Intermetallics,* vol. 49, pp. 29-35, 2014.

[74] M. Todaia, T. Nakanoa, T. Liua, H. Y. Yasudaa, K. Hagiharab, K. Choa, M. Uedac and M. Takeyamad, “Effect of building direction on the microstructure and tensile properties of Ti-48Al-2Cr-2Nb alloy additively manufactured by electron beam melting,” *Additive Manufacturing,* vol. 13, p. 61–70, 2017.

[75] J. Wang, K. Yang, N. Liu, L. Jia, G. Yang and H. Tang, “Microstructure and Tensile Properties of Ti-48Al-2Cr-2Nb Rods Additively Manufactured by Selective Electron Beam Melting,” *JOM,* vol. 69, no. 12, pp. 2751-2755, 2017.

[76] H. Yue, Y. Chen, X. Wang and F. Kong, “Effect of beam current on microstructure, phase, grain characteristic and mechanical properties of Ti-47Al-2Cr-2Nb alloy fabricated by selective electron beam melting,” *Journal of Alloys and Compounds,* vol. 750, pp. 617-625, 2018.

[77] Y. Chena, H. Yuea and X. Wanga, “Microstructure, texture and tensile property as a function of scanning speed of Ti-47Al-2Cr-2Nb alloy fabricated by selective electron beam melting,” *Materials Science & Engineering A,* vol. 713, p. 195–205, 2018.

[78] H. Yue, Y. Chen, X. Wang, S. Xiao and F. Kong, “Microstructure, texture and tensile properties of Ti-47Al-2Cr-2Nb alloy produced by selective electron beam melting,” *Journal of Alloys and Compounds,* vol. 766, pp. 450-459, 2018.

[79] P. Michaleris, “Modeling metal deposition in heat transfer analyses of additive manufacturing processes,” *FiniteElementsinAnalysisandDesign,* vol. 86, pp. 51-60, 2014.

[80] E. R. Denlinger, J. Irwin and P. Michaleris, “Thermomechanical Modeling of Additive Manufacturing Large Parts,” *Journal of Manufacturing Science and Engineering,* vol. 136, 2014.

[81] R. Jendrzejewski, G. Sliwinski, M. Krawczuk and W. Ostachowicz, "Temperature and stress fields induced during laser cladding," *Computers and Structures,* vol. 82, p. 653–658, 2004.

[82] R. Jendrzejewski and G. ´. liwin´ski, "Investigation of temperature and stress fields in laser cladded coatings," *Applied Surface Science ,* vol. 254, p. 921–925, 2007.

[83] J. E. S. Riqing Ye a, B. Zheng, Y. Zhoua and E. J. Lavernia, "Numerical modeling of the thermal behavior during the LENS® process," *Materials Science and Engineering A,* vol. 428, p. 47–53, 2006.

[84] A. Lundb¨ack and L. E. Lindgren, "Modelling of metal deposition," *Finite Elements in Analysis and Design,* vol. 47, p. 1169–1177, 2011.

[85] G. Zhu, A.Zhang, D. Li, Y. Tang, Z. Tong and Q. Lu, "Numerical simulation of thermal behavior during laser direct metal deposition," *Int J Adv Manuf Technol ,* vol. 55, p. 945–954, 2011.

[86] M. Asadi, M. Shubert, M. Kashani and M. Smith, "Exploring the Complex Welding Engineering Design Space using Computational Weld Mechanics," *Science in the Age of Experience,* 2017.

[87] A. Favaloro, E. Barocio, B. Brenken and B. Pipes, "Simulation of Polymeric Composites Additive Manufacturing using Abaqus," *Science in the Age of Experience,* 2017.

[88] B. Brenkena, E. Barocio, A.Favaloro, V. Kuncc and R. B. Pipes, "Development and validation of extrusion deposition additive manufacturing process simulations," *Additive Manufacturing,* vol. 25 , p. 218–226, 2019.

[89] E. Barocio, B. Brenken, A. Favaloro, M. Ramirez, J.Ramirez and R. B. Pipes, "Prediction of the Degree of Bonding in the Extrusion Deposition Additive Manufacturing Process of Semi Crystalline Polymer Composites," Purdue University, Composites Manufacturing and Simulation Center, 2019.

[90] T. Ales, “An integrated model for the probabilistic prediction of yield strength in electron-beam additively manufactured Ti-6Al-4V,” Graduate Theses and Dissertations, Iowa State University, 2018.

[91] W. M. F. M. W. P. M. J. Dantin, “Towards an open-source, preprocessing framework for simulating material deposition for a directed energy deposition process,” in *Solid Freeform Fabrication 2018: Proceedings of the 29th Annual International Solid Freeform Fabrication Symposium*, Mississippi, USA, 2018.

[92] P. Bajerski, R. Pecherski and D.Chudy, “Virtual Additive Manufacturing Based on Semicrystalline Polymer Polyetheretherketone (PEEK),” *Engineering Transactions,* vol. 67, no. 2, 2019.

[93] D. Sistémes, “Abaqus user's guide,” Dassault Sistémes , [Online]. Available: https://abaqus-docs.mit.edu/2017/English/SIMACAEANLRefMap/simaanl-c-elemactivation.htm#simaanl-c-elemactivation. [Accessed 16 11 2019].

[94] M. Galati, L. Iuliano and A. Snis, “Experimental validation of a numerical thermal model of the EBM process for Ti6Al4V,” *Computers and Mathematics with Applications,* vol. 78, p. 2417–2427, 2019.

[95] D. J. Whitehouse, Handbook Of Surface and anometrology Second Edition, CRC Press, 2011.

[96] A. Townsend, N. Senin, L. Blunt, R. Leach and J. Taylor, “ Surface texture metrology for metal additive,” *Precis. Eng.,* vol. 46, p. 34–47, 2016.

[97] G. M., M. P. and R. G., “Surface Roughness Characterisation and Analysis of the Electron Beam Melting (EBM) Process,” *Materials,* 2019.

[98] Arcam, “Process Validation tools,” [Online]. Available: http://www.arcam.com/technology/electron-beam-melting/process-validation-tools/. [Accessed 05 04 2019].

[99] A. T. Olanipekun, A. A. Abioye and K. E. Oluwabunmi, “Time-Dependent Ginzburg–Landau equation modelling of electron beam additive

manufactured Titanium alloy," *Leonardo Electronic Journal of Practices and Technologies,* pp. 93-102, 2018.

[100] H. Hassanin, L. Finet, S. C. Cox, P. Jamshidi and L. M. Grover, "Tailoring selective laser melting process for titanium drug-delivering implants with releasing micro-channels," *Additive Manufacturing,* 2018.

[101] J. Milberg and M. Sigl, "Electron beam sintering of metal powder," *German Academic Society for Production Engineering,* 2008.

[102] J. Schwerdtfeger, R. F. Singer and C. Korner, "In situ flaw detection by IR-imaging during electron beam melting," *Rapid Prototyping Journal,* vol. 18, no. 4, pp. 259-263, 2012.

[103] D. Riedlbauer, P. Steinmann and J. Mergheim, "Thermomechanical finite element simulations of selective electron beam melting processes: performance considerations," *Comput Mech,* vol. 54, p. 109–122, 2014.

[104] D. Riedlbauer, J. Mergheim and P. Steinmann, "Thermomechanical Simulation of the Electron Beam Melting Process for TiAl6V4," *PAMM Proc. Appl. Math. Mech,* vol. 14 , p. 463 – 464 , 2014.

[105] H. Tang, M. Qian, N. Liu, X. Zhang and G. Yang, "Effect of Powder Reuse Times on Additive Manufacturing of Ti-6Al-4V by Selective Electron Beam Melting," *The Minerals, Metals & Materials Society,* 2015.

[106] B. Cheng, S. Price, X. Gong, K. C. J. Lydon and K. Chou, "Speed Function Effects in Electron Beam Additive Manufacturing," Montreal, Quebec, Canada, 2014.

# Appendix A

# UEPACTIVATION VOL

## A.1 Interface parameters

As already mentioned, the UEPACTIVATION VOL subroutine is used to assign the volume fraction material to the elements that must be activated. Through the subroutine interface it is possible to access the parameters of the EPA feature. Below are listed some significant parameters used in the implementation of the model in question.

- *epaName*: the name of the element progressive activation;
- *noel*: user-assigned element number;
- *nElemNodes*: number of element nodes;
- *iElemNodes*: array containing user-assigned node numbers of the element;
- *coordNodes*: array containing the coordinates of the nodes of the element;
- *uNodes*: array containing displacements at the element nodes;
- *Kstep*: current step number;
- *Kinc*: current increment number;
- *time(1)*: current value of step time;
- *time(2)*: current value of total time;
- *Dtime*: time increment;
- *temp*: an array containing predefined temperature at the element nodes;
- *Npredef*: number of field variables;
- *predef*: array containing predefined field variables at the element nodes;
- *sol:* array of the solution variables at the beginning of the increment;
- *volFract*: total volume fracture of the material at the previous increment.

# Appendix B

# USER SUBROUTINES

## B.1 DFLUX, UEPACTIVATION VOL, USDFLD

Below is the code used to perform the multilayer analysis developed within the three subroutines, DFLUX, UEPACTIVATION VOL and USDFLD.

```
      SUBROUTINE DFLUX(FLUX,SOL,KSTEP,KINC,TIME,NOEL,NPT,COORDS,
     1 JLTYP,TEMP,PRESS,SNAME)
      INCLUDE 'ABA_PARAM.INC'
      DIMENSION FLUX(2), TIME(2), COORDS(3)
      CHARACTER*80 SNAME
c
c
c      DIMENSIONI MODELLO
      l=3                                        !length
      w=1.8                                     !width
      h=0.36                                     !height
c
c     PARAMETRI DI PROCESSO
      R=0.316                                   !Beam radius
      Rvero=0.350                               !Beam radius increased
      v=2800                                    !speed
      f=790140                                  !flux magnitude
      lt=0.09                                   !layer thickness
c
c
c
c     COORDINATE
      x=COORDS(1)
      y=COORDS(2)
      z=COORDS(3)
C
c
c
c
c     LAYER 1
c
      xlim=0.2
c
c     PARAMETRI LAYER
```

```
      ptz=(l/xlim)                              !total tracks along z
      ptx=(w/xlim)                              !total tracks along x
      nl=h/lt                                   !layer number
c
      t=TIME(1)
c
C     coordinate iniziali
      xi1=-0.1-Rvero
      zi1=0.1+Rvero
c
C     coordinate limite del profilo
      lz1=l
      llim1=27
      zlim1=zi1+llim1-Rvero
c
      t1=(30-2*Rvero)/v
c
      n=t/t1
      TR=int(n)
       xii1=xi1-n*xlim
       dz=v*(t-TR*t1)
c
      if (kstep.EQ.1)then
       if(xii1.GE.(xi1-5*xlim)) then
         if (((z-zi1-dz)**2+(x-xii1)**2).LE.R**2) then
               if ((z-zi1-dz).LE.zlim1.AND.y.GE.-0.272.AND.y.LE.-0.268) then
                FLUX(1)=f
               else if ((z-zi1-dz).GT.zlim1.AND.y.GE.-0.272.AND.y.LE.-0.268)
then
                FLUX(1)=0
           end if
         end if
       end if
      end if
c
c
c
c
c     LAYER 2
c
      xlim=0.2
c
c     PARAMETRI LAYER
      ptz=(l/xlim)
      ptx=(w/xlim)
      nl=h/lt
c
c     Coordinate iniziali
      xi2=-0.1-Rvero
      zi2=l+0.1-Rvero
c
C     coordinate limite del profilo
      lx2=w
      llim2=27
      xlim2=xi2+llim2-Rvero
c
      t2=(30-2*Rvero)/v
c
      n=t/t2
      TR=int(n)
c
      zii2=zi2-n*xlim
       dx=v*(t-TR*t2)
```

```
c
      if(kstep.EQ.2) then
       if(zii2.GE.(zi2-10*xlim)) then
        if (((x-xi2+dx)**2+(z-zii2)**2).LE.R**2) then
              if ((x-xi2+dx).LE.xlim2.AND.y.GE.-0.182.AND.y.LE.-0.178) then
                FLUX(1)=f
              else if ((x-xi2+dx).GT.xlim2.AND.y.GE.-0.182.AND.y.LE.-0.178)
then
                FLUX(1)=0
          endif
        end if
       end if
      end if
c
c
c
c     LAYER 3
c
      xlim=0.2
c     PARAMETRI LAYER
      ptz=(l/xlim)
      ptx=(w/xlim)
      nl=h/lt
c
c      Cordinate iniziali
      xi3=-1.7-0.1+Rvero
      zi3=l+0.1-Rvero
c
C     coordinate limite del profilo
      lz3=l
      llim3=27
      zlim3=zi3+llim3-Rvero
c
      t3=(30-2*Rvero)/v
c
      n=t/t3
      TR=int(n)
c
      xii3=xi3+n*xlim
       dz=v*(t-TR*t3)
c
      if(kstep.EQ.3) then
       if(xii3.LE.(xi3+5*xlim)) then
        if (((z-zi3+dz)**2+(x-xii3)**2).LE.R**2) then
              if ((z-zi3+dz).LE.zlim3.AND.y.GE.-0.092.AND.y.LE.-0.088) then
                FLUX(1)=f
      else if ((z-zi3+dz).GT.zlim3.AND.y.GE.-0.092.AND.y.LE.-0.088) then
                FLUX(1)=0
          endif
        endif
       end if
      end if
c
c
c
c
c     LAYER 4
c
      xlim=0.2
c
c     PARAMETRI LAYER
      ptz=(l/xlim)
      ptx=(w/xlim)
```

```
      nl=h/lt
c
      t=TIME(1)
c
c     Coordinate iniziali
      xi4=-1.7-0.1+Rvero
      zi4=0.1+Rvero
c
C     coordinate limite del profilo
      lx4=w
      llim4=27
      xlim4=1.8
c
      t4=(30-2*Rvero)/v
c
      n=t/t4
      TR=int(n)
c
      zii4=zi4+n*xlim
       dx=v*(t-TR*t4)
c
      if (kstep.EQ.4) then
       if(zii4.LE.(zi4+10*xlim)) then
        if (((x-xi4-dx)**2+(z-zii4)**2).LE.R**2) then
              if ((x-xi4-dx).LE.xlim4.AND.y.GE.-0.02.AND.y.LE.0.02)then
                FLUX(1)=f
          else if ((x-xi4-dx).GT.xlim4.AND.y.GE.-0.02.AND.y.LE.0.02)then
                FLUX(1)=0
          endif
        end if
       end if
      end if
c
c
      RETURN
      END
c
c
c
      subroutine uepactivationvol(
     * lFlags,
     * epaName,
     * noel,
     * nElemNodes,
     * iElemNodes,
     * mcrd,
     * coordNodes,
     * uNodes,
     * kstep,
     * kinc,
     * time,
     * dtime,
     * temp,
     * npredef,
     * predef,
     * nsvars,
     * svars,
     * sol,
     * solinc,
     * volFract,
     * nVolumeAddEvents,
     * volFractAdded,
     * csiAdded)
```

```
      include 'aba_param.inc'
      dimension
     * lFlags(*),
     * iElemNodes(nElemNodes),
     * coordNodes(mcrd,nElemNodes),
     * uNodes(mcrd,nElemNodes),
     * time(2),
     * temp(2,nElemNodes),
     * predef(2,npredef,nElemNodes),
     * svars(2,nsvars),
     * sol(nElemNodes),
     * solinc(nElemNodes),
     * volFract(*),
     * volFractAdded(*),
     * csiAdded(3,*)
      character*80 epaName
c
c
c
c
c
c     DIMENSIONI MODELLO
        l=3          !lunghezza
        w=1.8        !larghezza
c
c     PARAMETRI DI PROCESSO
        R=0.316
        Rvero=0.350
        v=2800
c
        r=Rvero                 !Initial activation zone radius
        ta=1600                 !Minimum activation temperature
c
c
        volFractAdded(1)=0.d0
c
        t=TIME(2)
c
c
c     LAYER 1
c
        x=coordNodes(1,3)
        yu=coordNodes(2,8)
        yl=coordNodes(2,1)
        z=coordNodes(3,3)
c
c     PARAMETRI DI LAYER
        xlim=0.2
        ptz=(l/xlim)
        ptx=(w/xlim)
c
c      COORDINATE LIMITE DEL PROFILO
        lz1=l
        t1=(lz1-2*Rvero)/v
c
        tf1=t1*6
c
        if(kstep.EQ.1) then
          if(epaName.EQ.'ONE')then
c         if(t.GE.0.AND.dt.LE.tf1) then
          if (yl.GE.-0.32 .AND. yu.LE.-0.27) then
c
            if(((x+0.1+Rvero)**2+ (z-0.1-Rvero)**2).LE.r**2)then
```

```
              volFractAdded(1) = 1.d0
            end if
          end if
c
          if(z.GE.0.AND.z.LE.3.2)then
            if(sol(1).GE. ta) then
              volFractAdded(1) = 1.d0
            else if (sol(2).GE. ta) then
              volFractAdded(1) = 1.d0
            else if (sol(3).GE. ta) then
              volFractAdded(1) = 1.d0
            else if (sol(4).GE. ta) then
              volFractAdded(1) = 1.d0
            else if (sol(5).GE. ta) then
              volFractAdded(1) = 1.d0
            else if (sol(6).GE. ta) then
              volFractAdded(1) = 1.d0
            else if (sol(7).GE. ta) then
              volFractAdded(1) = 1.d0
            else if (sol(8).GE. ta) then
              volFractAdded(1) = 1.d0
            end if
          end if
         end if
       end if
c
c       LAYER 2
        yu=coordNodes(2,1)
        yl=coordNodes(2,8)
c
c     PARAMETRI LAYER
      xlim=0.2
      ptz=(l/xlim)
      ptx=(w/xlim)
c
c     COORDINATE LIMITE PROFILO
      lx2=l
c
      t2=(w-2*Rvero)/v
       tf2=t1*6+t2*11 !ptz*t1+ptx*t2
c
        if (kstep.EQ.2)then
         if(epaName.EQ.'TWO')then
c        if(t.GE.tf1.AND.t.LE.tf2) then
         if(yl.GE.-0.27.AND. yu.LE.-0.18) then
c
          if(((x+0.1+Rvero)**2+ (z-l-0.1+Rvero)**2).LE.r**2)then
            volFractAdded(1) = 1.d0
          end if
       end if
c
        if(z.GE.0.AND.z.LE.3.2)then
          if(sol(1).GE. ta) then
              volFractAdded(1) = 1.d0
            else if (sol(2).GE. ta) then
              volFractAdded(1) = 1.d0
            else if (sol(3).GE. ta) then
              volFractAdded(1) = 1.d0
            else if (sol(4).GE. ta) then
              volFractAdded(1) = 1.d0
            else if (sol(5).GE. ta) then
              volFractAdded(1) = 1.d0
            else if (sol(6).GE. ta) then
```

```
              volFractAdded(1) = 1.d0
            else if (sol(7).GE. ta) then
              volFractAdded(1) = 1.d0
            else if (sol(8).GE. ta) then
              volFractAdded(1) = 1.d0
            end if
          end if
         end if
        end if
c
c
c       LAYER 3
c
        yu=coordNodes(2,8)
        yl=coordNodes(2,1)
c      PARAMETRI LAYER
       xlim=0.2
       ptz=(l/xlim)
       ptx=(w/xlim)
c
c      COORDINATE LIMITE PROFILO
       lz3=l
c
         t3=(lz3-2*Rvero)/v
         tf3=t3*6+t2*11+t1*6 !ptz*t1+ptx*t2+ptz*t3
c
        if(kstep.EQ.3) then
         if(epaName.EQ.'THREE')then
c          if(t.GE.tf2.AND.t.LE.tf3) then
         if(yl.GE.-0.18 .AND. yu.LE.-0.09) then
c
           if(((x+w+0.1-Rvero)**2+ (z-l-0.1+Rvero)**2).LE.r**2)then
             volFractAdded(1) = 1.d0
           end if
        end if
c
c
           if(z.GE.0.AND.z.LE.3.2)then
            if(sol(1).GE. ta) then
               volFractAdded(1) = 1.d0
             else if (sol(2).GE. ta) then
               volFractAdded(1) = 1.d0
             else if (sol(3).GE. ta) then
               volFractAdded(1) = 1.d0
             else if (sol(4).GE. ta) then
               volFractAdded(1) = 1.d0
             else if (sol(5).GE. ta) then
               volFractAdded(1) = 1.d0
             else if (sol(6).GE. ta) then
               volFractAdded(1) = 1.d0
             else if (sol(7).GE. ta) then
               volFractAdded(1) = 1.d0
             else if (sol(8).GE. ta) then
               volFractAdded(1) = 1.d0
             end if
           end if
        end if
       end if
c
c
c       LAYER 4
c
c
```

```
        yu=coordNodes(2,1)
        yl=coordNodes(2,8)
c     PARAMETRI LAYER
      xlim=0.2
      ptz=(l/xlim)
      ptx=(w/xlim)
c
c      COORDINATE LIMITE DEL PROFILO
      lx4=l
      t4=(w-2*Rvero)/v
      tf4=t4*11+t3*6+t2*11+t1*6 !ptz*t1+ptx*t2+ptz*t3+ptx*t4
c
      if(kstep.EQ.4) then
       if(epaName.EQ.'FOUR')then
c       if(t.GE.tf3.AND.t.LE.tf4) then
        if(yl.GE.-0.09 .AND. yu.LE.0) then
c
          if(((x+w+0.1-Rvero)**2+ (z-0.1-Rvero)**2).LE.r**2)then
            volFractAdded(1) = 1.d0
          end if
       end if
c
        if(z.GE.0.AND.z.LE.3.2)then
          if(sol(1).GE. ta) then
              volFractAdded(1) = 1.d0
            else if (sol(2).GE. ta) then
              volFractAdded(1) = 1.d0
            else if (sol(3).GE. ta) then
              volFractAdded(1) = 1.d0
            else if (sol(4).GE. ta) then
              volFractAdded(1) = 1.d0
            else if (sol(5).GE. ta) then
              volFractAdded(1) = 1.d0
            else if (sol(6).GE. ta) then
              volFractAdded(1) = 1.d0
            else if (sol(7).GE. ta) then
              volFractAdded(1) = 1.d0
            else if (sol(8).GE. ta) then
              volFractAdded(1) = 1.d0
            end if
        end if
       end if
      end if
c
c
c
      return
      end
c
c
       SUBROUTINE USDFLD(FIELD,STATEV,PNEWDT,DIRECT,T,CELENT,
     1            TIME,DTIME,CMNAME,ORNAME,NFIELD,NSTATV,NOEL,NPT,LAYER,
     2            KSPT,KSTEP,KINC,NDI,NSHR,COORD,JMAC,JMATYP,MATLAYO,
     3            LACCFLA)
C
      INCLUDE 'ABA_PARAM.INC'
C
      CHARACTER*80 CMNAME,ORNAME
      CHARACTER*3  FLGRAY(15)
      DIMENSION FIELD(NFIELD),STATEV(NSTATV)
      dimension array(15),jarray(15)
      INTEGER MAT_ID2
c
```

```
c     current temperature
      CALL GETVRM('TEMP',ARRAY,JARRAY,FLGRAY,JRCD,JMAC,JMATYP,
     1 MATLAYO,LACCFLA)
      TEMP = ARRAY(1)
      ID=STATEV(1)
c
      if (TEMP.GE.1737) then
          ID=1
      end if
c
        FIELD(1)=ID           !Use ID as field variable
        STATEV(1)=FIELD(1)    !store ID as a solution dependent state variable
c
        write(6,*) '!!! USDFLD CALLED !!!'
c
c
C     If error, write comment to .DAT file:
      IF(JRCD.NE.0)THEN
       WRITE(6,*) 'REQUEST ERROR IN USDFLD FOR ELEMENT NUMBER ',
     1     NOEL,'INTEGRATION POINT NUMBER ',NPT
      ENDIF
c
      RETURN
      END
```